PD-74-058
December 1974

LASER DOPPLER VELOCIMETER SYSTEM SIMULATION FOR SENSING AIRCRAFT WAKE VORTICES

J.A.L. Thomson and J.C.S. Meng

Contractor: Physical Dynamics, Inc.
Contract Number: NAS8-28984
Effective Date of Contract: 18 December 1972
Contract Expiration Date: 2 February 1975
Amount of Contract: $89,466.00

Principal Investigator: J. Alex Thomson
Phone: (415) 848-3063

Procurement Officer: Ray Weems
Phone: (205) 453-2857

Contracting Officer's Representative:
R. Milton Huffaker
Phone: (205) 453-1595

Approved for public release;
distribution unlimited.

This research was supported by the National Aeronautics and Space Administration and was monitored by R. Milton Huffaker, S&E-AERO-A, NASA, Marshall Space Flight Center, Ala. 38512, under Contract NAS8-28984.

UNCLASSIFIED

SECURITY CLASSIFICATION OF THIS PAGE *(When Data Entered)*

REPORT DOCUMENTATION PAGE

READ INSTRUCTIONS BEFORE COMPLETING FORM

1. REPORT NUMBER

2. GOVT ACCESSION NO.

3. RECIPIENT'S CATALOG NUMBER

4. TITLE *(and Subtitle)*
LASER DOPPLER VELOCIMETER SYSTEM SIMULATION FOR SENSING AIRCRAFT WAKE VORTICES

5. TYPE OF REPORT & PERIOD COVERED
Final
18 Dec 72 - 2 Feb 75

6. PERFORMING ORG. REPORT NUMBER
PD-74-058

7. AUTHOR(s)
J.A.L. Thomson and J.C.S. Meng

8. CONTRACT OR GRANT NUMBER(s)
NAS8-28984

9. PERFORMING ORGANIZATION NAME AND ADDRESS
Physical Dynamics, Inc.
P.O. Box 1069
Berkeley, California 94701

10. PROGRAM ELEMENT, PROJECT, TASK AREA & WORK UNIT NUMBERS

11. CONTROLLING OFFICE NAME AND ADDRESS
George C. Marshall Space Flight Center
National Aeronautics and Space Administration
Marshall Space Flight Center, Alabama 35812

12. REPORT DATE
December 1974

13. NUMBER OF PAGES
111

14. MONITORING AGENCY NAME & ADDRESS *(if different from Controlling Office)*

15. SECURITY CLASS. *(of this report)*
UNCLASSIFIED

15a. DECLASSIFICATION/DOWNGRADING SCHEDULE

16. DISTRIBUTION STATEMENT *(of this Report)*
Approved for public release; distribution unlimited.

17. DISTRIBUTION STATEMENT *(of the abstract entered in Block 20, if different from Report)*

18. SUPPLEMENTARY NOTES

19. KEY WORDS *(Continue on reverse side if necessary and identify by block number)*
Laser Velocimeter
Vortex Wakes
Simulation

20. ABSTRACT *(Continue on reverse side if necessary and identify by block number)*

A hydrodynamic model of aircraft vortex wakes in an irregular wind shear field near the ground is developed and used as a basis for modeling the characteristics of a laser doppler detection and vortex location system. The trailing vortex sheet and the wind shear are represented by discrete free vortices distributed over a two-dimensional grid. The time dependent hydrodynamic equations are solved by direct numerical integration in the Boussinesq approximation. The ground boundary is simulated by images, and fast Fourier Transform techniques are used to evaluate the vorticity stream function. The

UNCLASSIFIED

SECURITY CLASSIFICATION OF THIS PAGE *(When Data Entered)*

INSTRUCTIONS FOR PREPARATION OF REPORT DOCUMENTATION PAGE

RESPONSIBILITY. The controlling DoD office will be responsible for completion of the Report Documentation Page, DD Form 1473, in all technical reports prepared by or for DoD organizations.

CLASSIFICATION. Since this Report Documentation Page, DD Form 1473, is used in preparing announcements, bibliographies, and data banks, it should be unclassified if possible. If a classification is required, identify the classified items on the page by the appropriate symbol.

COMPLETION GUIDE

General. Make Blocks 1, 4, 5, 6, 7, 11, 13, 15, and 16 agree with the corresponding information on the report cover. Leave Blocks 2 and 3 blank.

Block 1. Report Number. Enter the unique alphanumeric report number shown on the cover.

Block 2. Government Accession No. Leave Blank. This space is for use by the Defense Documentation Center.

Block 3. Recipient's Catalog Number. Leave blank. This space is for the use of the report recipient to assist in future retrieval of the document.

Block 4. Title and Subtitle. Enter the title in all capital letters exactly as it appears on the publication. Titles should be unclassified whenever possible. Write out the English equivalent for Greek letters and mathematical symbols in the title *(see "Abstracting Scientific and Technical Reports of Defense-sponsored RDT/E,"AD-667 000).* If the report has a subtitle, this subtitle should follow the main title, be separated by a comma or semicolon if appropriate, and be initially capitalized. If a publication has a title in a foreign language, translate the title into English and follow the English translation with the title in the original language. Make every effort to simplify the title before publication.

Block 5. Type of Report and Period Covered. Indicate here whether report is interim, final, etc., and, if applicable, inclusive dates of period covered, such as the life of a contract covered in a final contractor report.

Block 6. Performing Organization Report Number. Only numbers other than the official report number shown in Block 1, such as series numbers for in-house reports or a contractor/grantee number assigned by him, will be placed in this space. If no such numbers are used, leave this space blank.

Block 7. Author*(s)*. Include corresponding information from the report cover. Give the name*(s)* of the author*(s)* in conventional order *(for example, John R. Doe or, if author prefers, J. Robert Doe)*. In addition, list the affiliation of an author if it differs from that of the performing organization.

Block 8. Contract or Grant Number*(s)*. For a contractor or grantee report, enter the complete contract or grant number*(s)* under which the work reported was accomplished. Leave blank in in-house reports.

Block 9. Performing Organization Name and Address. For in-house reports enter the name and address, including office symbol, of the performing activity. For contractor or grantee reports enter the name and address of the contractor or grantee who prepared the report and identify the appropriate corporate division, school, laboratory, etc., of the author. List city, state, and ZIP Code.

Block 10. Program Element, Project, Task Area, and Work Unit Numbers. Enter here the number code from the applicable Department of Defense form, such as the DD Form 1498, "Research and Technology Work Unit Summary" or the DD Form 1634. "Research and Development Planning Summary," which identifies the program element, project, task area, and work unit or equivalent under which the work was authorized.

Block 11. Controlling Office Name and Address. Enter the full, official name and address, including office symbol, of the controlling office. *(Equates to funding/sponsoring agency. For definition see DoD Directive 5200.20, "Distribution Statements on Technical Documents.")*

Block 12. Report Date. Enter here the day, month, and year or month and year as shown on the cover.

Block 13. Number of Pages. Enter the total number of pages.

Block 14. Monitoring Agency Name and Address *(if different from Controlling Office)*. For use when the controlling or funding office does not directly administer a project, contract, or grant, but delegates the administrative responsibility to another organization.

Blocks 15 & 15a. Security Classification of the Report: Declassification/Downgrading Schedule of the Report. Enter in 15 the highest classification of the report. If appropriate, enter in 15a the declassification/downgrading schedule of the report, using the abbreviations for declassification/downgrading schedules listed in paragraph 4-207 of DoD 5200.1-R.

Block 16. Distribution Statement of the Report. Insert here the applicable distribution statement of the report from DoD Directive 5200.20, "Distribution Statements on Technical Documents."

Block 17. Distribution Statement *(of the abstract entered in Block 20, if different from the distribution statement of the report)*. Insert here the applicable distribution statement of the abstract from DoD Directive 5200.20, "Distribution Statements on Technical Documents."

Block 18. Supplementary Notes. Enter information not included elsewhere but useful, such as: Prepared in cooperation with . . . Translation of *(or by)* . . . Presented at conference of . . . To be published in . . .

Block 19. Key Words. Select terms or short phrases that identify the principal subjects covered in the report, and are sufficiently specific and precise to be used as index entries for cataloging, conforming to standard terminology. The DoD "Thesaurus of Engineering and Scientific Terms" *(TEST)*, AD-672 000, can be helpful.

Block 20. Abstract. The abstract should be a brief *(not to exceed 200 words)* factual summary of the most significant information contained in the report. If possible, the abstract of a classified report should be unclassified and the abstract to an unclassified report should consist of publicly- releasable information. If the report contains a significant bibliography or literature survey, mention it here. For information on preparing abstracts see "Abstracting Scientific and Technical Reports of Defense-Sponsored RDT&E," AD-667 000.

atmospheric turbulence was simulated by constructing specific realizations at time t=0, assuming Kolmogoroff's law applies, and that the dissipation rate is constant throughout the flow field. Although the primary purpose of the study reported here was to analyze the laser doppler velocimeter system, characteristics of other systems are also discussed in the framework of the present model.

The response of a simulated laser doppler velocimeter is analyzed by simulating the signal return from the flow field as sensed by a simulation of the optical/electronic system. Patterns of various features of the signature are presented in range-elevation angle plots. The problem of locating the vortex centers is discussed both as a pattern recognition problem and as a "point" target problem.

TABLE OF CONTENTS

LIST OF FIGURES

LASER DOPPLER VELOCIMTER SYSTEM SIMULATION FOR SENSING AIRCRAFT WAKE VORTICES

by

J.A.L. Thomson and J.C.S. Meng

SUMMARY

A hydrodynamic model of aircraft vortex wakes moving in a turbulent wind shear field near the ground is developed and used as a basis for modeling the characteristics of a laser doppler detection and vortex location system. The trailing vortex sheet and the wind shear are represented by discrete free vortices distributed over a two-dimensional grid. The time dependent hydrodynamic equations are solved by direct numerical integration. The effects of buoyant exhaust and atmospheric stratifications are incorporated in the Boussinesq approximation. The ground boundary is simulated by images, and fast Fourier Transform techniques are used to evaluate the vorticity stream function. The atmospheric turbulence was simulated by constructing specific realizations at time t=0, assuming Kolmogoroff's law applies, and that the dissipation rate is constant throughout the flow field. Although the primary purpose of the study reported here was to analyze the laser doppler velocimeter system, characteristics of other systems are also discussed in the framework of the present model.

The response of a simulated laser doppler velocimeter is analyzed by simulating the signal return from the

flow field as sensed by a simulation of the optical/ electronic system. Patterns of various features of the signature are presented in range-elevation angle plots. The problem of locating the vortex centers is discussed both as a pattern recognition problem and as a "point" target problem.

I.0 INTRODUCTION

The implementation of reliable, efficient and safe control of the air traffic in the airport terminal environment requires detailed knowledge of the wind shear fields in the vicinity of the airport and, in particular, in wakes of the larger aircraft. These wakes following the aircraft bear characteristics of the aircraft's weight, wing span and configuration, approach speed and height, engine configuration, engine exhaust buoyancy and thrust, as well as environmental characteristics: vertical wind shear, turbulence level and atmospheric stability. In this report we describe a model which simulates the interaction of a laser-doppler velocimeter with the wake flow field. This combined model of the wake and the detector system is expected to be useful both in the design of detection systems and in analyzing or correlating test data.

For simple wings the lift force is distributed elliptically (to a good approximation), along the wing so that the maximum circulation shed per length (the spanwise derivative of the lift) is at the wing tip. Hence, the maximum upwash velocity is also at the tip, and roll up occurs there first and extends toward the fuselage. Since the maximum vorticity is at the tip, most of the vorticity shed by the wing is relatively quickly concentrated into a tip vortex. Many previous analyses were based upon the approximation that the trailing vortex sheet can be represented by two well defined counter rotating cylindrical "tip vortices".

All of the detection systems presently considered rely specifically on such a model of the flow field in order to deduce the vortex locations. One of the prime objectives of the LDV[*] system is to provide spatially-resolved velocity fields. However, even here finite range resolution limits the location accuracy. In order to be able to assess and develop an optimal design, a hydrodynamic model is developed which provides a reasonably realistic description of the wind shear field; in particular, it is capable of treating non-simple wing loadings (i.e., general flap configuration), the early time period before wrap-up, the vertical wind shear, simulated atmospheric turbulence, interaction of multiple wake vortex regions, buoyant and stratification effects of the ambient atmosphere and of the engine exhaust gases.

When the buoyancy of the exhaust gases and of the ambient atmosphere is included, the vertical motion of the wake is modified at late time. Characteristic times for stratification effects are measured by the Brünt-Väisälä time ($\tau = \left[T_p/(g\partial T_p/\partial z)\right]^{\frac{1}{2}}$, where T_p is the "potential" temperature), and are typically several minutes in the lower atmosphere.

In the presence of a finite wind, the above-mentioned phenomena will further be complicated by a shearing effect of the atmospheric turbulent boundary layer. In addition to simple convection of the wake by the wind, the wind shear is expected to alter the relative motion of the two vortices.

---

[*] Laser Doppler Velocimeter

From observation, it is known that the downwind vortex often rises.

All the physical phenomena mentioned above - the vortex sheet, the buoyant exhaust, the wind profile and turbulence, ground images and vertical stratification - are modeled in the current analysis in two dimensions on a rectangular mesh. The continuous vorticity field is represented by a cloud of closely spaced discrete vortices. The airplane wake appears initially as a line of closely spaced vortices which subsequently wrap up and form the tip vortices. Except for the concentrated tip vortices, the velocity field is calculated at the mesh points from the Poisson equation relating the stream function to the vorticity. The vorticity itself is evaluated by calculating the local concentration of the discrete vortex cloud. Turbulence is simulated by adding a random additional term to the circulation of each vortex element in such a way as to guarantee a Kolmogoroff spectrum as the mean. Fast Fourier Transform techniques are used to solve for the velocity field at each time step. The individual vortices are then moved appropriately in this velocity field.

A primary effect which is not coupled into the model at present, but which may be important at early time, is the axial motion. However, the axial flow does not affect directly the transport of the trailing vortex except when it is drastically reduced. Until a three-dimensional approach is adopted, we shall not include this axial motion.

The laser doppler system is modeled by calculating the system response as the focal point is moved in range and elevation angle in the scan plane. When the system is focused at a given point in space, the Doppler spectrum response is calculated by considering contributions from each range point and superposing these, multiplied by a theoretical range response function. The velocity components are obtained from the hydrodynamical model at various times. A unique feature of the modeling of the hydrodynamics allows the tip vortices to be treated with high spatial resolution by invoking specific models of the core structure while at the same time retaining a lower resolution representation of the larger scale features. In the present analysis, we use Owen's model of the core structure and its decay. More accurate representations of the vortex structure are currently available (Betz, 1933; Donaldson, 1973) and can be included as required. The range response function is constructed from a previous analysis of the optical system for Gaussian beams. Effects of finite truncation and blocking of the primary mirror have been treated by a detailed two-dimensional propagation analysis. In the system model these effects are included by simply degrading the Gaussian beam analysis appropriately.

The spectrum is calculated by multiplying the aerosol density by the response function at each range point and cumulating this contribution in the appropriate velocity (or frequency) channel. The aerosol density in the neighborhood of the core is affected by centrifuging at late time, and a model for this has been developed (Appendix I). However, in the present simulation calculations, a uniform particle density is assumed.

Once the spectrum has been evaluated, simulations of the data analysis procedure are carried out. After specifying appropriate velocity and intensity thresholds, various moments of the spectrum are calculated (the mean velocity, variance, skewness and kurtosis). In addition, certain other characteristics of the spectrum are calculated: the velocity of the highest channel above threshold (V_{peak}), the velocity of the channel having the peak signal (V_{max}), the signal level in this channel (I_{peak}). All of these data, in addition to the fundamental input (the value of the parallel velocity at the particular range point) are presented on a (3-dimensional) range-elevation angle plot. Also plotted are the actual locations of the vortex cores. The geometry of the simulated laser scan pattern together with the vortex wake motion are separately displayed. This entire procedure is repeated for each time step of interest.

In the following section we give a detailed description of the hydrodynamic model followed by a description of the laser doppler system simulation. Example case histories are given in Section V for a simulation of a B747, a B720, and a DC-3. The DC-3 example is included to show comparisons with experimental LDV returns for a flight measurement. Detailed analyses of the LDV optics and the aerosol density evolution are relegated to appendices.

II.0 FORMULATION OF THE HYDRODYNAMIC MODEL

II.1 Equations of Motion

The momentum equation for an incompressible fluid may be written in the form

$$\frac{d\vec{u}}{dt} = - \frac{1}{\rho} \nabla p + \eta \nabla^2 \vec{u} + \vec{g} \qquad (1)$$

where $\vec{u}$ is the velocity, p the pressure and ρ the fluid density, η the kinematic viscosity, and $\vec{g}$ is the acceleration due to gravity. The vorticity

$$\vec{\zeta} = \nabla \times \vec{u} \qquad (2)$$

satisfies the equation obtained by taking the curl of Eq. (1):

$$\frac{d\vec{\zeta}}{dt} = - \nabla \frac{1}{\rho} \times \nabla p + \eta \nabla^2 \vec{\zeta} \quad . \qquad (3)$$

Thus vorticity is generated as a result of buoyancy forces associated with density and pressure gradients and diffusively dissipates as a result of viscosity. Eq. (3) provides a means for evaluating the vorticity of given fluid elements. The velocity at any point ($\vec{r}$) in the fluid may be evaluated from the integral of Eq. (2) which, in two dimensions, has the form

$$\vec{u}(\vec{r}) = \frac{1}{2\pi} \iint \zeta(\vec{r}\,') \times \frac{(\vec{r} - \vec{r}\,')}{|r - r'|^2}\, dx'dy' \qquad (4)$$

where the integral extends over the entire rotational region of the fluid. The continuity equation for an incompressible fluid:

$$\frac{d\rho}{dt} = \frac{\partial \rho}{\partial t} + \vec{u}\cdot\nabla\rho = 0 \qquad (5)$$

can be used to follow the evolution of the density distribution in time.

Instead of the Green's function form for the velocity field (Eq. 4), the velocity may be expressed in terms of a stream function $\vec{\Psi}$:

$$\vec{u} = \nabla\times\vec{\Psi} \qquad (6)$$

defined such that $\nabla\cdot\vec{\Psi} = 0$ (the vanishing of $\nabla\cdot\vec{\Psi}$ is automatically fulfilled in two-dimensional motion). The stream function satisfies a Poisson equation with the vorticity as the source function:

$$\nabla^2\Psi = \zeta \qquad (7)$$

for which the formal solution can be written

$$\Psi(\vec{r}) = -\frac{1}{2\pi}\int \zeta(\vec{r}\,')\,\ell n\,|\vec{r} - \vec{r}\,'|\,dx'dy' . \qquad (8)$$

The curl of this expression yields the identity in Eq. (4).

In the present analysis we will be concerned primarily with fluids where the fractional variation of the density and viscosities are small $\left(\frac{\Delta\rho}{\rho}, \frac{\Delta\eta}{\eta}, << 1\right)$ and we carry out calculations only to first order in these variations.

II.2 Numerical Procedure for the Inviscid Fluids

When the viscosity is negligible the vorticity equation (3) takes the form

$$\frac{d\vec{\zeta}}{dt} = -\nabla \frac{1}{\rho} \times \nabla p \tag{9}$$

and to first order in the density difference $\left[\text{since } p = \rho_o \vec{g} + o\left(\frac{\nabla \rho}{\rho}\right)\right]$,

$$\frac{d\vec{\zeta}}{dt} = -\frac{\nabla \rho}{\rho_o} \times \vec{g} \quad . \tag{10}$$

For the two-dimensional motion in the x, y plane the vorticity is effectively a scalar (i.e., has only a z component). Thus, for a vertical (y direction) downward gravitational acceleration g, Eq. (10) becomes

$$\frac{d\zeta}{dt} = \frac{g}{\rho_o} \frac{\partial \rho}{\partial x} \quad . \tag{11}$$

Of particular interest is the case of a stratified fluid. Here we divide the entire fluid into layers of slightly differing density. In this case, vorticity is generated only at the interface between the layers, the remainder of the flow remaining to be irrotational. It is convenient here to integrate Eq. (11) across the interface to yield an expression for the growth rate of the surface circulation density σ (circulation per unit length along the interface):

$$\frac{d\sigma}{dt} = \frac{g(\rho_+ - \rho_-)}{\rho_o} \sin\theta \qquad (12)$$

where ρ_+ is the density to the right of the interface and ρ_- that to the left, and θ is the angle of inclination of the interface (to the horizontal).

The total circulation of a given (i^{th}) fluid element $\vec{\Gamma}_i = \int \vec{\zeta}_i \, dx'dy'$ is determined by

$$\frac{d\vec{\Gamma}_i}{dt} = \frac{g(\rho_+ - \rho_-)}{\rho_o} \Delta y_i \, \vec{n}_z \qquad (13)$$

where Δy_i is the vertical separation between adjacent fluid elements on the interface and $\vec{n}_z$ is the unit vector perpendicular to the plane of motion.

A convenient numerical analysis of the evolution of the fluid motion can be obtained by dividing up the interface into a number of discrete fluid elements and approximating the circulation of each element as being concentrated into a line vortex having circulation Γ_i. The quantity Δy_i is then to be interpreted as the vertical separation between adjacent vortices. The evaluation of the fluid motion then reduces to the problem of following the motion of the individual discrete vortices. The velocity of the

i^{th} vortex is a summation over contributions from all other vortices:

$$\frac{d\vec{r}_i}{dt} = \vec{u}_i = \sum_{j \neq i}^{N} \frac{\vec{\Gamma}_i}{2\pi} \times \frac{(r_i - r_j)}{|\vec{r} - \vec{r}_j|^2} \quad . \qquad (14)$$

This equation of motion plus the relation determining the circulation growth rate (Eq. 13) in which Δy_i is replaced by $\frac{1}{2}(y_{i+1}-y_{i-1})$ yields a direct deterministic procedure for following the motion.

Equation (13) is the basis for calculating the vorticity due to the buoyant exhaust and its subsequent variation, and Eq. (14) is the conventional Green's function formalism. In practice, Fast Fourier Transform techniques are applied to solve Eq. (7). From the distribution of the discrete vortices, the continuous vorticity distribution is obtained by cumulating the vorticity in each cell[*]. From these the vorticity field is obtained and the Fourier components of the vorticity are then calculated. Fourier components of the stream function can be obtained from the Fourier transform of Eq. (7); that is

$$\psi_{\vec{k}} = \frac{-\zeta_{\vec{k}}}{(k_x^2+k_y^2)} \quad . \qquad (15)$$

The velocity field can be obtained most accurately by simple multiplication in Fourier space, rather than direct finite

---

[*] For the purposes of this cumulation, the vorticity due to each vortex is assumed to be smeared out uniformly over one mesh. This is a standard procedure for these types of mixed Lagrangian-Eulerian techniques.

differencing in physical space. Thus,

$$\vec{u}_k = \vec{k}\times\vec{\Psi}_{\vec{k}} \quad . \tag{16}$$

Transforming back to physical space we find the velocity of each discrete vortex by a bilinear interpolation from the nearest four space mesh points. The position of the vortices can then be advanced through the next time step.

II.3 Formulation of a Hybrid Vortex-in-Cell Method

The limitation of a purely FFT scheme, as presented in Section II.2, is its small time step. This time is essentially determined by the peak angular velocity of the tip vortex. Since angular velocities exceeding 10 radians per second are expected in some cases, the time step required to follow this motion would be substantially less than 0.1 second. To cover an elapsed time of 100 seconds requires more than 1000 steps. This is excessive and it is desirable to obtain a numerical scheme which can handle the same number of vortices without the limitation of a small integration time step.

For the present study, there is another reason that a purely FFT scheme will not be adequate. In order to resolve a vortex flow field which has a core radius of a few meters, one must have a mesh smaller than the core radius. On the other hand, one must cover an overall dimension determined by the product of the wind speed and the total elapsed time of interest (several hundred meters). The ratio of this dimension to the core radius indicates that at least 100 mesh points in each direction are required to resolve the flow field, and this is large even for the CDC 7600. To achieve an economical and accurate computation we introduce a hybrid method which is capable of resolving the fine structure near the tip vortex while maintaining a relatively coarse mesh.

We utilize the fact that the vortex sheet quickly coagulates into two (or more) well defined localized structures which maintain their identity for many rotations. The total velocity field is taken to be a superposition of two parts: one the contribution of the localized tip vortices and the other due to the more distributed vorticity. The velocity field of the tip vortex we construct from an axisymmetric model. This model in general requires values of two quantities to be specified: the total vortex circulation $\Gamma(t)$, and a characteristic radius R (typically the core radius). Both Γ and R can be functions of time. In the present simulation we use the model constructed by Owen (1970) for a turbulent vortex and for which $R = \frac{2}{\sigma} \sqrt{\nu t}$ and $\sigma = \frac{1}{\Lambda} (\nu/\Gamma_o)^{\frac{1}{4}}$ where Λ is a numerical value of order unity (and is set equal to 1 in the present simulation). A simple laminar diffusion profile is used for the radial distribution of circulation $\left\{\Gamma \sim \Gamma_o\left[1 - \exp(-r^2/R^2)\right]\right\}$. As the core expands, the distributed vortices may be captured and incorporated into the tip vortices. The tip vortex locations are updated to the centroid of the original vorticity distribution in this capture process. The velocities due to the tip vortices and the wind shear are then superposed.

In practice, one avoids the short time step problem by superposing displacements rather than velocities. The angular displacements directly induced by the tip vortices are evaluated. This displacement is then added to that due to the slowly varying background velocity field. By repeating this process at each time step one follows accurately the motion near the core even though a given point may rotate several times about the tip vortex during one time step.

II. 4 Calculation of the Circulation of the Vortex Sheet

By Prandtl's lifting line theory, the vorticity shed from the high aspect ratio wings is parallel to the direction of flight and the flow in the neighborhood of any one section of the wing is approximately two dimensional and independent of the neighboring sections. This seems to be valid for most of the present day transport aircraft (excluding SST's). For low aspect ratio wings, the framework laid out in this study is still applicable except that a three-dimensional formulation must be utilized to model the initial distribution of circulation. Until practical application warrants the complication, we shall assume the hypotheses in Prandtl's theory applies.

By wing theory, the lift or wing loading is linearly proportional to the circulation about the wing cross section, and it is well known that for simple high aspect wings the wing loading can be approximated by the elliptic curve

$$\frac{S(x)}{S_o} = \sqrt{1 - \left(\frac{x}{R}\right)^2} \qquad (17)$$

where S_o is the maximum circulation at $x = 0$ and R is the wing span (Figure 1). The circulation between the point x and x+dx is decreased by the amount $\Delta S = S(x+dx) - S(x)$ and this amount of circulation must be shed from the wing section between these two points. The cross section at AA' (Figure 1) indicates this variable strength vortex sheet. (This shed vortex sheet should not be confused with the starting vortex shed from a two-dimensional wing section. Section BB' in Figure 1 shows this starting vortex.) Thus, the circulation of the trailing vortex sheet at Section AA' is equal to the rate of change of S(x), that is, $-\frac{dS(x)}{dx}$ along the wing.

To model this initial velocity field we divide the vortex sheet into a number of strips in the z direction, each segment of which has a circulation $\Gamma_i(x)$ given by

$$\Gamma(x_i) = \left[S(x_i) - S(x_{i+1})\right]/\Delta x \tag{18}$$

where $\Delta x = x_{i+1} - x_i$.

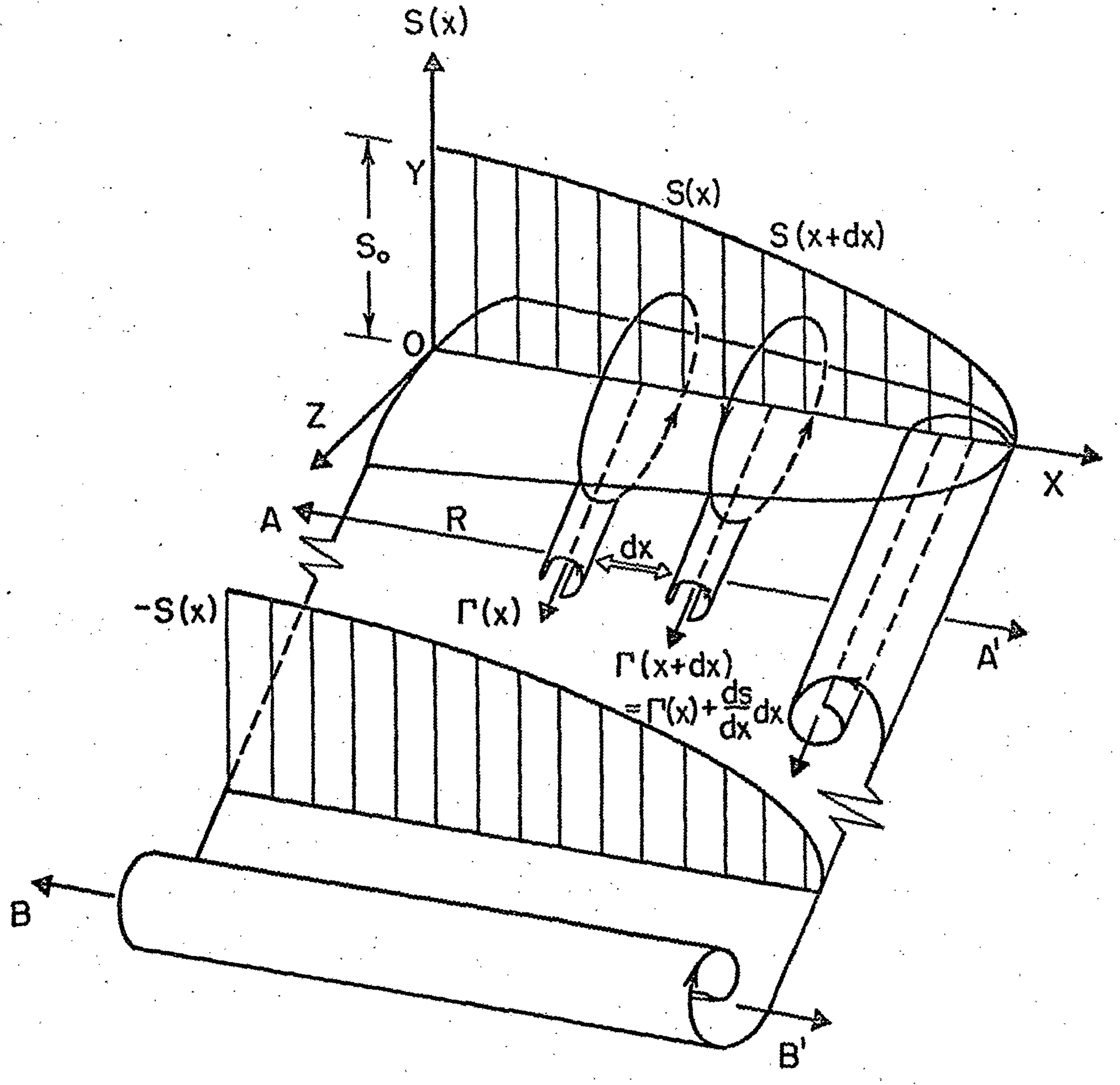

R is the wing span

Figure 1. Determination of the strength of the aircraft trailing vortex.

II.5 Simulation of the Turbulent Wind Shear Field

The wind profile near the ground in a neutrally-stable atmosphere is known to exhibit a logarithmic dependence upon the height y (Blackadar and Tennekes, 1968)

$$U = \frac{u_\tau}{\kappa} \ln \left(1 + \frac{y}{y_o}\right) + \text{constant} \tag{19}$$

where u_τ is the friction velocity and is usually related to the wind velocity by the relation $u_\tau \cong \frac{1}{30} U_{(\text{at standard height})}$. The parameter κ is the Kármán constant and is equal to .42 (Hinze, 1959). The parameter y_o is the roughness height.

From Eq. (19) the vertical wind shear can be obtained by taking the derivative with respect to y:

$$\zeta(y) = \frac{u_\tau}{\kappa y} \quad . \tag{20}$$

To describe the mean wind shear field, this circulation is assigned to a uniform distribution of discrete vortices as follows:

$$\Gamma_o = \frac{U_\tau}{\kappa} \ln \left(1 + \frac{\Delta y}{2y_o}\right) \Delta x \qquad \text{for } j = 1$$

and

$$\Gamma_j = \frac{U_\tau}{\kappa} \ln \left(\frac{Y_j + \Delta y/2}{Y_j - \Delta y/2} \right) \Delta x \qquad j=2,\ldots 17 \tag{21}$$

where Δx, Δy are the horizontal and vertical mesh sizes. The present treatment is similar to that of Brashear and Hallock (1973) except for the number of wind shear vortices used to simulate the wind shear field. In the present analysis, the introduction of the mixed Eulerian-Lagrangian coordinates (a particle-in-cell method) allows a highly detailed spatial resolution of the wind field at relatively modest cost.

The mean wind profile is assumed prescribed at time $t=0$ and is independent of horizontal location. To simulate the turbulence we seek a realization of the turbulent wind field assuming the Kolmogoroff -5/3 law applies and the dissipation rate is constant throughout the flow field. In essence, the turbulence is assumed to be represented by constructing, at time = 0, a random field of vortices with the fluctuating velocity field satisfying the Kolmogoroff law (in expectation).

Let the fluctuating velocity component be represented by a Fourier series,

$$\vec{u}(\vec{x}) = \sum_{\vec{k}=0}^{\infty}\sum \vec{u}(\vec{k}) \exp(i\vec{k}\cdot\vec{x}) \quad , \qquad \vec{k} = (k_x, k_y)$$

where the $\vec{u}(\vec{k})$ is the Fourier component of the $\vec{u}(\vec{x})$. A specific realization can be determined from:

$$|\vec{u}(\vec{k})| = - < \vec{u}(\vec{k}) > \quad \ell n(1-r_1)$$

or

$$= -\left(\iint_{\vec{k}-\frac{1}{2}\Delta\vec{k}}^{\vec{k}+\frac{\Delta\vec{k}}{2}} \frac{c\varepsilon^{\frac{2}{3}} k^{-\frac{8}{3}}}{2\pi} dk_x dk_y\right)^{1/2} \quad \ell n(1-r_1)$$

where r_1 is an equidistributed random number in (0,1) and $k = \sqrt{k_x^2 + k_y^2}$, $c \cong 1.52$ and ε is the dissipation rate. Since $\vec{u}(\vec{k})$ is in general complex, a random phase must also be introduced; this yields

$$\vec{u}(\vec{k}) = -\left[\iint_{\Delta\vec{k}} \frac{c\varepsilon^{\frac{2}{3}} k^{-\frac{8}{3}}}{2\pi} dk_x dk_y\right]^{1/2} \quad \ell n(1-r_1) \; \exp(i2\pi r_2)$$

where r_2 is also an equidistributed random number in (0,1). Taking curl of this relation in $\vec{x}$ space, the vorticity is obtained and the circulation strength of each vortex can be calculated by integrating over the mesh $\Delta x \; \Delta y$

$$\Gamma(\vec{x}) = F^{-1}\left\{2i\left[u(\vec{k})k_x - v(\vec{k})k_y\right] \frac{\sin\left(k_x\frac{\Delta x}{2}\right)}{k_x} \frac{\sin\left(k_y\frac{\Delta y}{2}\right)}{k_y}\right\} \qquad (22)$$

where Δx, Δy are the mesh sizes and F^{-1} represents the inverse Fourier transform.

This circulation is added to the time independent wind shear given by Eq. (21) at initial time, the subsequent motion is then determined by the interactions among the vortices.

III.0 SPECTRAL SIGNAL CHARACTERISTICS FOR COAXIAL LDV SYSTEMS

III.1 Signal-to-Noise Ratio

Coherent heterodyne laser detection systems are commonly operated in a shot noise limited condition; that is, the noise is determined entirely by the number of scattered photons detected, not by the receiver electronics. The performance of a general coherent laser system detecting the radiation scattered from a continuously distributed aerosol has been analyzed previously. In the special case of a coaxial system (that is, the received scattered signal is collected through the transmitting optics), the signal-to-noise ratio is given by

$$S/N = \frac{\eta P_\omega}{2\Delta\omega} \left(\frac{\lambda}{\pi\gamma}\right)^2 \int_0^\infty \frac{\overline{\sigma n}_f(L)}{(L-L^*)^2 + \Delta L^2} \, dL \quad . \tag{23}$$

Here $\overline{n_f \sigma}$ is the differential backscattering crosssection per unit range per steradian, η the overall loss factor (atmospheric absorption, optics and electronics), P_ω the transmitter power that is scattered into the bandwidth $\Delta\omega$ (i.e., $P_\omega \Delta\omega$ is proportional to the number of photons transmitted which would be scattered into the frequency interval $\Delta\omega$ in an ideal system). We have assumed that both transmitter and receiver have a Gaussian apodization with radii R_t and R_r, respectively, at the e^{-2} intensity points.

The transmitted wave fronts are focused at a range f_t and the receiver section is focused at f_r. The focal point for the receiver is determined by locating the position of the virtual image of the local oscillator. In terms of these optics parameters, the various parameters in Eq. (23) are given by the relations

$$\gamma = \sqrt{\theta_{geom}^2 + \theta_{diff}^2}$$

$$\theta_{geom} = \sqrt{\left(R_r^2 + R_t^2\right)}/f_2$$

$$\theta_{diff} = \lambda\sqrt{R_T^2 + R_r^2/\ R_t R_r}$$

$$f_1 = \left(\frac{R_r^2}{f_r} + \frac{R_t^2}{f_t}\right)\Bigg/\left(\frac{R_r^2}{f_r^2} + \frac{R_t^2}{f_t^2}\right)$$

$$f_2 = \left[\frac{R_t^2 + R_r^2}{\dfrac{R_r^2}{f_r^2} + \dfrac{R_t^2}{f_t^2}}\right]^{1/2}$$

$$L^* = \frac{f_1}{1 + (\lambda f_2/\pi R_t R_r)^2}$$, λ is the wavelength

and

$$\Delta L = \left\{ \left[\frac{\lambda f_1/\pi R_t R_r}{1 + \left(\frac{\lambda f_2}{\pi R_t R_r} \right)^2} \right]^2 + \frac{\left[\frac{R_r R_t}{\left(R_r^2 + R_t^2 \right)} \left(\frac{f_2}{f_t} - \frac{f_2}{f_r} \right) \right]^2}{\left[1 + \left(\frac{\lambda f_2}{\pi R_t R_r} \right)^2 \right]} \right\}^{1/2} f_2 \ .$$

When the atmospheric backscattering properties of the doppler signal vary negligibly across the depth of field $\pi \Delta L$, the signal-to-noise ratio takes the form

$$S/N = \frac{\pi}{2} \frac{\eta P}{\Delta\omega \Delta L} \left(\frac{\lambda}{\pi \gamma} \right)^2 \overline{n_f \sigma} \left(\frac{1}{2} + \frac{1}{\pi} \tan^{-1} \frac{L^*}{\Delta L} \right) \quad . \qquad (24)$$

In order that significant range resolution be achieved, the aperture must be chosen so that ΔL is small compared to L^*, i.e., so that the scattering particles are well within the near field ($\lambda f/\pi R^2 << 1$). In this limit, the signal-to-noise is independent of range

$$S/N = \eta \frac{P}{\Delta\omega} \ \overline{n_f \sigma} \ \frac{\lambda}{4} \qquad (25)$$

and the range resolution (the region from which comes half the scattered energy) is $\pi \Delta L = \lambda L^2/R^2$.

The signal-to-noise given in Eq. (23) represents a mean value averaged over the band width $\Delta\omega$. When the receiver channel width exceeds the doppler width of the scattered signal, $\Delta\omega$ is to be set equal to the receiver channel bandwidth. When the doppler spread is large enough to cover more than one receiver channel, $\Delta\omega$ is to be set equal to the doppler width of the incoming signal. In this case, the signal-to-noise is independent of the individual receiver channel bandwidths.

When the magnitude of the scattered power changes only slightly in a time equal to the reciprocal of the individual receiver channel bandwidths, further improvement in the signal-to-noise ratio can be achieved by incoherent integration of the power level at the output of the receiver channels. The increase is essentially equal to $\sqrt{\Delta\omega_c \tau_i}$, where τ_i is the allowed integration time and $\Delta\omega_c$ the receiver channel bandwidth.

For optimum performance, the integration time should be matched to the dwell time. In the current LDV system, the receiver channel width is 100 kHz, and dwell times range from 1 to 10 milliseconds, yielding potential increases in signal-to-noise of factors of 3 to 10.

III.2 Spectral Response

A typical configuration for a single LDV system is shown in Figure 2a. In the scan plane there are 21 beams at 1.5° apart, each covering a range between 60 and 150 meters. Superimposed in the same figure is the location of the trailing vortex sheet. The parallel velocities along each line of sight, versus range, are presented in Figure 2b. These plots would indicate the response of an LDV system which had infinitely high range resolution. At large lateral separations from the vortices, that is, at the top and bottom of the figure, only a very weak velocity perturbation is seen. As the line of sight gets closer to the vortex, the velocity peaks at the vortex location (C). However, if the line of sight passes directly through the vortex only a small component of velocity parallel to the line of sight is obtained (B). Lines of sight which pass between the vortex pair sense both vortices (A). The peak value of the parallel velocity changes sign as the line of sight crosses the vortex center and maximizes at the edges of the core.

The finite range resolution smears out this velocity profile to a greater or lesser extent depending on range. The LDV system senses the doppler spectrum as averaged over the range response function of the instrument. Various moments or mean properties of the velocity spectrum may be calculated from the relation

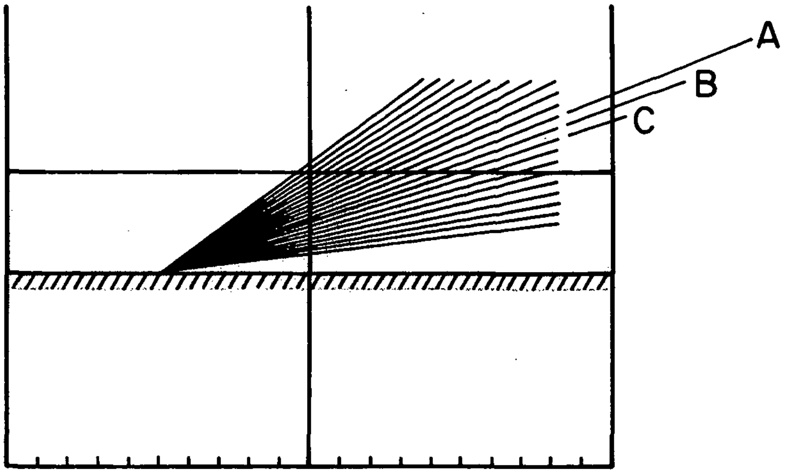

Figure 2a. LDV fan beam configuration

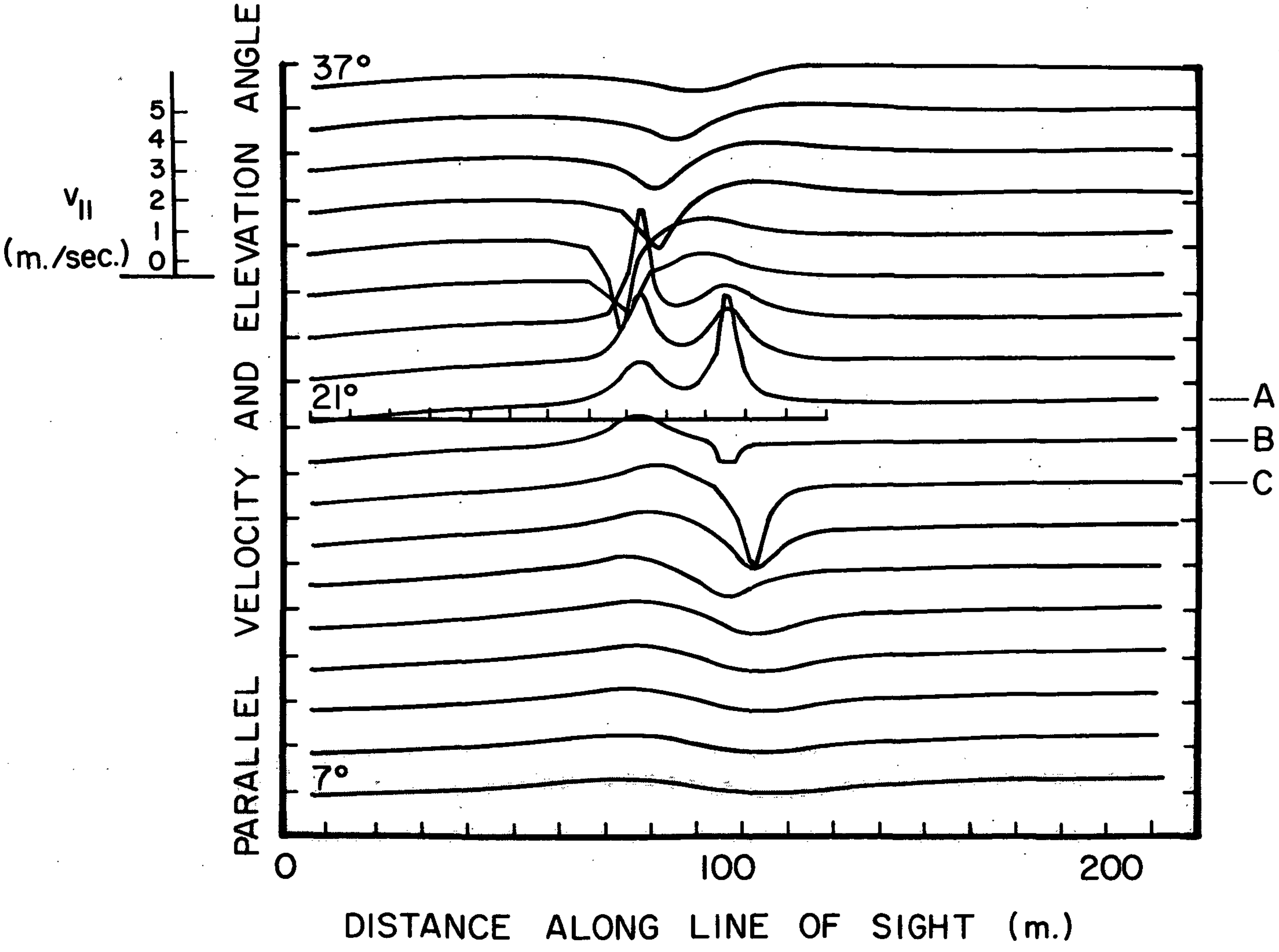

Figure 2b. r,Θ-Plot for the Parallel Velocity (V_{11})

$$\overline{f}(s,\theta) = \int^{\infty} f(V_{\shortparallel})\ I(s,\theta,V_{\shortparallel})dV_{\shortparallel} \bigg/ \int I(s,\theta,V_{\shortparallel})dV_{\shortparallel} \qquad (26)$$

where $I(s,\theta,V_{\shortparallel})$ is the doppler spectral intensity. This intensity in turn depends on the atmospheric backscattering properties and the range response function $g_s(s,s')$. For Gaussian aperture apodization, the range response function has the form

$$g_s(s,s') = \frac{1}{\left[1 + 4\left(\frac{s-s'}{\Delta s}\right)^2\right]} \qquad (27)$$

where Δs is the range resolution (between 3db points):

$$(\Delta s)_{\text{gaussian}} = 2\,\frac{\lambda}{\pi}\left(\frac{s}{R}\right)^2 \qquad (28)$$

Here s is the range to the focal point and R is the aperture radius (e^{-2} intensity). To account for finite truncation of the telescope mirror in the simulation model, we simply degrade the resolution by a fixed factor:

$$\Delta s = 2f\,\frac{\lambda}{\pi}\,(s/R)^2 \quad . \qquad (29)$$

Detailed propagation calculations have been carried out to examine the effects of finite apertures and blocking of the mirror. For a Gaussian beam truncated at the e^{-2} radius, f is computed to be 2.1.

Two modes of operation are possible, in general: one where the sign of the doppler shift is sensed and the other where only the magnitude is used. All of the calculations presented in this report assume the latter mode although either or both modes can be implemented.

To demonstrate the nature of the output available, three test examples of the simulation have been run, two for large aircraft (B747, B720) and one for a DC-3.

The calculation of the spectrum begins with the parallel velocity profile versus range. When the system is focused at the range s the spectrum level in the velocity channel V_k is obtained from a finite difference representation of

$$I(s,\theta,V_k) = I_o \int_0^\infty \frac{\overline{n\sigma}(s')g_V\left(V_{\parallel}(s') - V_k\right) ds'/\Delta s}{\pi\left[1 + 4\left(\frac{s-s'}{\Delta s}\right)^2\right]} . \qquad (30)$$

Here $g_V(\delta V)$ is the frequency response of the filter and is taken to have the form

$$g_V(\delta V) = \frac{1}{\left[1 + \left(2\frac{\delta V}{\Delta V}\right)^{2p}\right]} \qquad (31)$$

where ΔV is the velocity resolution (0.545 meters/sec in the current simulation) and p is a parameter. The value p = 1 gives a reasonable representation of the actual filter function in the NASA/MSFC system whereas $p \to \infty$ gives the square box filter. No great differences are expected between different values of p. The current demonstration calculations have all assumed $p = \infty$.

In Figure 3, we show typical distributions of aerosol sizes in continental air. The signal-to-noise for the heterodyne signal is proportional to the mean value of the product $\overline{n\sigma}$:

$$\overline{n\sigma} = \int_0^\infty \gamma_{180} \sigma_T(a) \frac{dn}{da} \, da \qquad (32)$$

where σ_T is the total scattering cross section and γ_{180} the backscattering efficiency.

The backscattering efficiency for particles is defined as 4π times the ratio of the scattered intensity per unit solid angle at backscatter to the total scattered intensity. Diermendjian has calculated the angular dependence of scattering for haze at a wavelength of 0.7μ (see Figure 4). A backscattering efficiency of 0.15 has been evaluated from these data by numerical integration. For rough estimates we will estimate σ by the approximate expression

$$\sigma_T \approx 2\pi \, a^2 \qquad \text{for } a > \lambda/2\pi$$

$$\sigma_T \approx 0 \qquad \text{for } a < \lambda/2\pi \quad . \qquad (33)$$

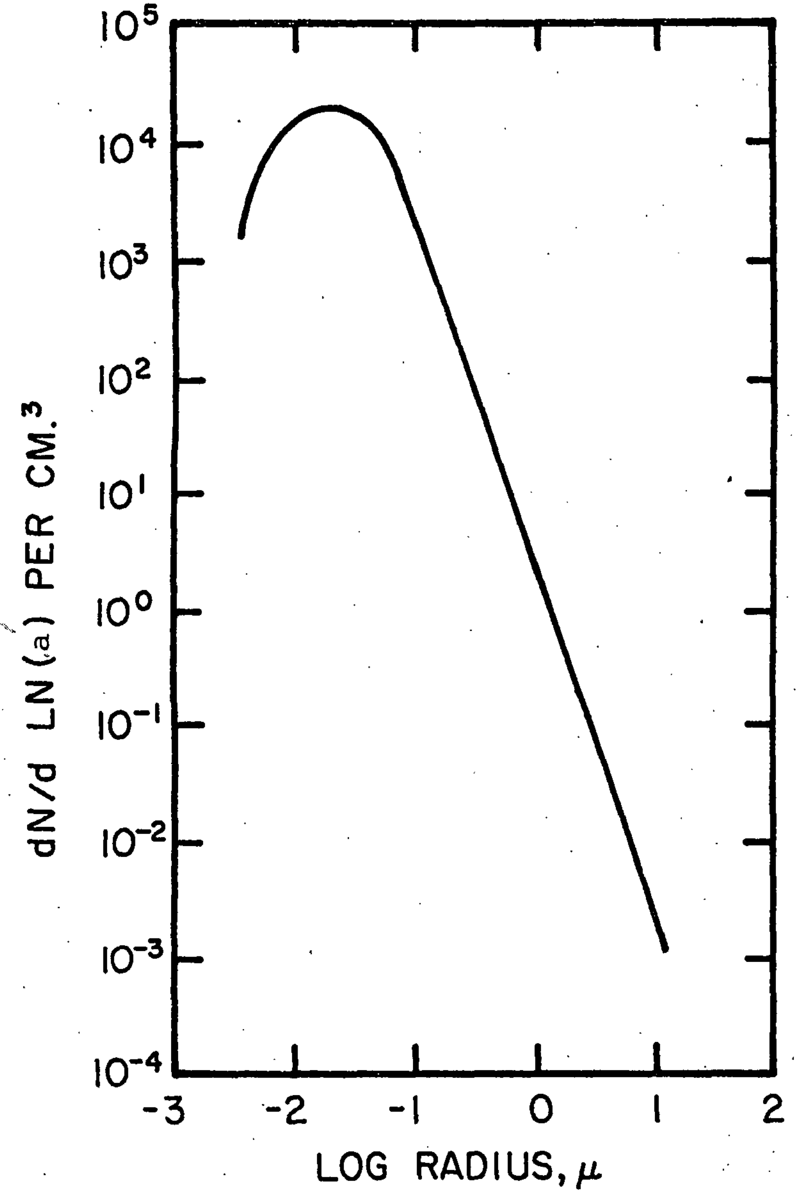

Figure 3. Aerosol size distribution

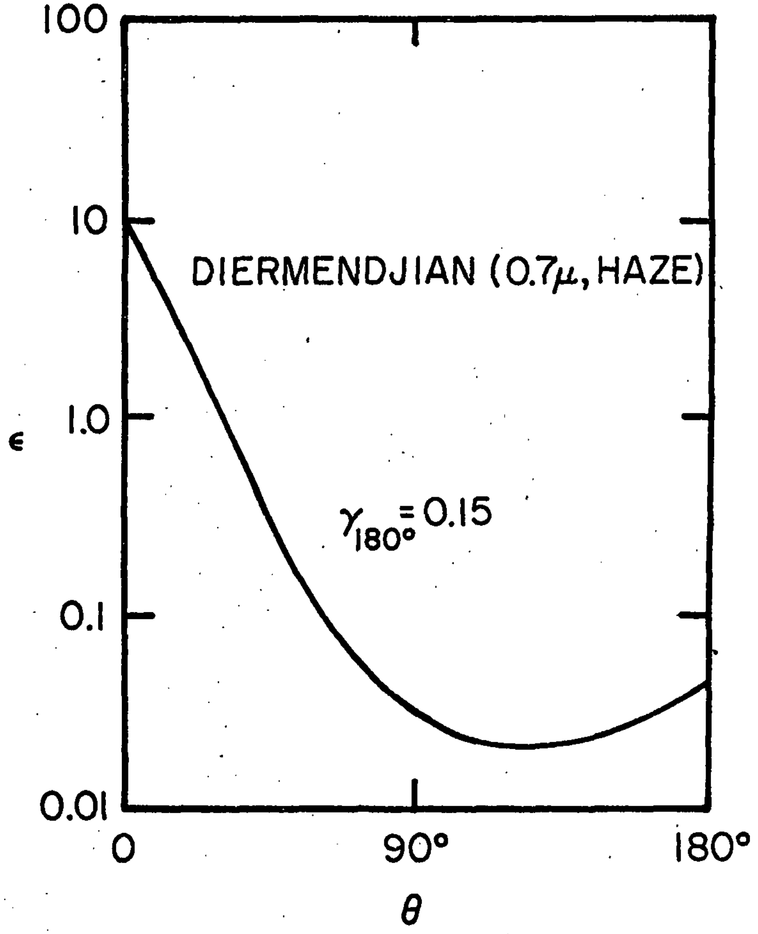

Figure 4. Angular dependence of aerosol scattering

In continental air the particle size distribution may be roughly represented in the form[12]

$$\frac{dn}{da} \approx n_o a_o^3 / a^4 \ \text{cm}^{-4} \qquad (34)$$

for a > 1000 Å. Thus, the mean value of $n\sigma$ is roughly given by

$$\overline{n\sigma} \approx 4\pi^2 \ \gamma \, n_o a_o^3 / \lambda \quad . \qquad (35)$$

From the Handbook of Geophysics model of continental air $n_o \approx 2$ particles/cm^3 when a_o is chosen equal to 1 micron. Thus,

$$\overline{n\sigma} \ = 7.89 \times 10^{-11} \ \gamma/\lambda \ \text{cm}^{-1} \quad .$$

At 6000 Å, $\overline{n\sigma}$ is 0.132 γ per km and at 10.6μ is 0.00744 γ per km. These values of the total scattering coefficient and the inverse wavelength dependence are in good agreement with the detailed calculations by McClatchey, et al. (1971), for his clear air model (see Figure 5). For other atmospheric conditions, $\overline{n\sigma}$ may be deduced from the value of the visual range L_V (visibility) which is defined as $3.9/\overline{n\sigma_T}$. Thus, at backscatter

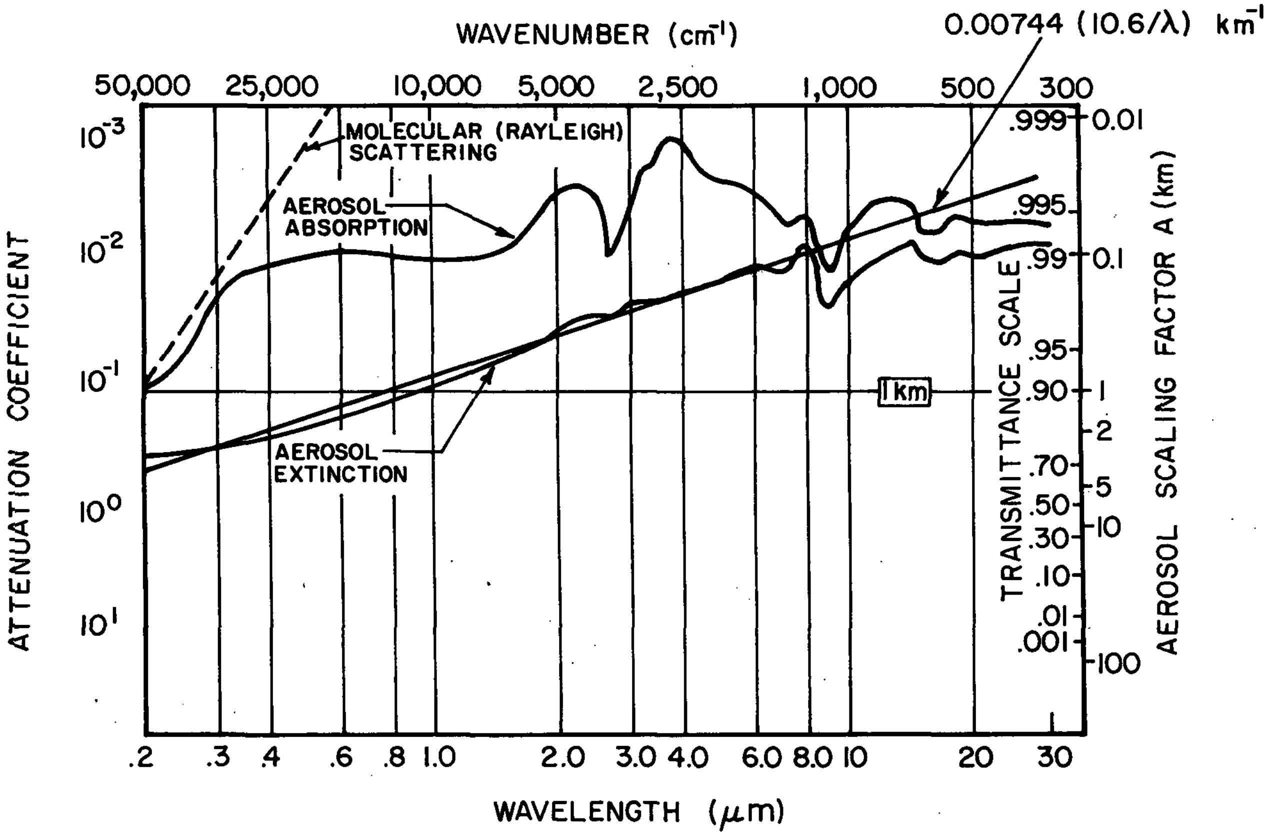

Figure 5. Attenuation Coefficients (per km) for Aerosol Transmittance (Absorption and Total Extinction)

$$(\overline{n\sigma})_{vis} \approx 3.9\ \gamma/L_V \approx 0.6\ L_V \quad . \qquad (36)$$

At 10.6μ, the model clear air backscatter cross section is (using $\gamma = 0.15$ and into 4π steradians)

$$\overline{n\sigma}_{10.6\mu} = 1.12\times10^{-8}\ \text{cm}^{-1}$$

$$= 0.0011\ \text{km}^{-1} \quad .$$

Per steradian, the model differential backscatter cross section is at sea level for clear air

$$\frac{d(\overline{n\sigma})}{d\Omega} = 8.91\times10^{-5}\ \text{km}^{-1}\ \text{ster}^{-1} \quad .$$

Values of the signal-to-noise per joule of energy transmitted are shown in Figure 6 . These values assume no incoherent integration and the relevant energy for a CW system is the energy transmitted in a time equal to the reciprocal of the signal bandwidth. Thus, at short ranges the total signal-to-noise ratio for a 10 watt laser with a 100 KHz bandwidth, an overall efficiency (optics, detector, electronics, atmospheric transmission, scattering losses) of 0.6% is expected to be of the order of 10^3 (30db). With 10 milliseconds of incoherent integration this would be increased to 40db. If the signal bandwidth (due to the velocity gradients)

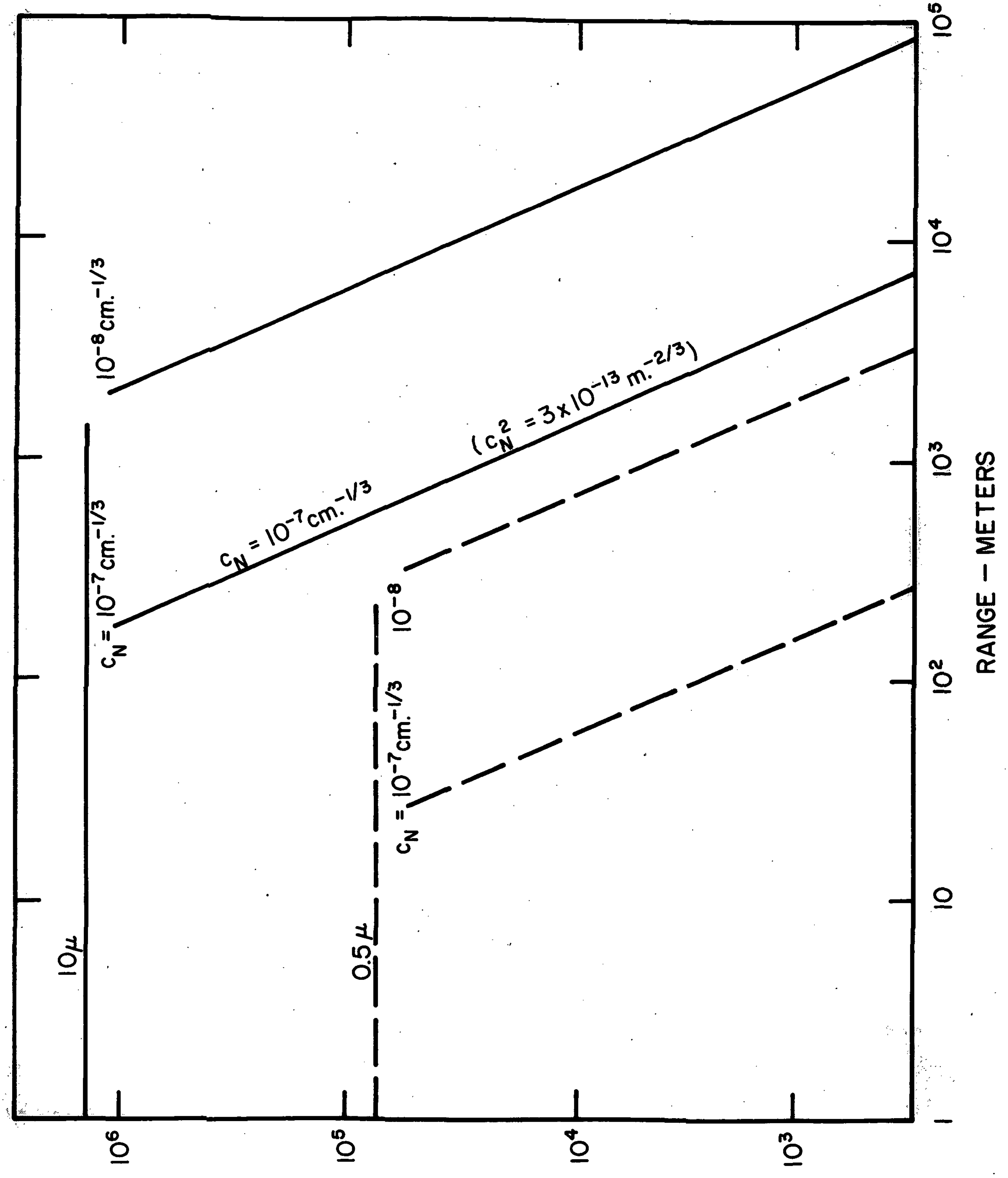

Figure 6. Signal-to-noise per joule vs. range (Continental air)

were spread over 20 channels, the signal-to-noise ratio per channel would be reduced to 17db with no integration and 27db with integration (summing the signal over all 20 channels would yield an additional 6.5db for a total signal strength measurement).

Thus, the expected signal-to-noise ratios at short range are high. Turbulence will degrade the signal quality at long range. For values of C_n^2 of order $3\times10^{-13}\ m^{-2/3}$, significant degradation is expected (for a 30 cm aperture) at ranges beyond 150 meters.

Centrifugal effects near the vortex core will reduce the aerosol density within the core and enhance it in the region surrounding the core. A simple analysis is carried out in Appendix I to derive the aerosol density profiles expected. Here, at the time t, an expression is given for the ratio of the density at a given radius from the vortex center (r) to its initial value:

$$\frac{n(a,r,t)}{n_{amb}(a)} = \mathcal{f}\left(\frac{r}{R}, \frac{t}{T(a)}\right) \tag{37}$$

where a is the particle radius, R the vortex radius and T(a) the centrifuging time given by

$$T(a) = 2.25 \frac{\rho_{air}}{\rho_{part}-\rho_{air}} \frac{\nu}{a^2} \left(\frac{2\pi R}{\Gamma}\right)^2 \quad .$$

Here Γ is the vortex circulation. The scattering cross section according to Eq. (32) may be approximated by

$$\overline{n\sigma}(r,t) = 2\pi \int_{a=\lambda/2\pi}^{\infty} n_{amb}(a)\, f\left[\frac{r}{R}, t/T(a)\right] a^2\, da \,. \qquad (38)$$

Values of the backscattering cross section are plotted as a function of radius from the vortex core for various times in Figure 7. Close to the axis it may be shown that

$$f(r/R, t/T) \rightarrow e^{-t/T} \quad .$$

Thus, at $r = 0$,

$$\overline{n\sigma}(0,t) \simeq 2\pi n_o a_o^3 \int_{\lambda/2\pi}^{\infty} e^{-\frac{a^2 t}{a_o^2 T_o}}\, da/a^2$$

where we have taken $n_{amb}(a) = n_o a_o^3/a^4$ and $T_o = T(a_o)$. In other words,

$$\overline{n\sigma}(0,t) \simeq 2\pi\, n_o a_o^2 \sqrt{\frac{t}{T_o}} \int_{\frac{\lambda}{2\pi a_o}\sqrt{\frac{t}{T_o}}}^{\infty} e^{-u^2}\, du/u^2 \quad . \qquad (39)$$

At early time $\left(\frac{t}{T_o} < 2\pi a_o/\lambda\right)$

$$\overline{n\sigma}(0,t) \approx \frac{4\pi^2 n_o a_o^3}{\lambda}\left(1 - \sqrt{\frac{t}{t_1}}\right) \qquad (40)$$

where

$$t_1 = \left(\frac{2\pi a_o}{\lambda}\right)^2 T_o = 88.8 \frac{\rho_a}{\rho_p}\frac{\nu}{\lambda^2}\left(\frac{2\pi R^2}{\Gamma}\right)^2$$

$$= 1.185\times 10^4 \left(\frac{2\pi R^2}{\Gamma}\right)^2 \text{ seconds} = 1.176\ T(a=2\mu) \quad .$$

The term t_1 is the time for centrifugal effects to substantially alter the local backscattering cross section within the vortex core.

For small high-velocity cores, these centrifuging times are relatively short. (For a B707, t_1 is 10 seconds or less for core diameters less than about 10 feet - see Table A-I.1 in Appendix I.) Thus, small high speed cores may be visible as an enhancement of the scattering around the periphery of the vortex.

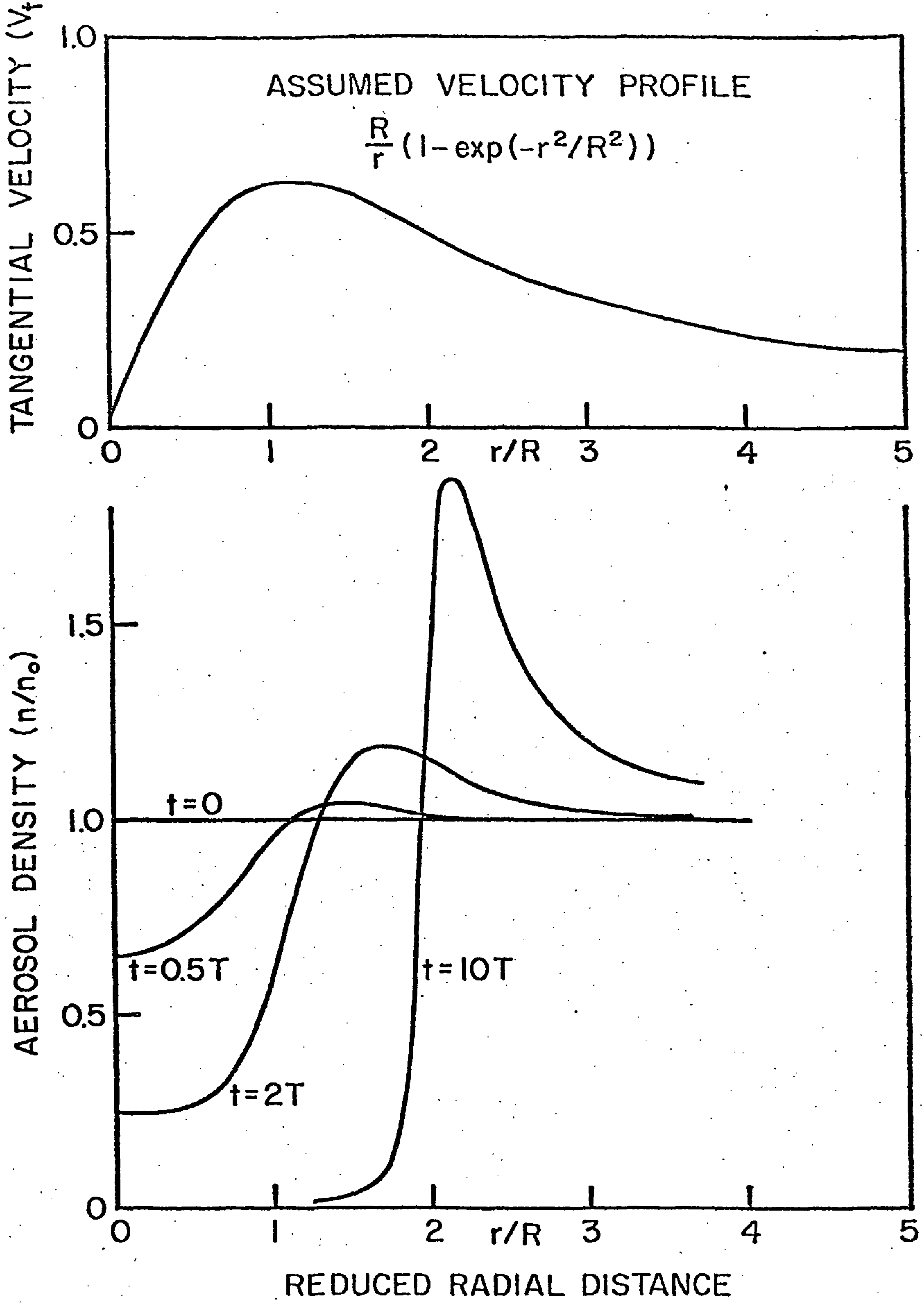

$$\left[\ T = 2.25 \left(\frac{\rho_a}{\rho_p - \rho_a}\right) \frac{\nu}{a_p^2} \left(\frac{2\pi R^2}{\Gamma}\right)^2\ \right]$$

Figure 7. Aerosol density at various times

IV.0 LDV SIMULATION CODE

A model of the hydrodynamic and laser system described in the preceding sections is formulated as a numerical computer program. This program calculates as a function of time the response of a pair of LDV scanning systems which view the region below and near the aircraft track. Each system is described by a prespecified number of equally-spaced lines of sight which uniformly cover elevation angles between a given maximum and minimum value. In the present formulation, the program "tracks" the wake, locates the elevation angle of the mid-point between the two tip vortices and automatically centers the elevation angle scan on this point. At regularly spaced time intervals, the simulated LDV system response is calculated as a function of range (to some maximum range) for each elevation angle.

The output of the program is displayed in a series of plots. The vortex sheet shed from the aircraft wing, as well as the tip vortices are first presented on an x-y plot along with the locations of all the distributed wind shear vortices. This general orientation plot is complimented by a velocity vector plot which shows the overall velocity field. The LDV system configuration is displayed by superposing individual lines of sight of the two beams on a plot of the vortex sheet location.

The LDV system response is calculated from the distribution of the parallel wind velocity component along each line of sight. Before presenting simulations of the system response, a high resolution 'three-dimensional' plot of this parallel velocity component is presented. This is the basic quantity sensed by all doppler radar backscatter systems (laser, acoustic or microwave). Here the velocity is plotted versus range for each elevation angle and an entire scan frame is presented in a single range-elevation angle plot. Curves for different elevation angles are displaced in the vertical direction by an amount proportional to the angle.

The doppler spectral intensity I(V) is then calculated (according to the prescription in Section III) at each point in space. Because of the large amount of data, only samples of these spectra at selected elevation angles are presented.

After the spectrum is computed, a number of spectral moments are determined. At present there are ten different variables or moments that are calculated at each range-elevation point. These are:

1. The parallel velocity $U_{\parallel}$: the actual component along the line of sight as computed directly from the hydrodynamic model.

2. The (unrectified) mean parallel velocity ($\overline{V}_1$): this is the parallel velocity simply averaged over the theoretical range resolution function

$$\overline{V}_1(s) = \int_0^\infty g_s(s-s')\, u_\parallel(s')\, ds' \Big/ \int_0^\infty g_s(s-s')ds'. \quad (41)$$

3. The (rectified) mean parallel velocity $\overline{V}$: this is the parallel velocity as sensed by the LDV system with finite range resolution:

$$\overline{V} = \sum_{|V_k|>V_o} \left[I(k) - I_o(k)\right] |V_k|/I_{sum}. \quad (42)$$

Here V_k is the velocity of the kth channel, I(k) the computed intensity in this channel, $I_o(k)$ a threshhold intensity level (to be discussed subsequently), and V_o a velocity threshhold. I_{sum} is the total intensity in all channels (above threshhold):

$$I_{sum} = \sum_{|V_k|>V_o} (I(k) - I_o(k)) \quad . \quad (43)$$

In all moment calculations, no contribution is included for intensities below a given intensity threshold (i.e., only nonzero contributions for $I(k) > I_o(k)$ are allowed).

In this computation the system is assumed incapable of distinguishing positive from negative doppler frequencies.

4. The velocity variance σ:

$$\sigma = \left[\sum_{|V_k|>V_o} (|V_k| - \overline{V})^2 \ (I(k) - I_o(k))/I_{sum} \right] . \qquad (44)$$

5. The skewness β:

$$\beta = \sum_{|V_k|>V_o} (|V_k| - \overline{V})^3 \ (I(k) - I_o(k))/I_{sum} . \qquad (45)$$

6. The kurtosis κ:

$$\kappa = \sum_{|V_k|>V_o} (|V_k| - \overline{V})^4 \ (I(k) - I_o(k))/I_{sum} . \qquad (46)$$

7. The peak velocity (V_{peak}):
The velocity of the highest frequency channel having a spectral intensity exceeding the threshhold value (and if $V_{peak}>V_o$).

8. The velocity of the maximum intensity (V_{max}):
The velocity of the channel having the highest value of $I(k) - I_o(k)$ and for which $V_k>V_o$.

9. The maximum intensity (I_{peak}):
The largest value of $I(k) - I_o(k)$ for all velocities greater than V_o.

10. Sum of intensity (I_{sum}):
The total signal strength above the intensity and velocity thresholds:

$$I_{sum} = \sum_{|V_k| > V_o} (I(k) - I_o(k)) \quad . \qquad (47)$$

All of these quantities are presented in the range-elevation angle plots described previously. To illustrate the relationship between the variations of each variable and the tip vortices, we have also superposed on the plots the location of the vortex sheet and the tip vortices.

V.0 SIMULATION CASE HISTORIES

V.1 B747 Simulation.

A simulation of the trailing vortex wake of a Boeing 747 aircraft at a height of 61 meters (200 ft.) above the runway using a 32×32 grid was carried out. The vortex sheet was represented by 25 discrete vortices distributed over half the wing span, each assigned a circulation according to Eq. (18). The wind shear vorticity is distributed over the flow domain on a 17×32 mesh, and the ground images are obtained by the symmetry condition in the vertical direction. A single cylindrical region under each wing is used to represent the engine exhausts. Circulation may be ascribed to the 25 vortices outlining this region to simulate the effect of buoyancy. However, no buoyancy is actually present in any of the simulations presented in this report.

Figure 8a shows a Boeing 747 trailing vortex sheet and its exhausts at initial time. On each grid point, there is a wind shear vortex with strength determined by Eqs. (21) and (22). The four downward arrows indicate the reference points of the initial geometry; all the dimensions are in KMS units. Figure 8b shows the velocity vector plot, including the trailing vortices, wind shear vortices, and their images; the maximum flow speed is represented by the length indicated on the upper left corner. There is a vertical downwash induced by the lift on the wing and the wind profile is significantly altered by the presence of the vortex sheet - notice the flow is opposite to the wind direction under the upwind tip vortex. Figures 9 and 10 show the rolling up of the vortex sheet at elapsed times of 6 and 12 seconds. The computation uses a 32×32 mesh over a physical dimension of 240m×240m and takes .426 seconds per time step (on a CDC 7600 computer); the time step is $\Delta t = .08$ second. A complete run of the total elapsed time of 60 seconds would require about 5 minutes CPU time.

In these calculations, no attempt was made to treat the tip vortices as discrete entities. As a consequence, even when the time step is as small as 0.08 seconds, substantial numerical noise is apparent by 12 seconds in the region near the vortex cores. A simple calculation of the vortex sheet by Westwater (1936), which is confirmed in the present calculation, shows that most of the vorticity is essentially concentrated into two well-defined tip vortices within a few seconds. For this reason, the hybrid computation method was adopted for all subsequent calculations. A repeat of this particular simulation with a 32×32 grid then allowed an integration time step of one second with satisfactory results (see Figures 11 a,b,c. This has greatly improved the computation efficiency. Figure 11 shows the overall picture of the vortex

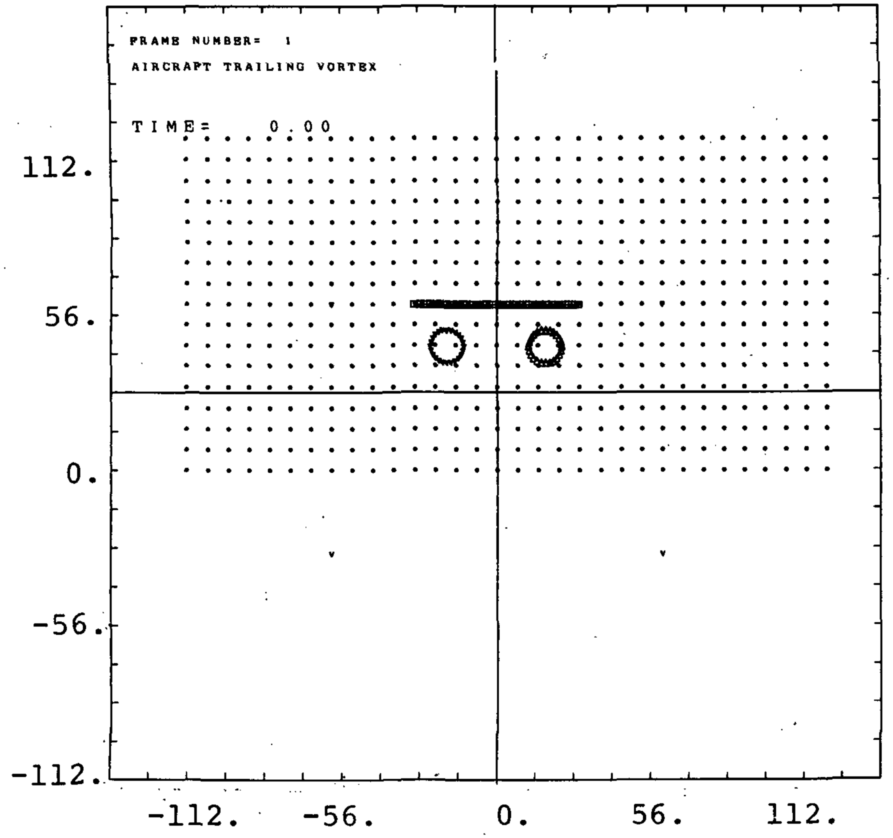

Figure 8a. Initial aircraft trailing vortex configuration.

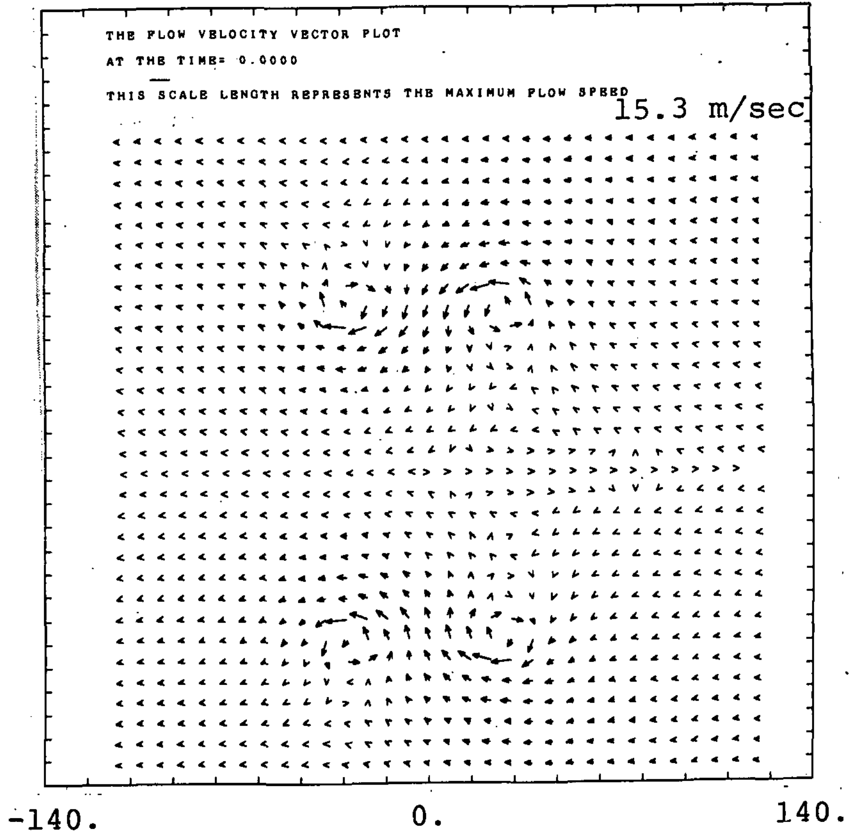

Figure 8b. Velocity vectors for the initial trailing vortex configuration.

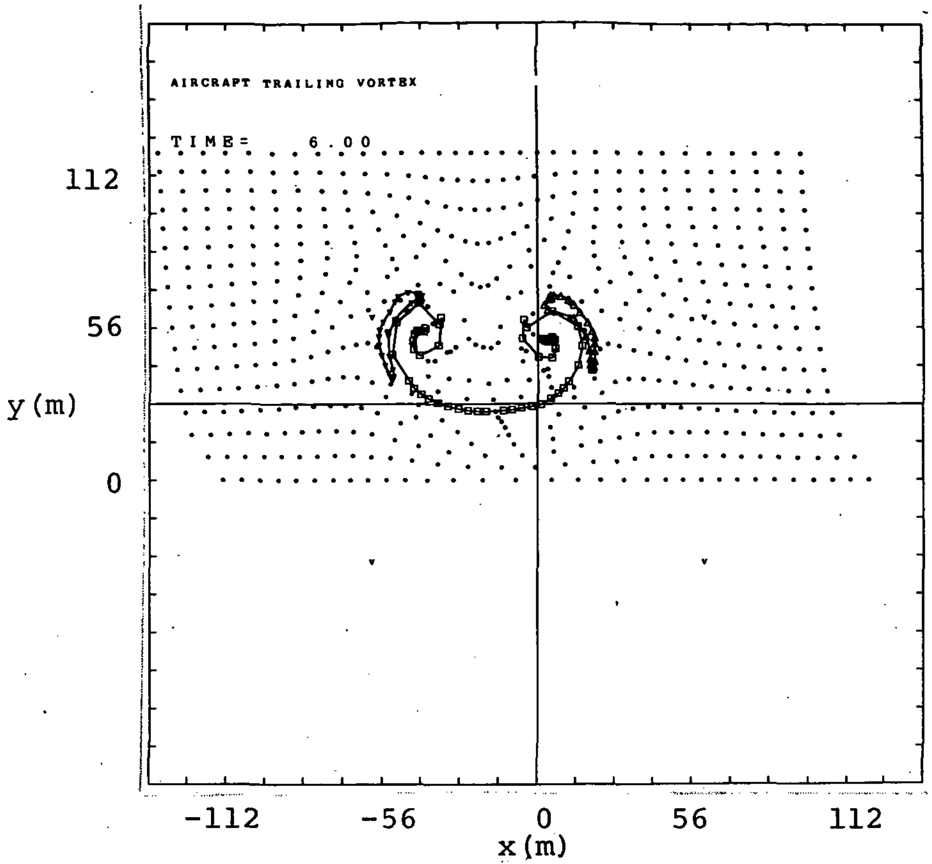

Figure 9. Trailing vortex configuration at 6 seconds

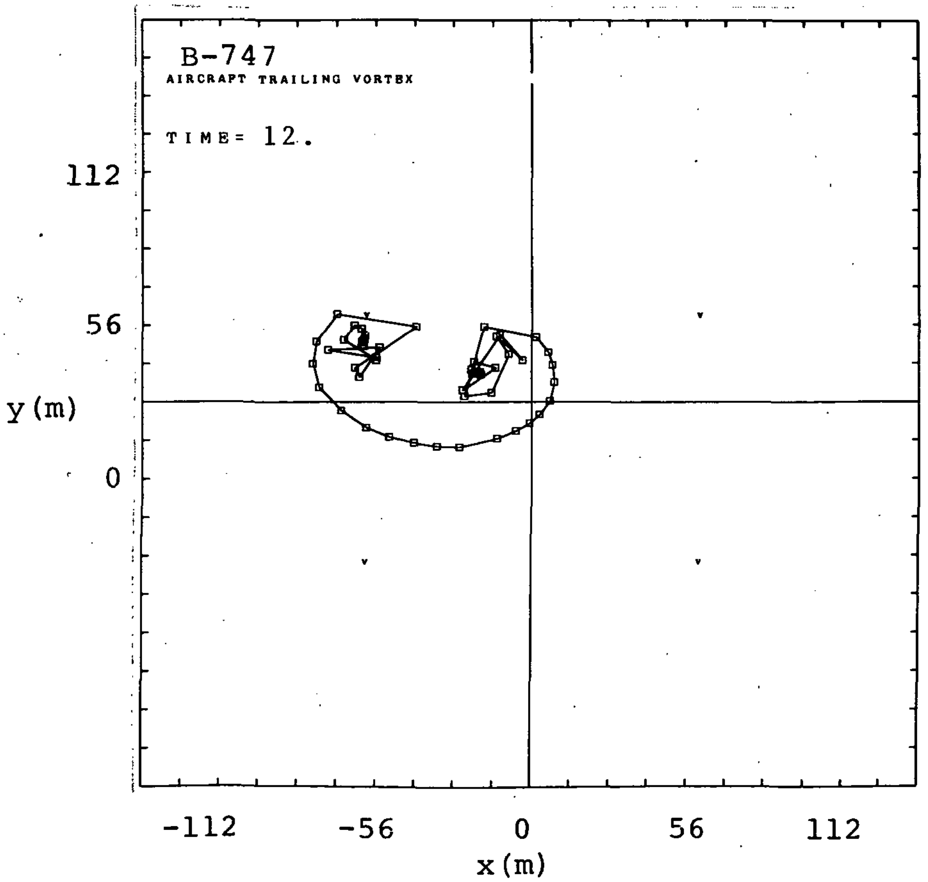

Figure 10. Trailing vortex configuration at 12 seconds.

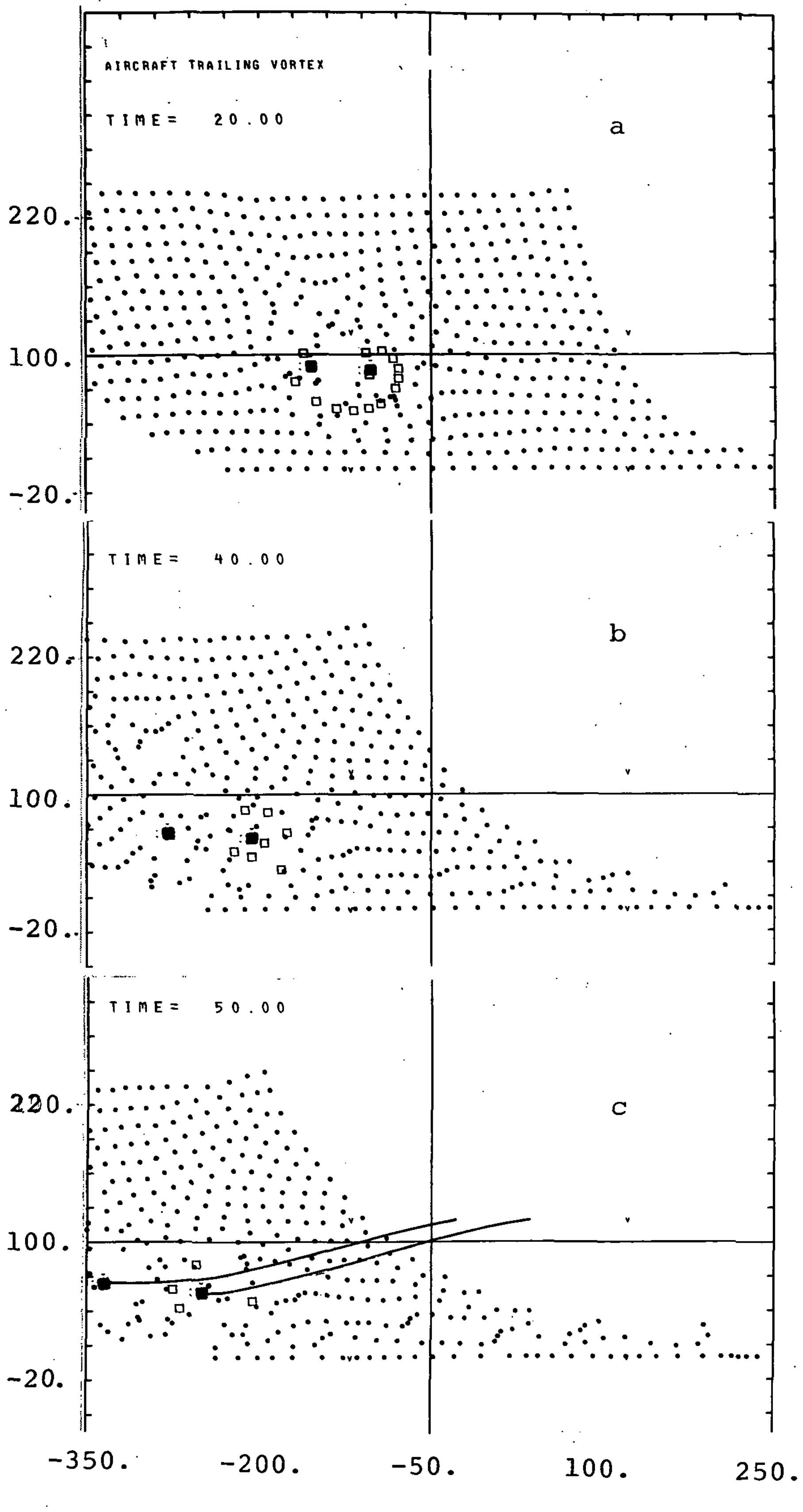

Figure 11abc. Trailing vortex configurations at 20, 40 and 50 seconds.

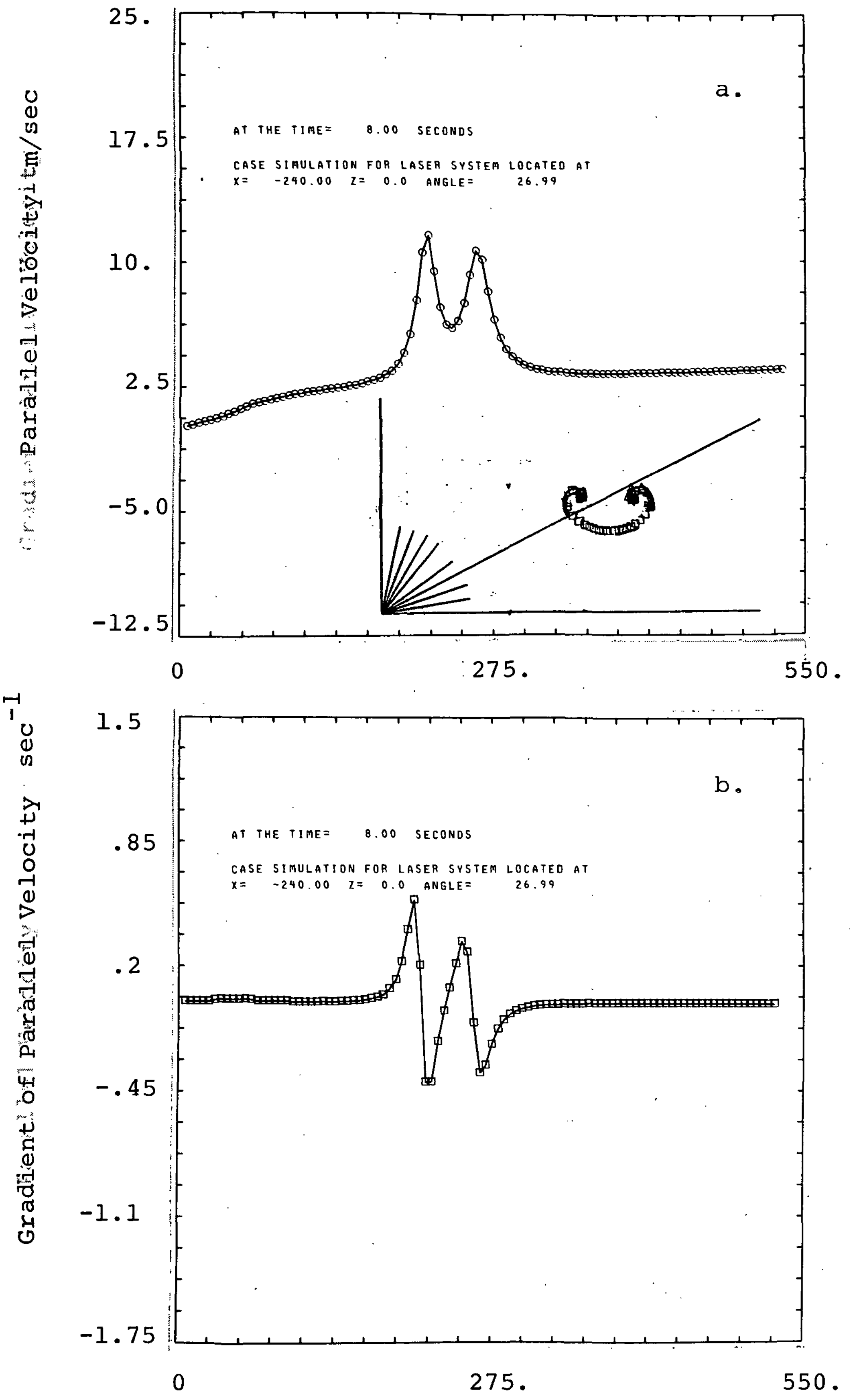

Figures 12a & b. Parallel velocity and gradient of the parallel velocity along a line of sight at 6 seconds.

system at times up to 50 seconds. At late time the wind shear vortices near the ground where the vorticity is maximum are swept up by the vortex wake and effects of the interaction between the wind shear and the tip vortices may be expected to appear. In Figure 11b, a tilting of the two vortices becomes apparent at time t = 40 seconds. The trailing vortices are transported nearly 300 meters to the left from the original position, and the position of the wind shear vortices delineate clearly the wind profile. Notice that when vortices are swept out of the boundary of the flow domain, the periodic condition implied by the Fourier transform requires that the total vortices be replenished but at one periodic length displaced from their original position. One can always choose a domain large enough to avoid the influence of the periodic images. The trajectories of the tip vortices are given in Figure 11c.

No LDV system responses were calculated for this B747 simulation. However, the two basic hydrodynamic quantities which are essentially measured by the system are shown in Figures 12 and 13, the local parallel component of the flow velocity and its gradient along the line of sight. The latter quantity is proportional to the doppler spectral width or (square root of) the spectral variance for a backscatter system having good spatial resolution.

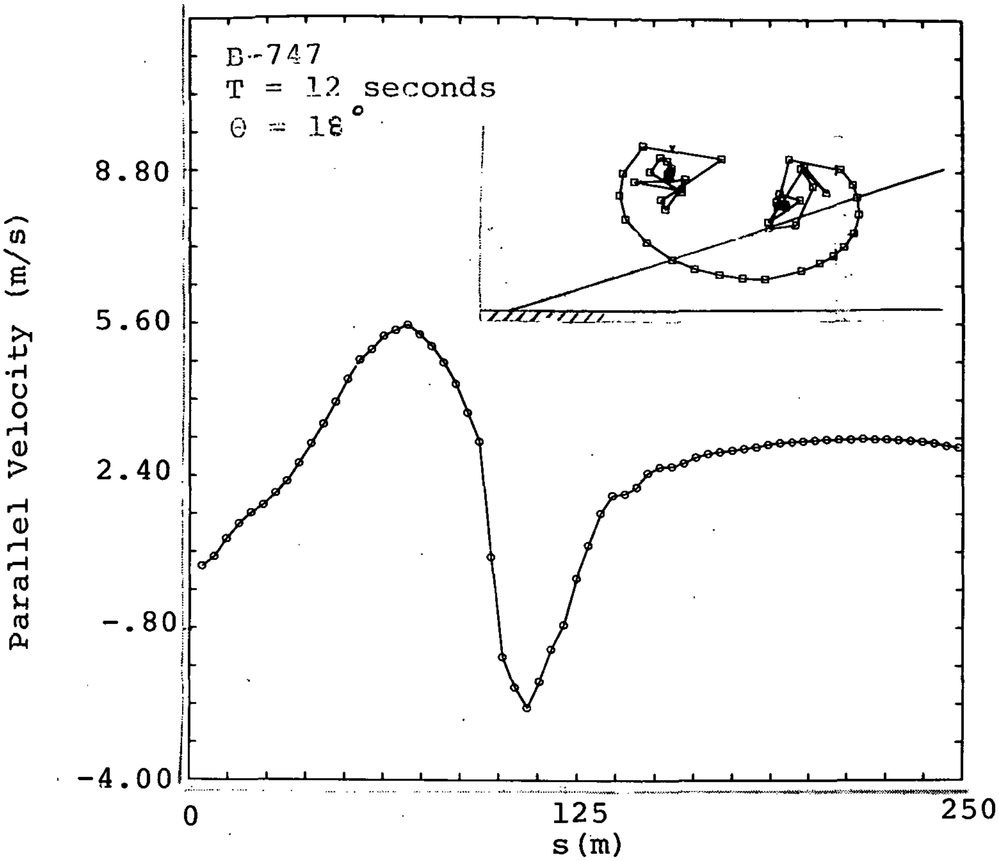

Figure 13a. Parallel velocity along line of sight at 12 seconds

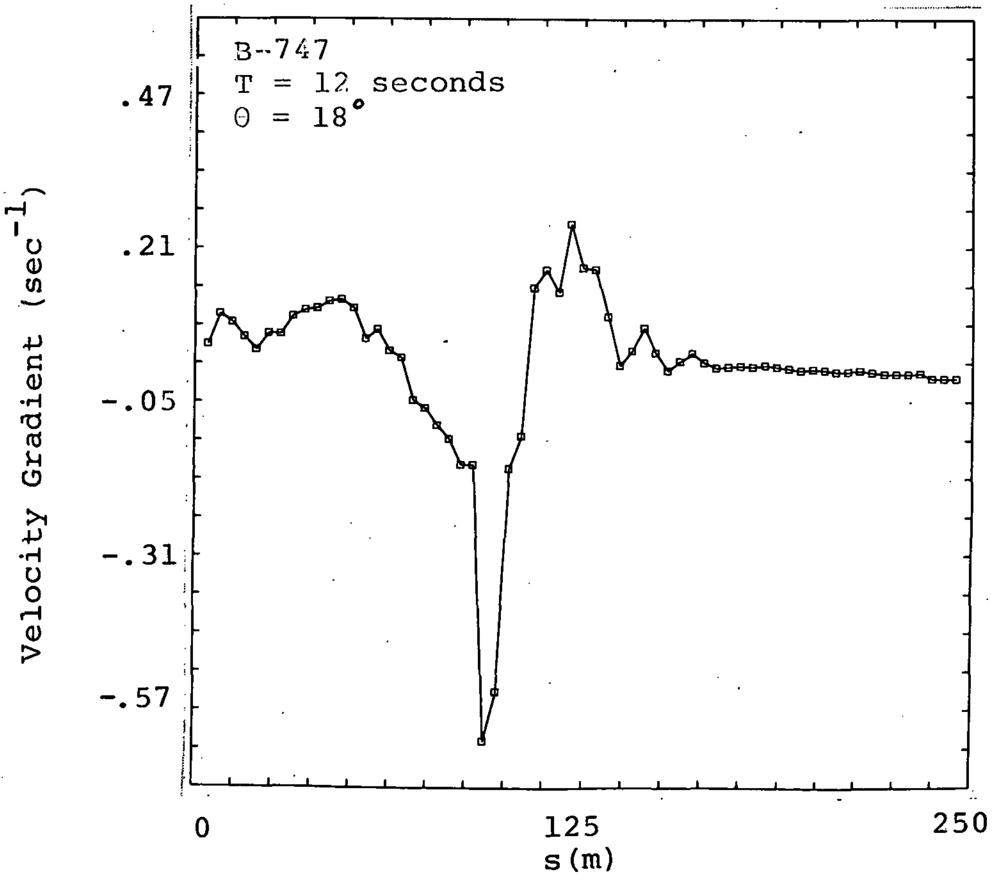

Figure 13b. Gradient of the parallel velocity along a line of sight at 12 seconds

V.2 DC-3 Simulation

Data were obtained from a DC-3 fly-by at NASA-MSFC in January 1974. Although precise aircraft properties (particularly height and atmospheric wind properties) are not available for this measurement, data were obtained at relatively close range and clear signatures were observed in the processed data. An approximate simulation for this fly-by was constructed and the results are shown in Figures 14 through 17.

The overall geometry of the simulation is shown in Figure 14. The actual parallel velocities are shown in Figure 15 for different elevation angles and a simulation for selected lines of sight of the LDV response (with zero thresholds) is shown in Figure 16. In Figure 17, we compare the mean velocity from the simulation at a computed time of 28 seconds with data observed at a time of 7 seconds after penetration of the aircraft through the scan plane. No particular significance is placed on the time difference since the aircraft position and the ambient winds were imprecise. In any case, the vortex structure changes little in the first 30 seconds. The simulation of the mean velocity shows a number of interesting features: first, for the three lines of sight that pass between the two vortices, both vortices are discernible as separate peaks in the range profile. However, when a line of sight passes almost through one of the vortices, that vortex is not visible and the other only gives rise to a broad maximum.

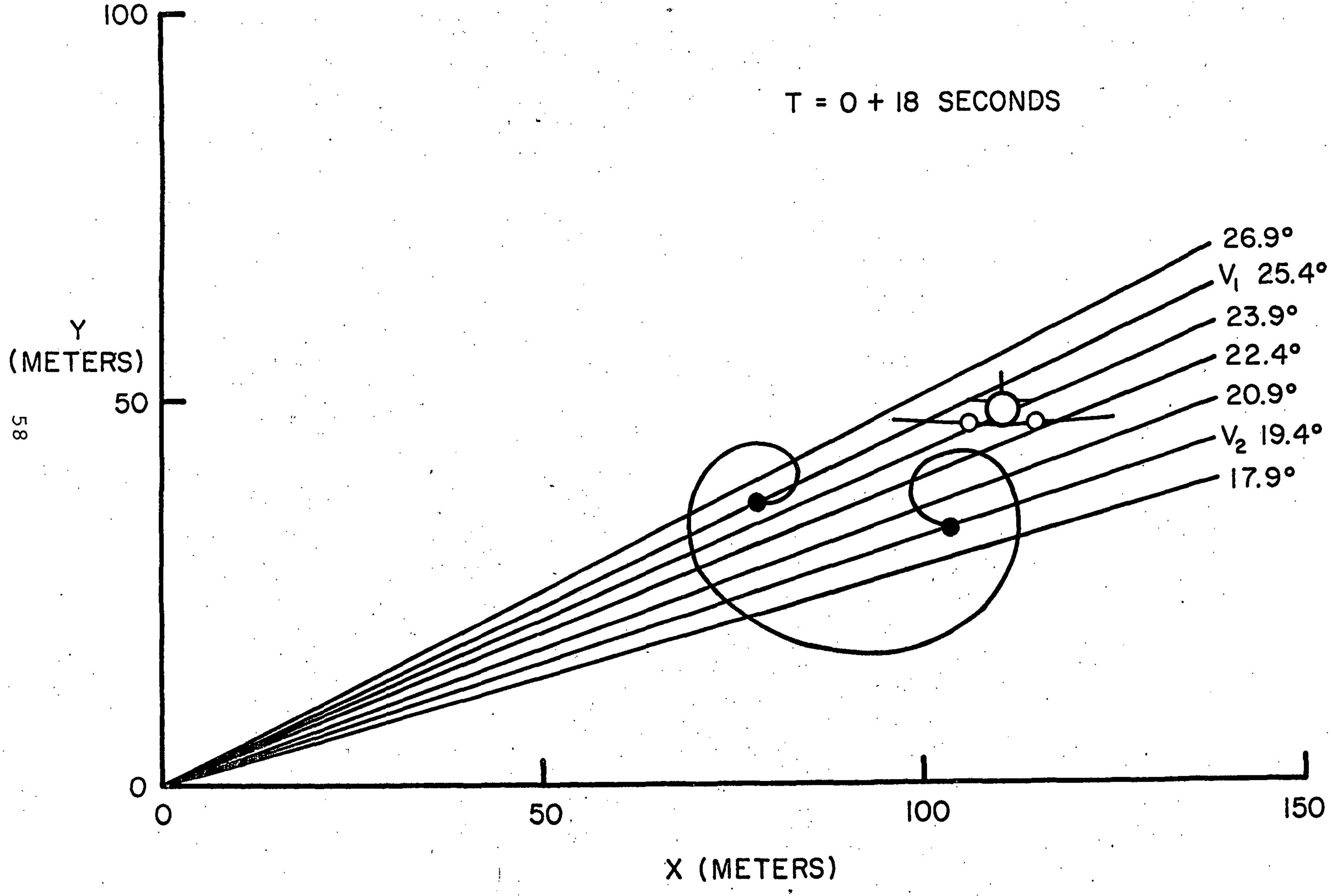

Figure 14. Line of sight geometry at 18 seconds

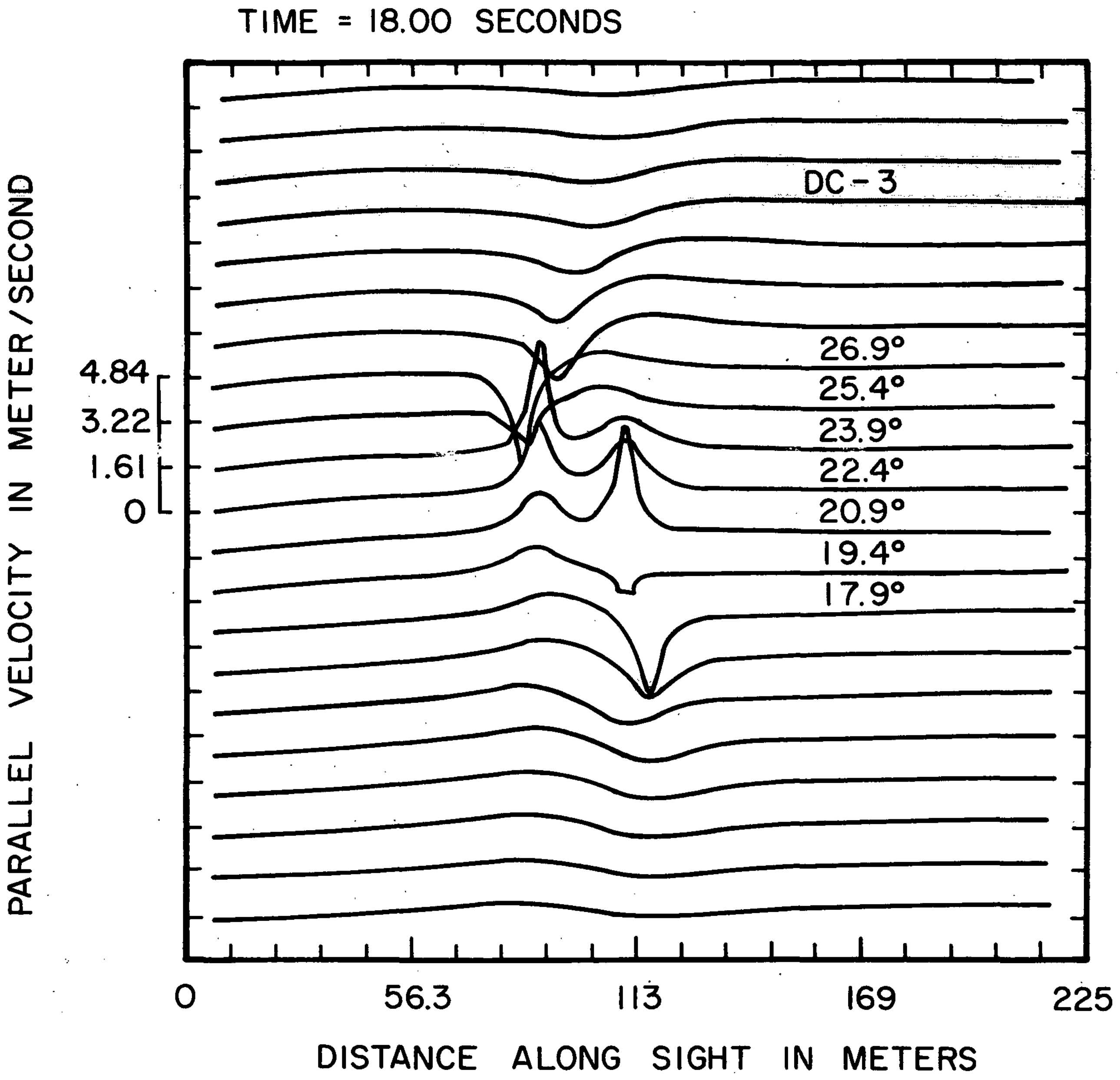

Figure 15. Theoretical Parallel Velocity vs. Range at 8 Seconds (DC-3 Simulation)

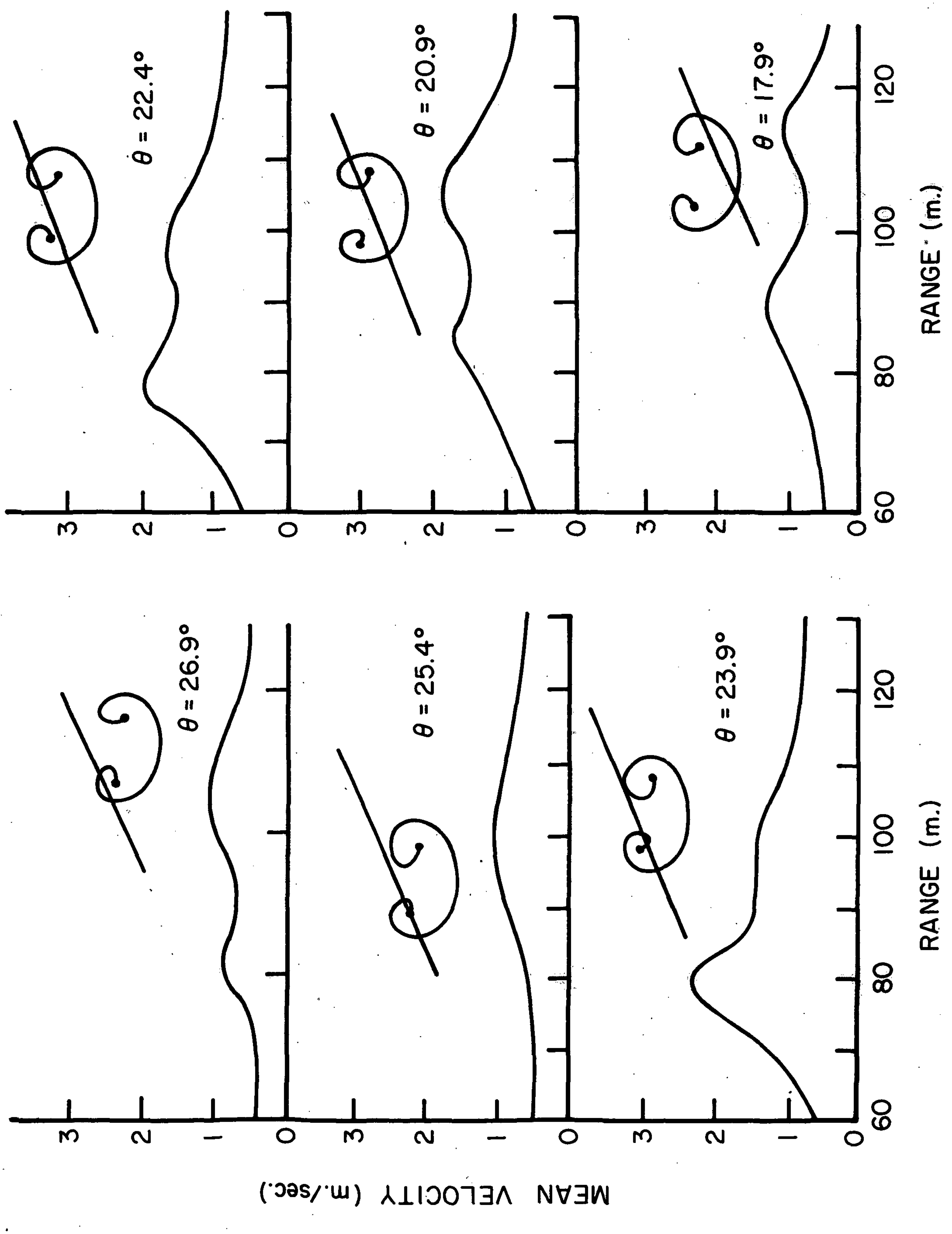

Figure 16. Mean Velocity Deduced from a Simulation of a DC-3

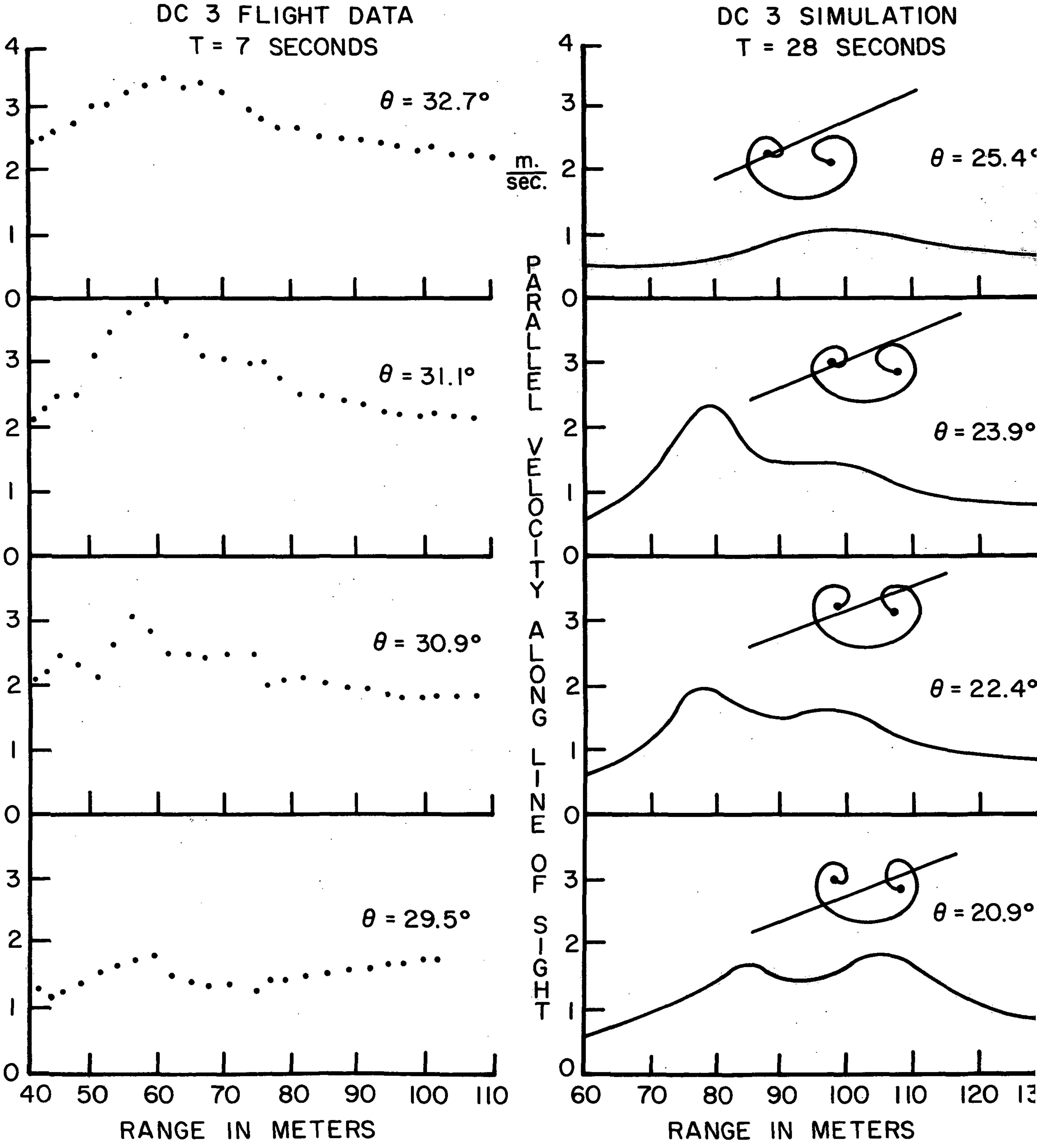

Figure 17, Comparison of DC-3 Fly-By Data and Simulation Results for $\overline{v}$.

The flight data shown in Fgiure 17 were obtained by NASA-MSFC and Lockheed-Huntsville personnel. No independent knowledge of the vortex location is available and the data shown were four successive elevation angles, the first one selected arbitrarily because of the clear signals shown. The signatures show several qualitative similarities to the simulation, although the average velocity is considerably higher. A more careful evaluation of the ambient wind profile and aircraft parameters will be required to obtain better comparison of the simulation with data.

V.3 B-720 Simulation

Figures 18 to 38 show simulations of the vortex wake of a B720. The altitude at time zero was taken to be 55.3 meters and the total circulation of one wing as 190 m^2/sec. A light wind was assumed according to $u_{wind} = 0.5 \ln (1+y/2)$ m/sec. Two LDV systems were assumed located on opposite sides of the aircraft track. Figures 19 and 20 show the overall geometry at an elapsed time of 18 seconds. In Figures 21 to 24 we show range-elevation plots of several variables; the actual local parallel velocity along the line of sight, the mean velocity averaged over the range resolution function, the rectified mean velocity as determined from the simulated spectra and the (square root of the) variance. In all cases to be discussed, the intensity and velocity thresholds were taken to be zero. In Figure 25 the peak velocity along each line of sight is plotted versus elevation angle.

Four particular lines of sight are identified in each plot and exhibit various characteristics of the signature. In general, both vortices can be identified (at least at this range) in all lines of sight which pass between the two vortices. The line of sight C passes near the midpoint and shows two comparable peaks. Lines of sight passing near the edge of a vortex core (but not through the core) show a strong peak (e.g., B); however when the line of sight passes directly through a vortex core (e.g., D and A), only

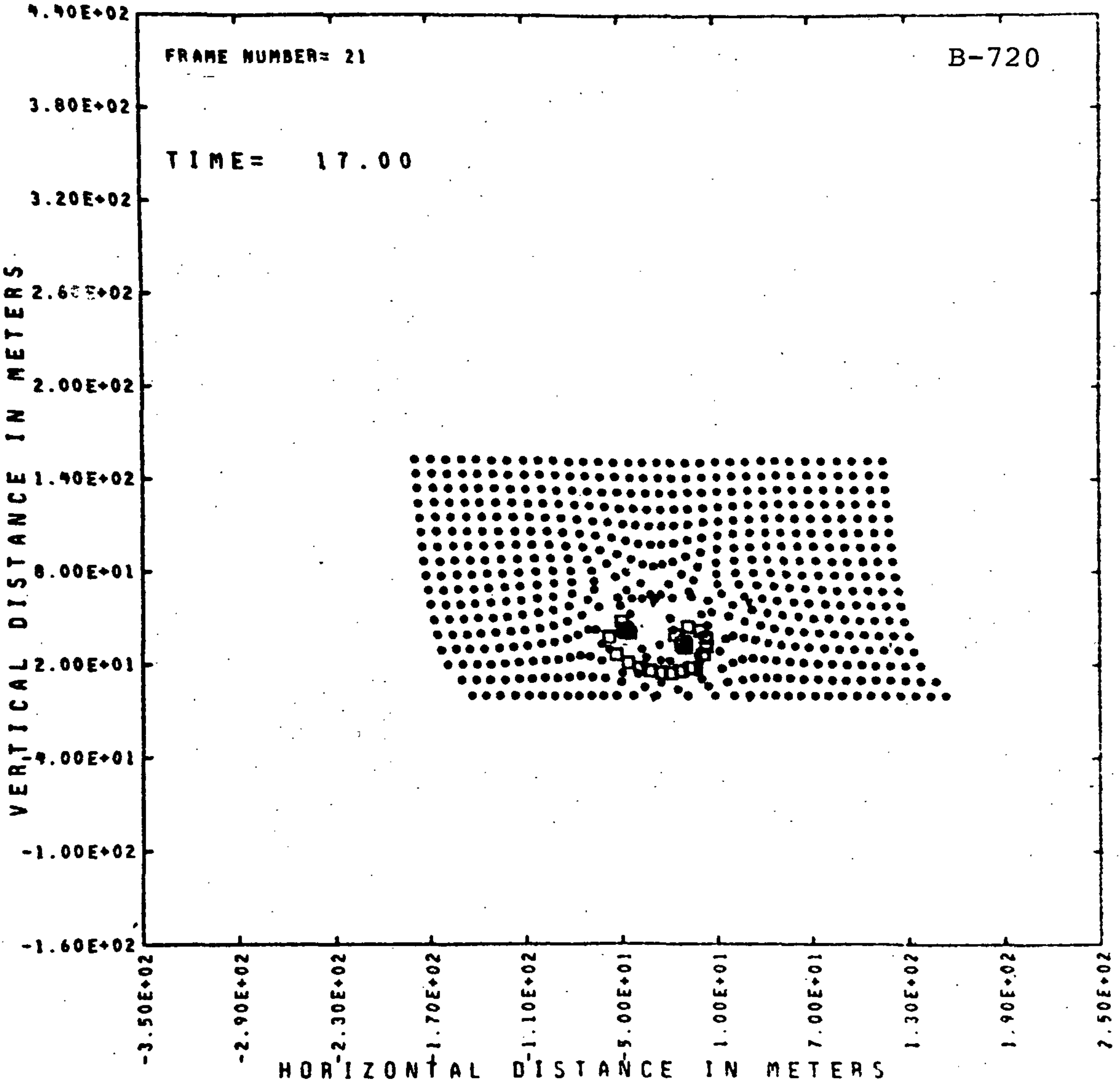

Figure 18. Trailing vortex configuration (B720) at 17 seconds.

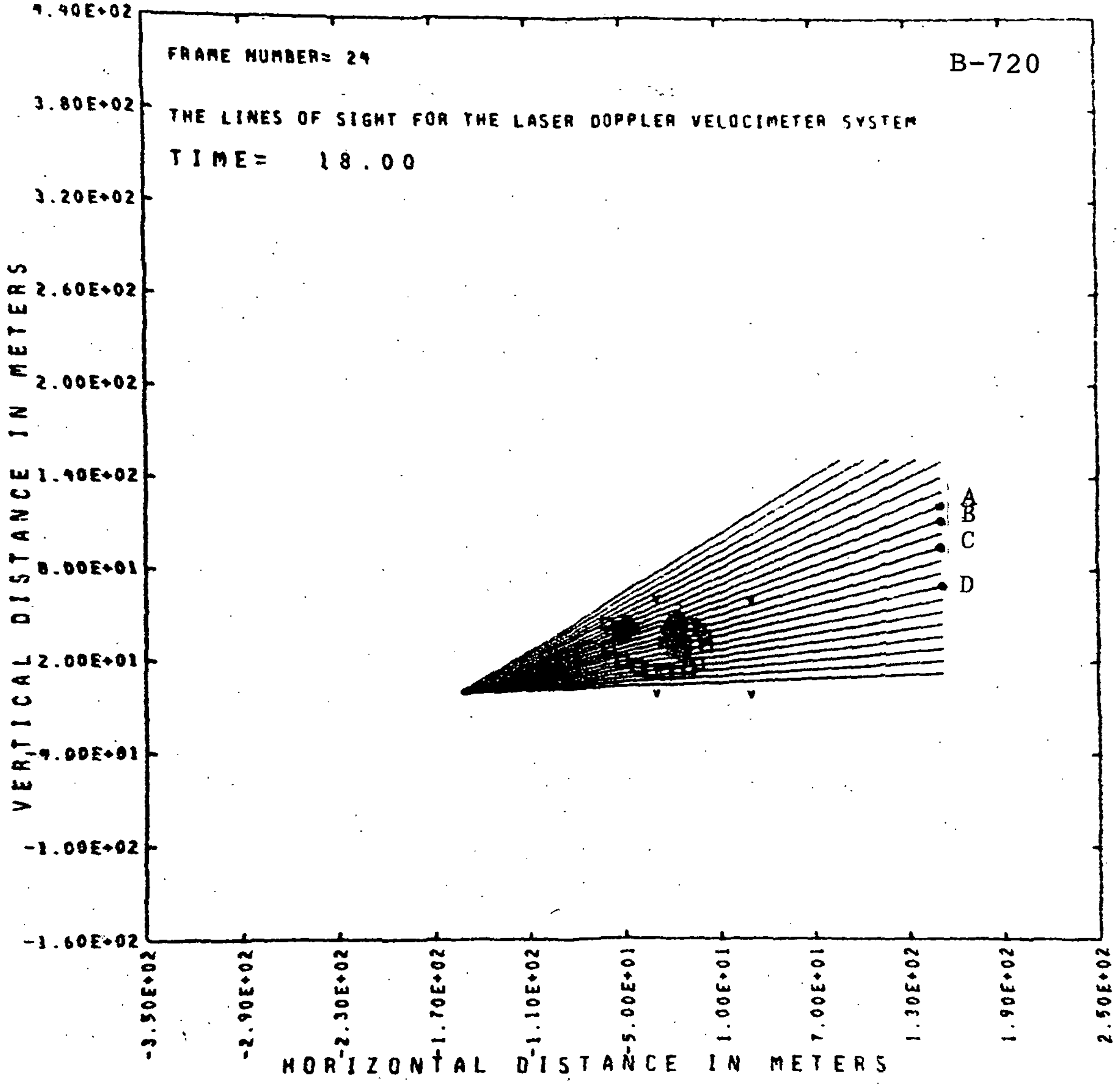

Figure 19. An LDV fan beam configuration at 18 seconds; downwind site

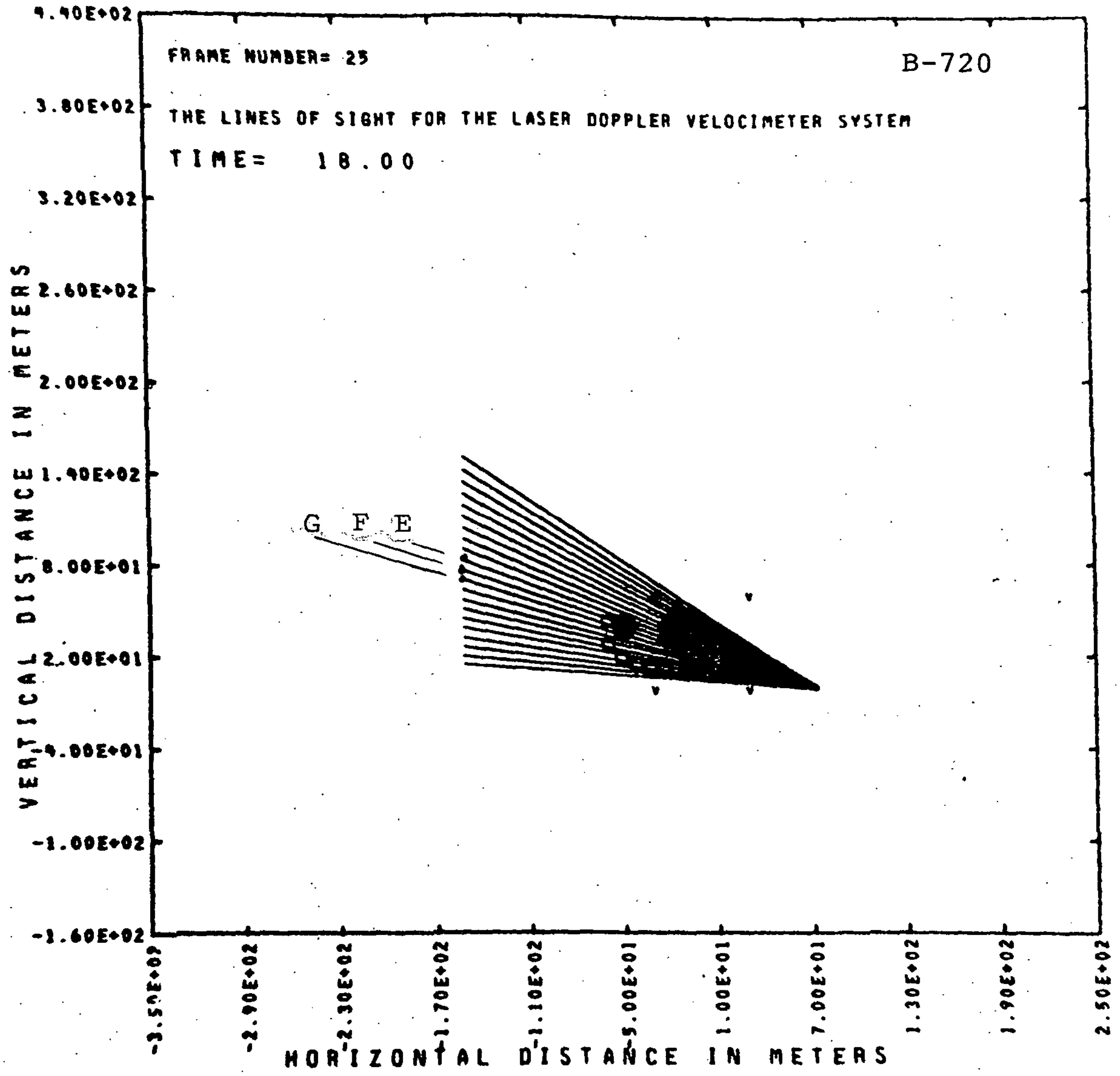

Figure 20. An LDV fan beam configuration at 18 seconds; upwind site

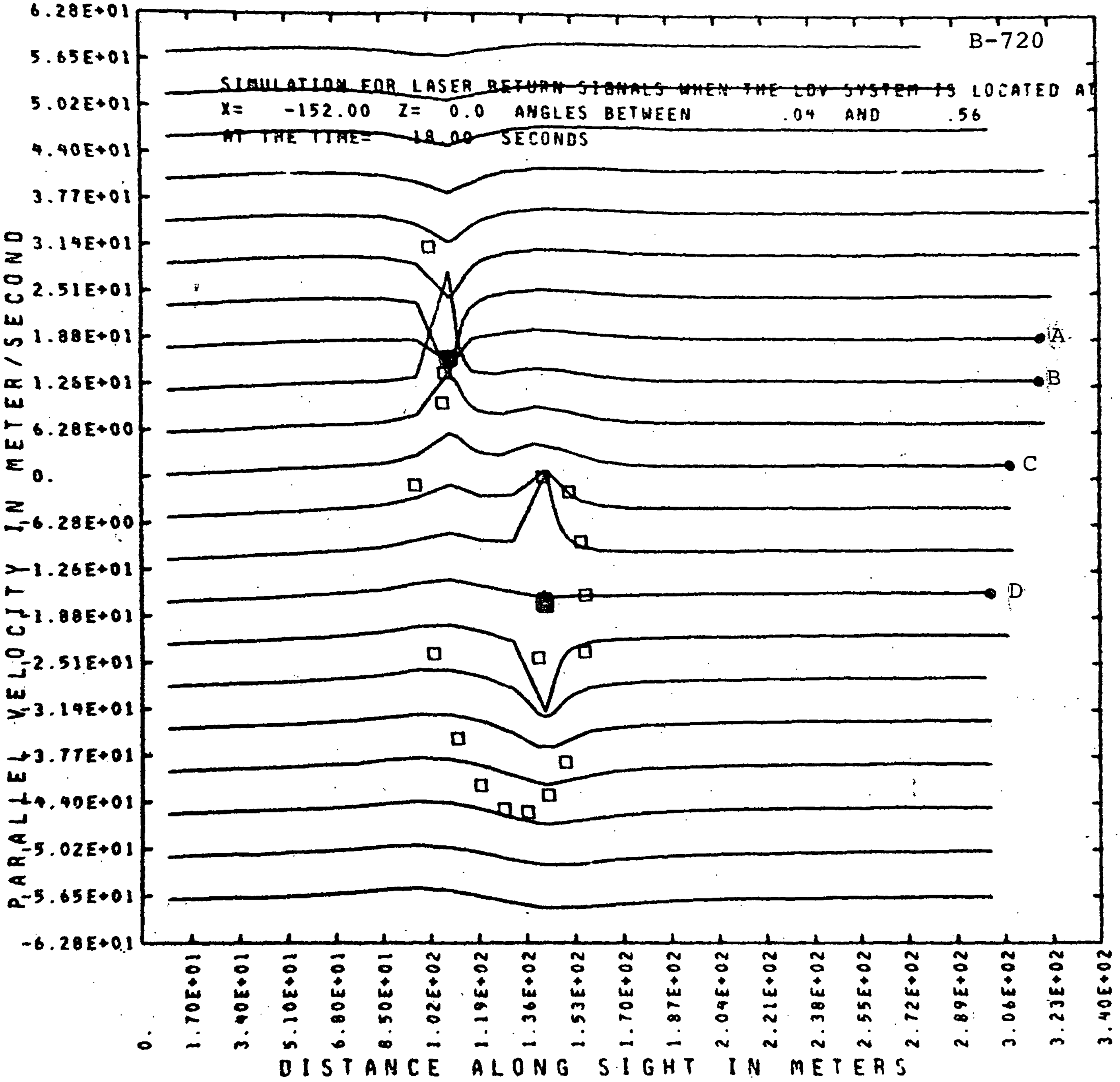

Figure 21. Parallel velocity along lines of sight (downwind site)

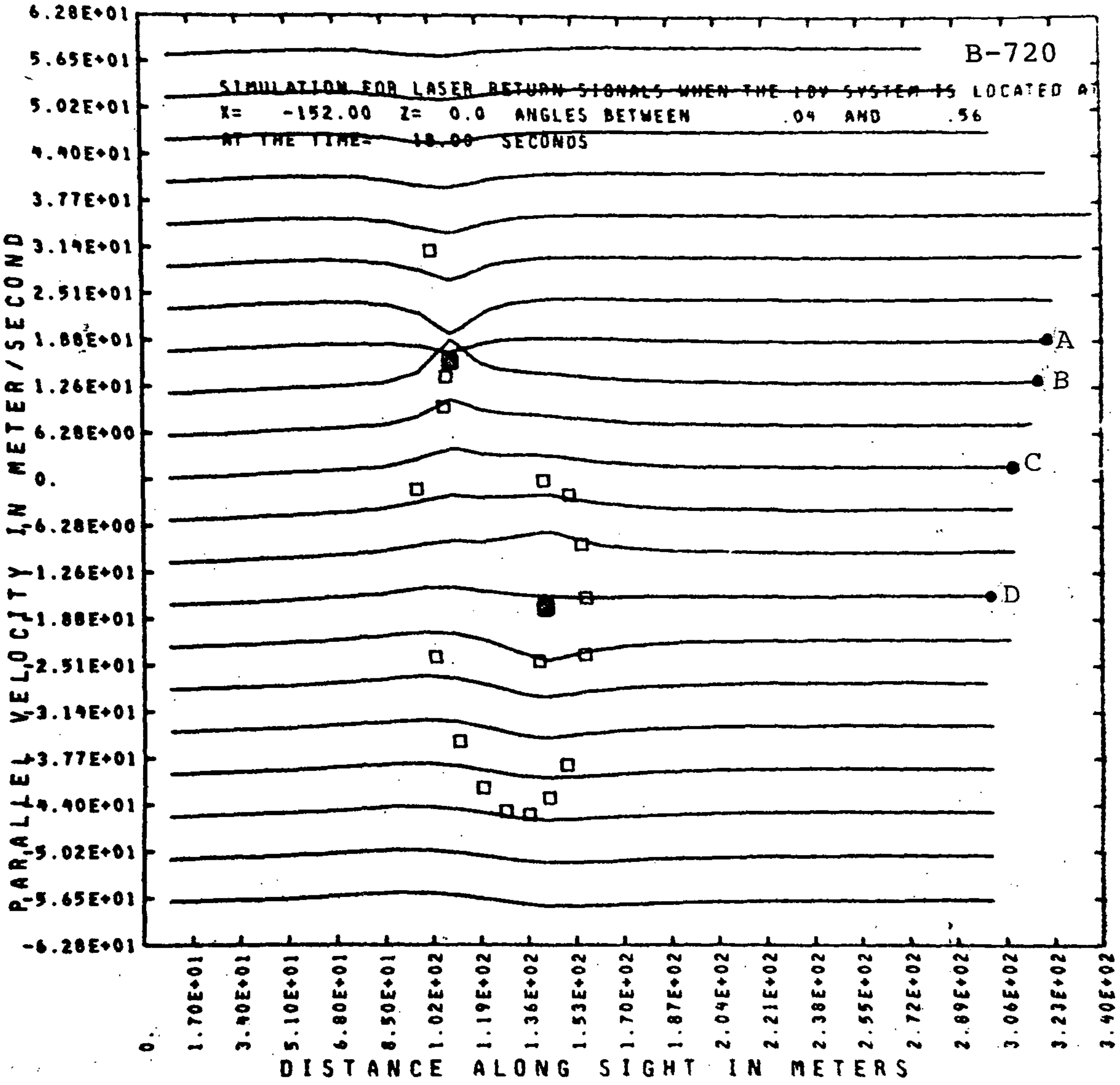

Figure 22. Mean parallel velocity with finite range resolution along lines of sight (downwind site)

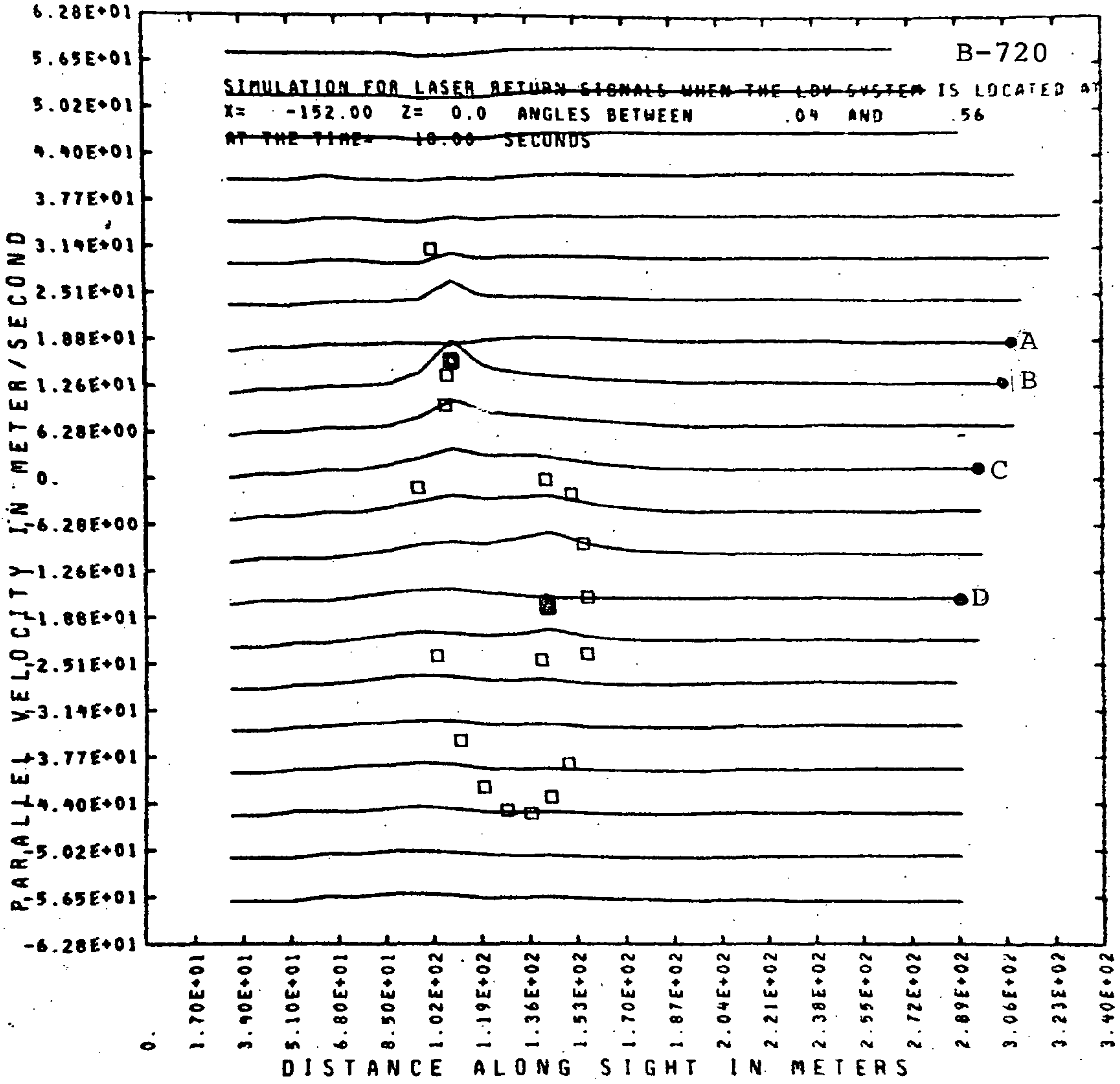

Figure 23. Mean parallel velocity from simulated spectra with rectification along lines of sight (downwind site)

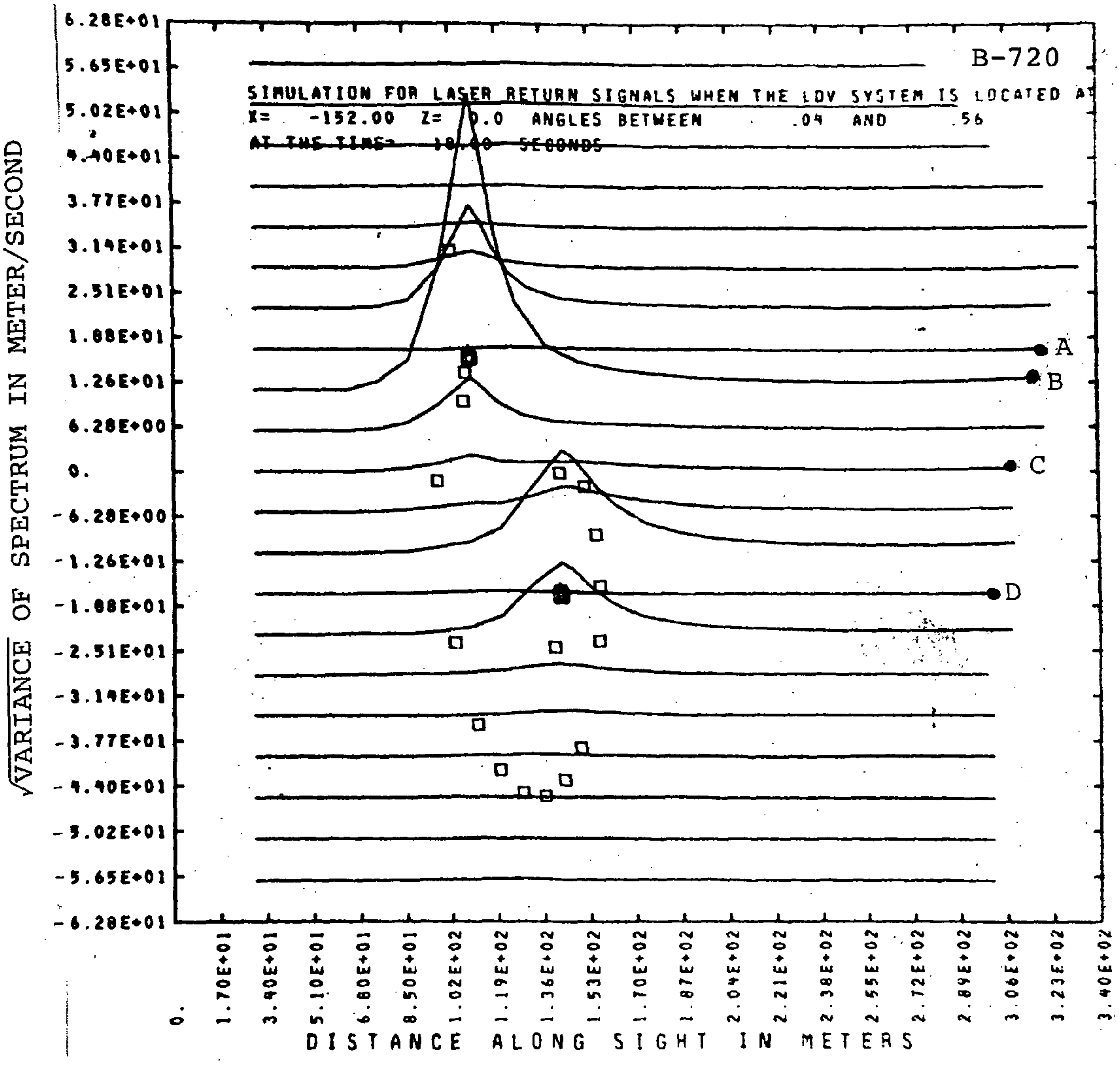

Figure 24. Square root of spectrum variance along lines of sight (downwind site)

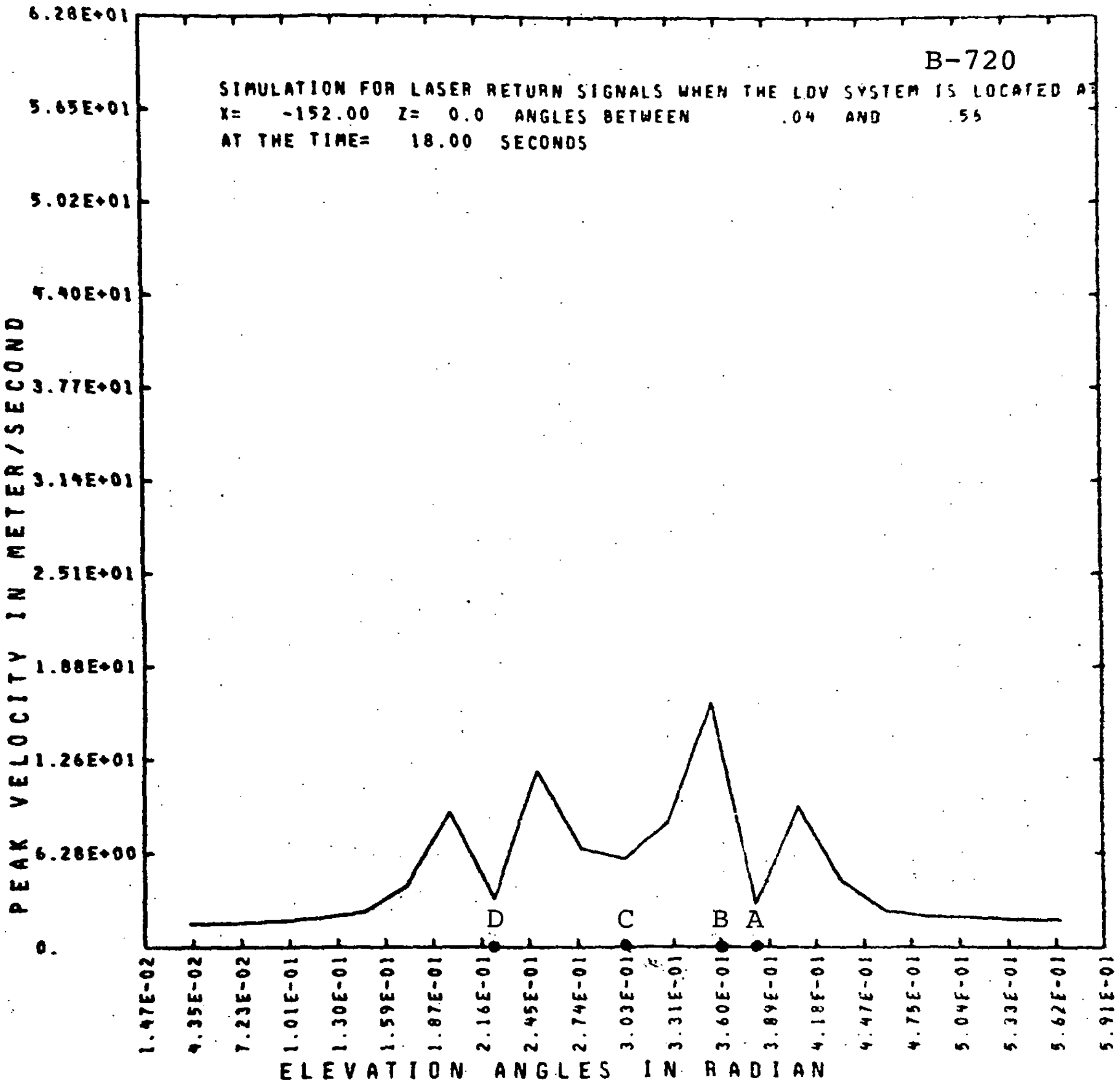

Figure 25. Peak velocity on each line of sight vs. elevation angle (downwind site)

the broad maxima from the other vortex is discernible. These features are particularly marked in the variance plots (Figure 24), where the core edges are quite visible, whereas the lines of sight passing through the center of the core show no signature.

When plotted versus elevation angle, the peak velocity identifies the core edges. However, the lateral spacing between the lines of sight (1.5°) at this range (~ 120 m) is considerably too large to define the structure of the core.

Simulated spectra for the four lines of sight (A,B,C,D) are displayed in Figures 26 to 29 as a function of range.

A similar set of data for the second LDV system is shown in Figures 30 to 37. The features here are basically similar except for the plot of V_{peak} versus elevation angle. Here only three peaks are identifiable rather than the four in Figure 25 which were identified with the core edges.

In Figure 38 we display both V_{peak} plots together with the lines of sight. It is clear from this view that, for the second system, the top edge of the far vortex appears directly behind the lower edge of the near vortex.

When this simulation was carried out, the skewness and kurtosis calculations had not been incorporated into the computation. The results of a more recent simulation under similar but not identical conditions, are shown in Figures 39

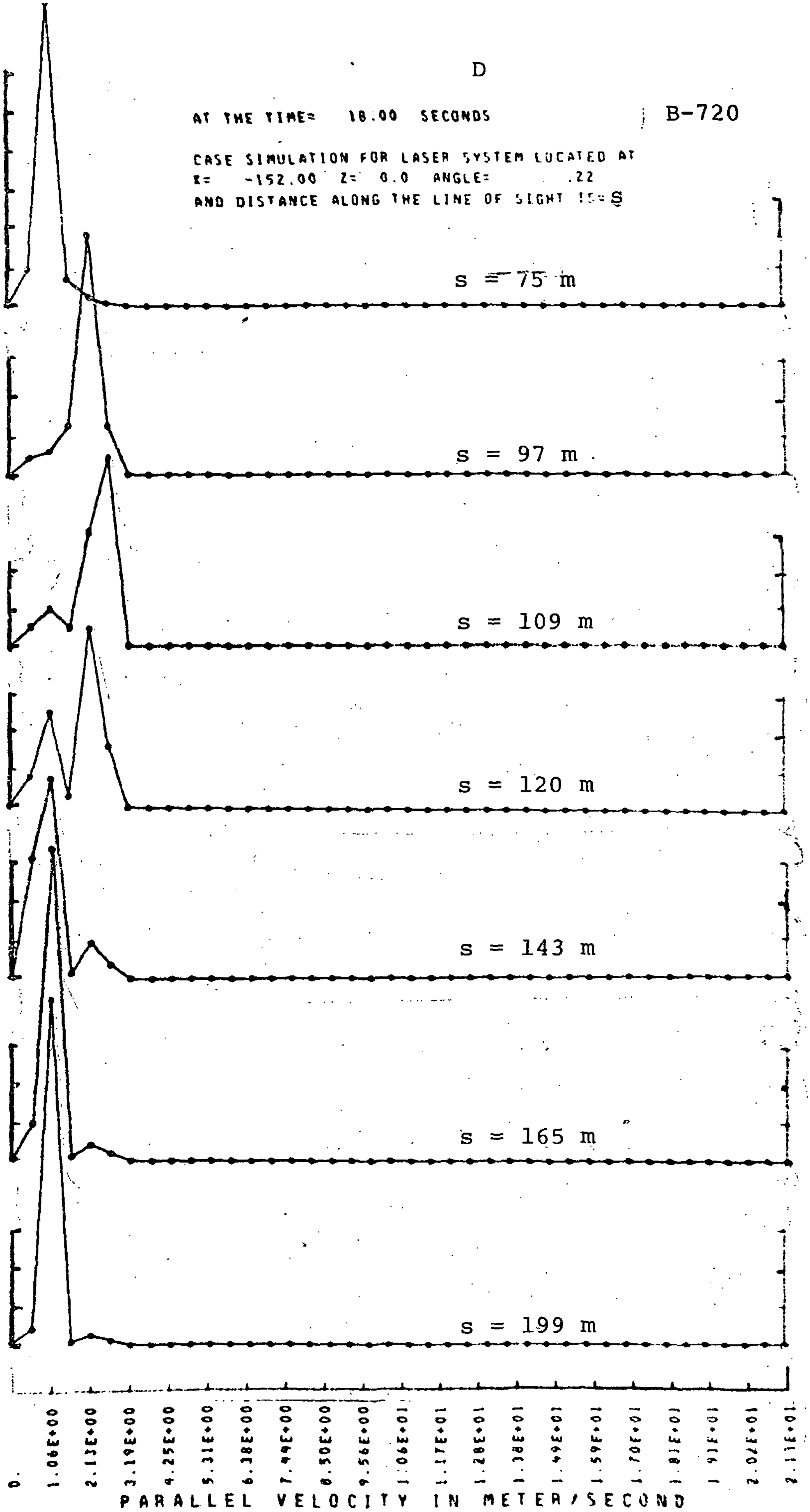

Figure 26. Simulated spectra for line of sight D (downwind site)

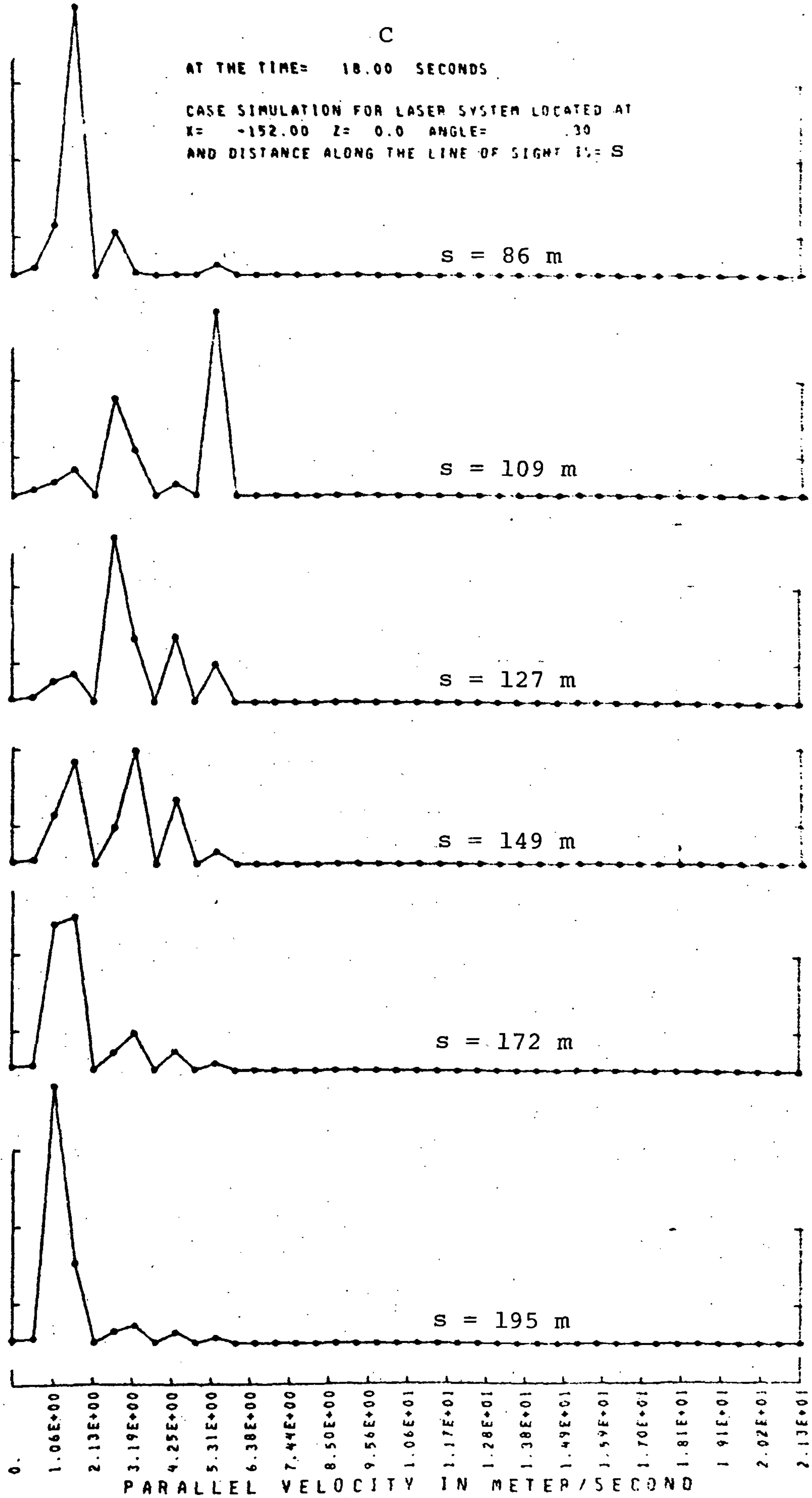

Figure 27. Simulated spectra for line of sight C (downwind site)

B

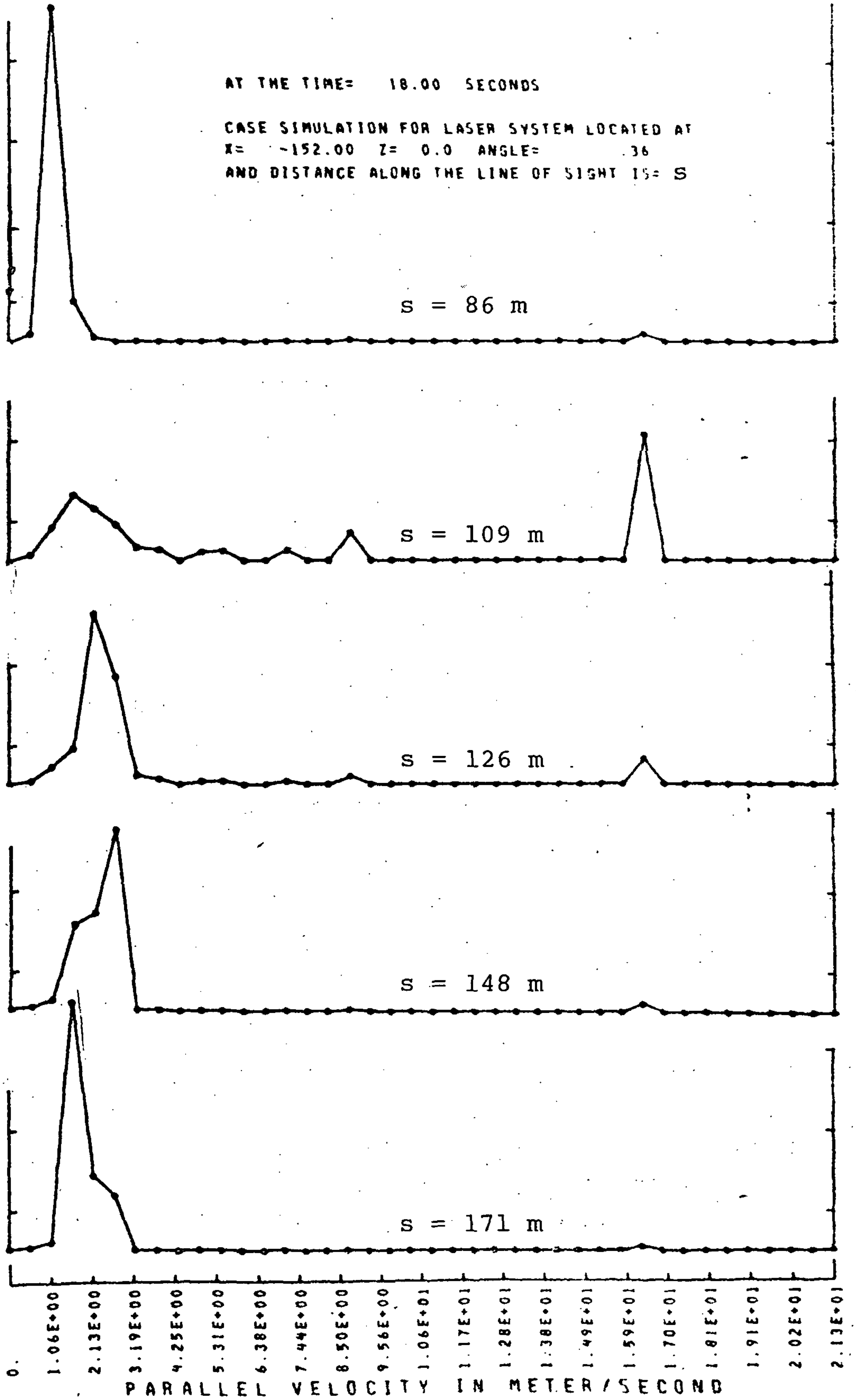

Figure 28. Simulated spectra for line of sight B (downwind site)

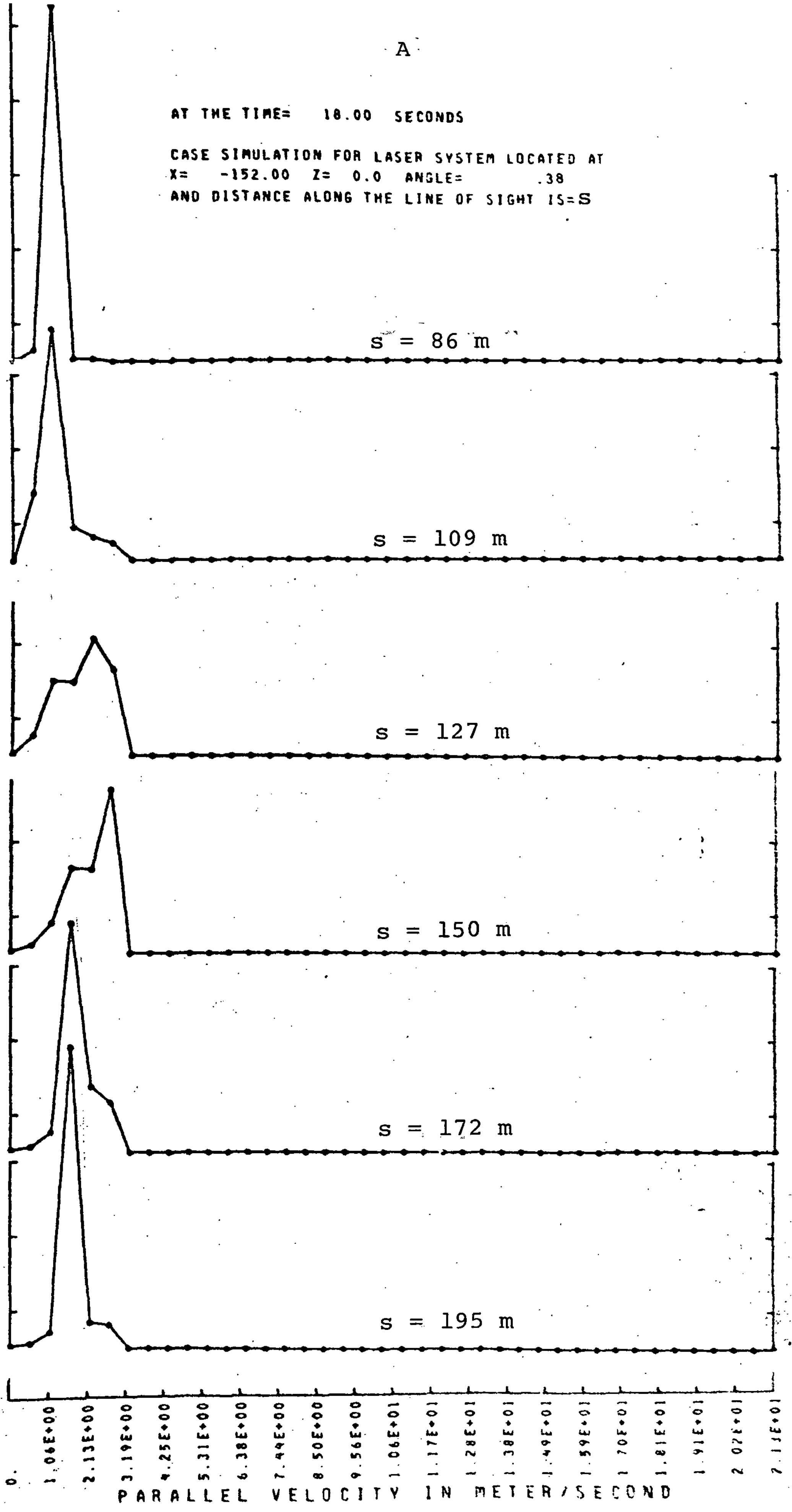

Figure 29. Simulated spectra for line of sight A (downwind site).

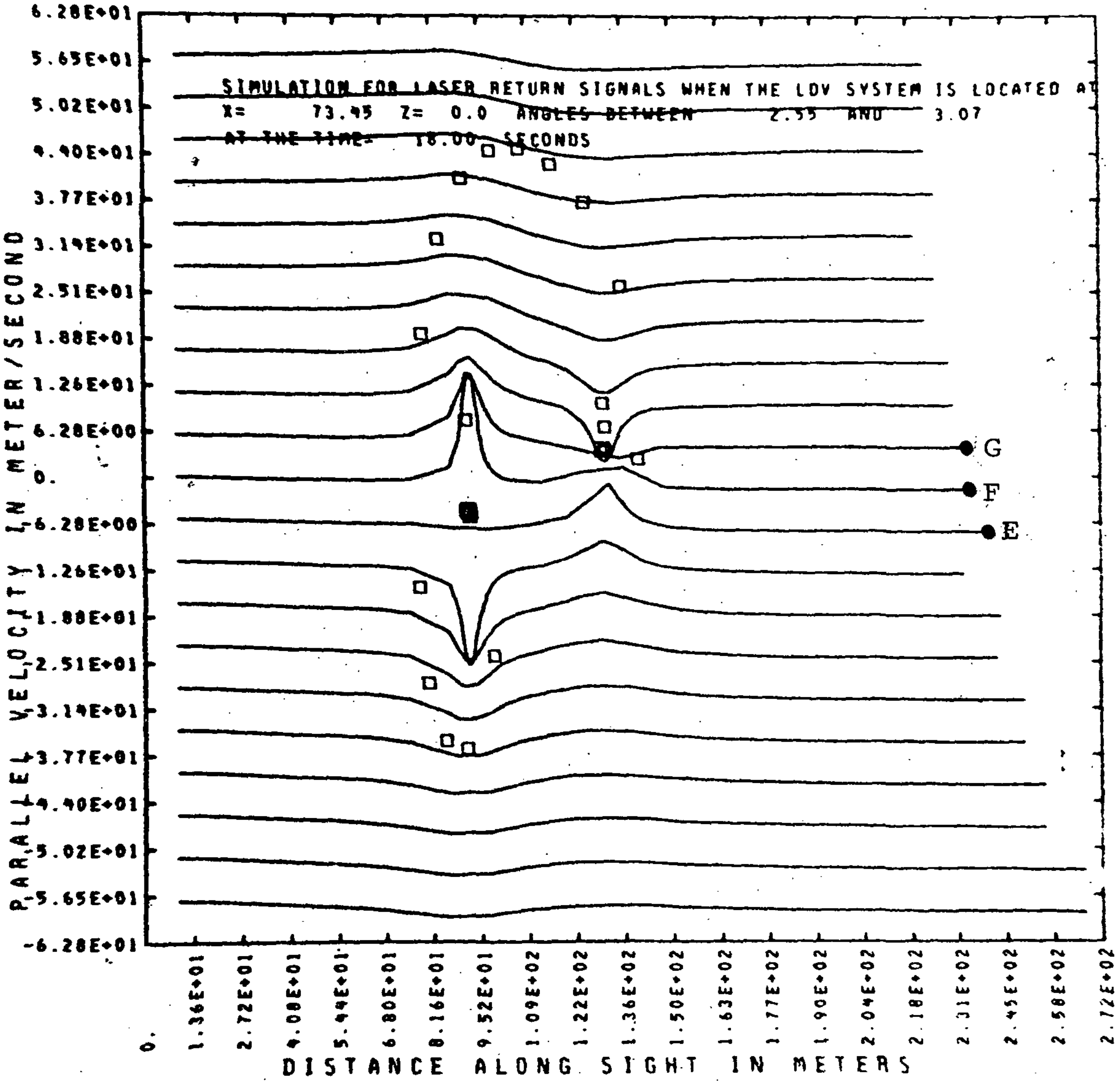

Figure 30. Parallel velocity along lines of sight (downwind site)

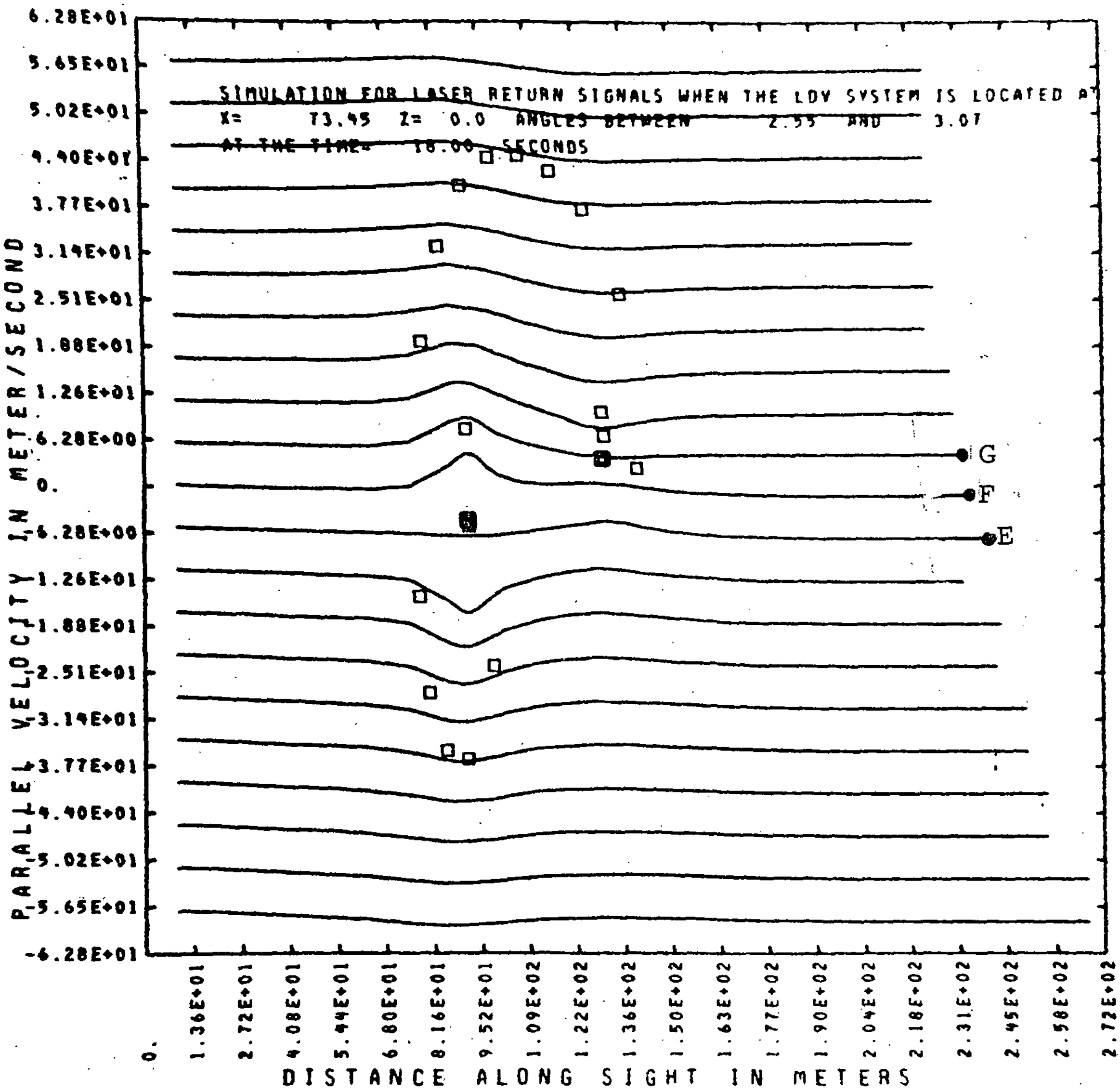

Figure 31. Mean parallel velocity with finite range resolution along lines of sight (upwind site)

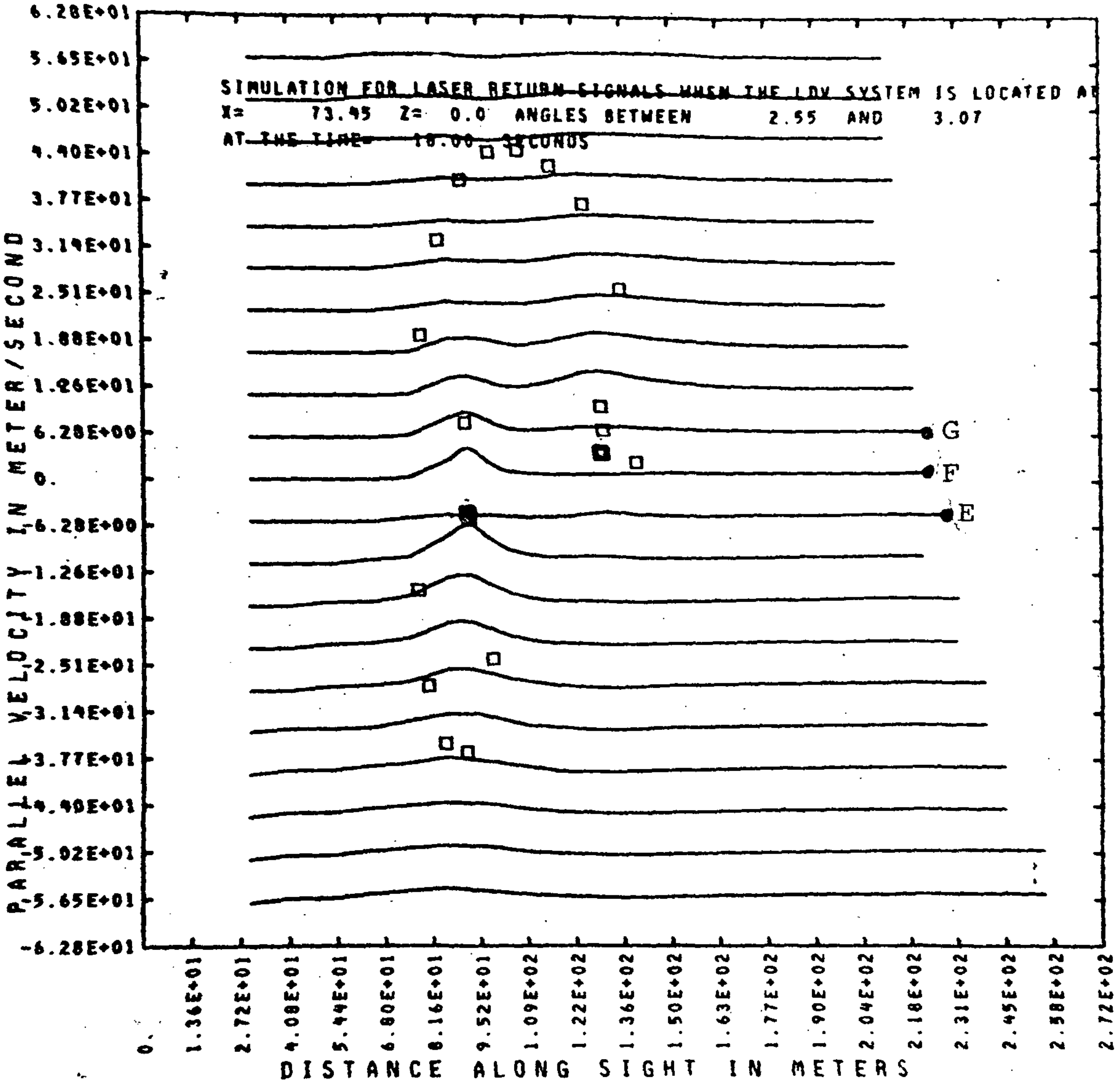

FIGURE 32. Mean parallel velocity from simulated spectra with rectification along lines of sight (upwind site)

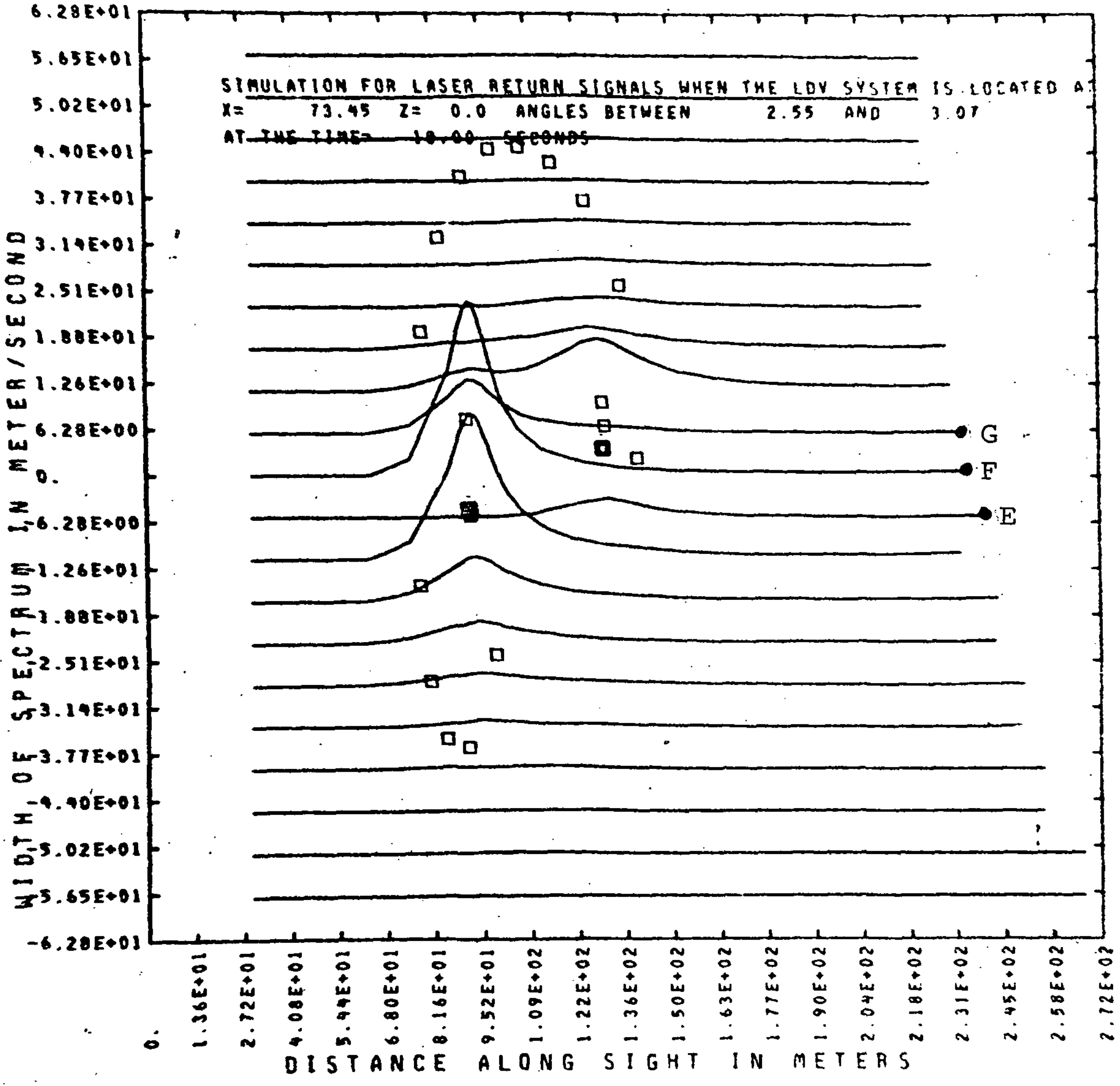

Figure 33. Square root of spectrum variance along lines of sight (upwind site)

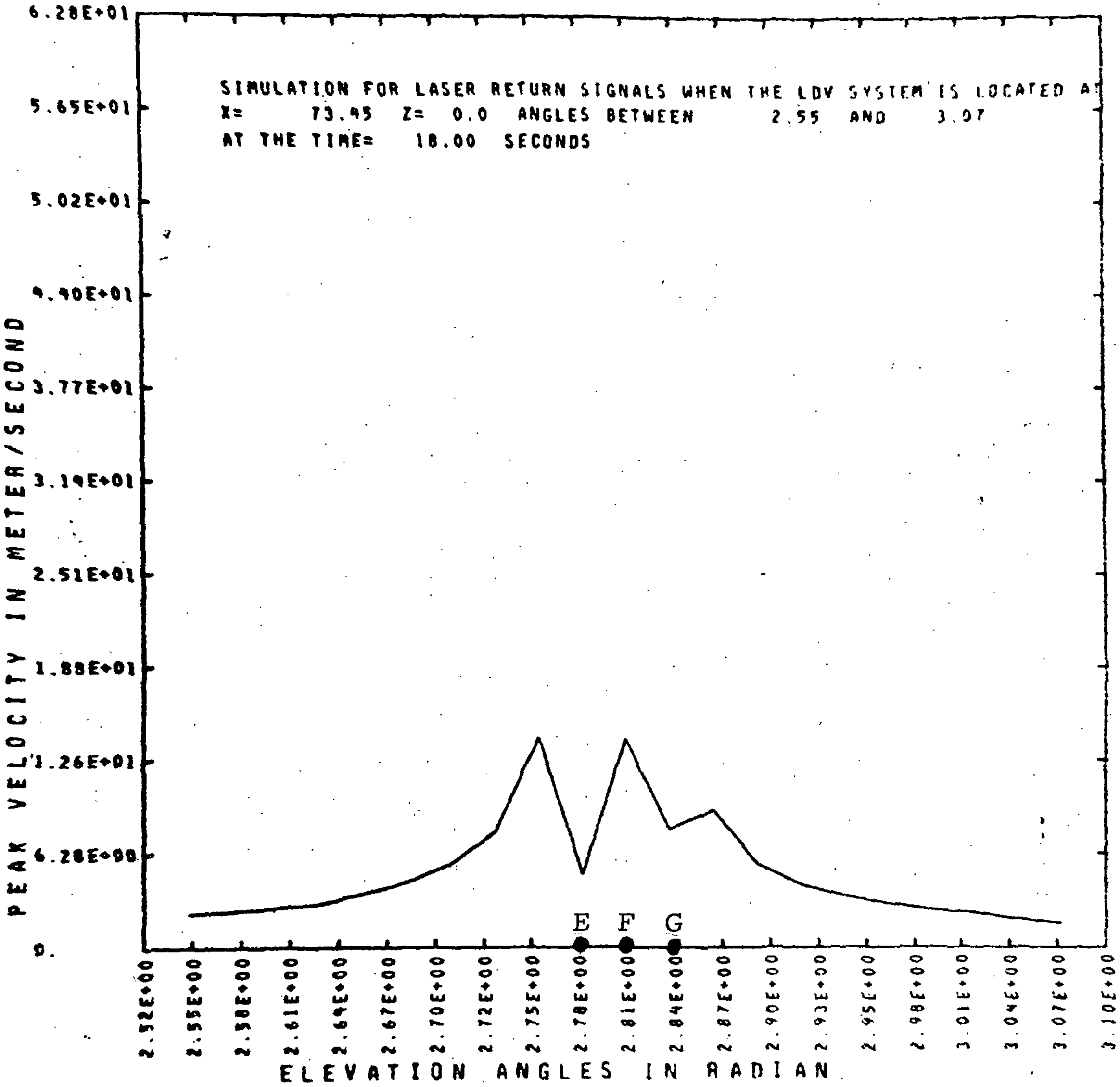

Figure 34. Peak velocity on each line of sight vs. elevation angle (upwind site)

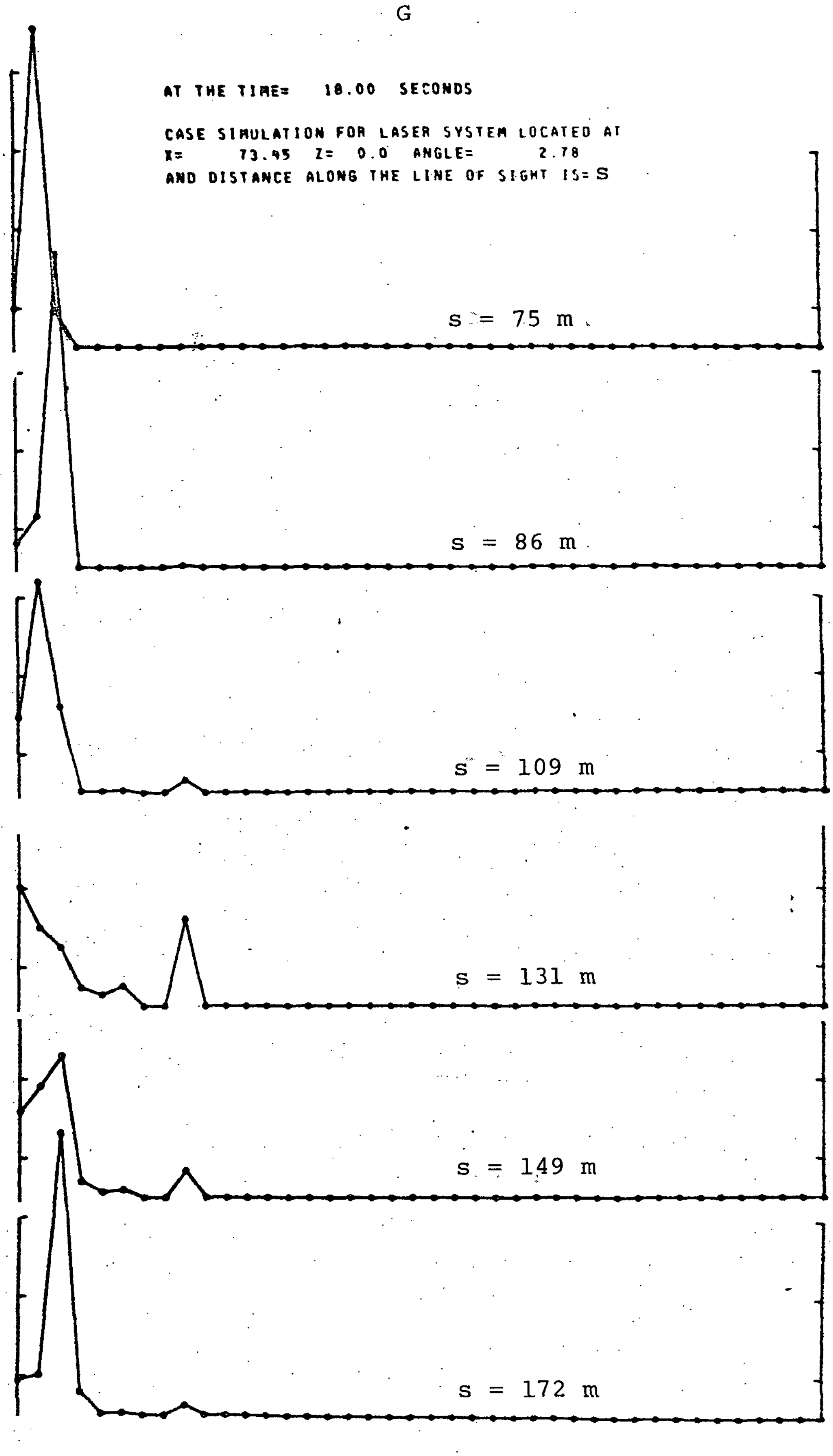

Figure 35. Simulated spectra for line of sight G (upwind site)

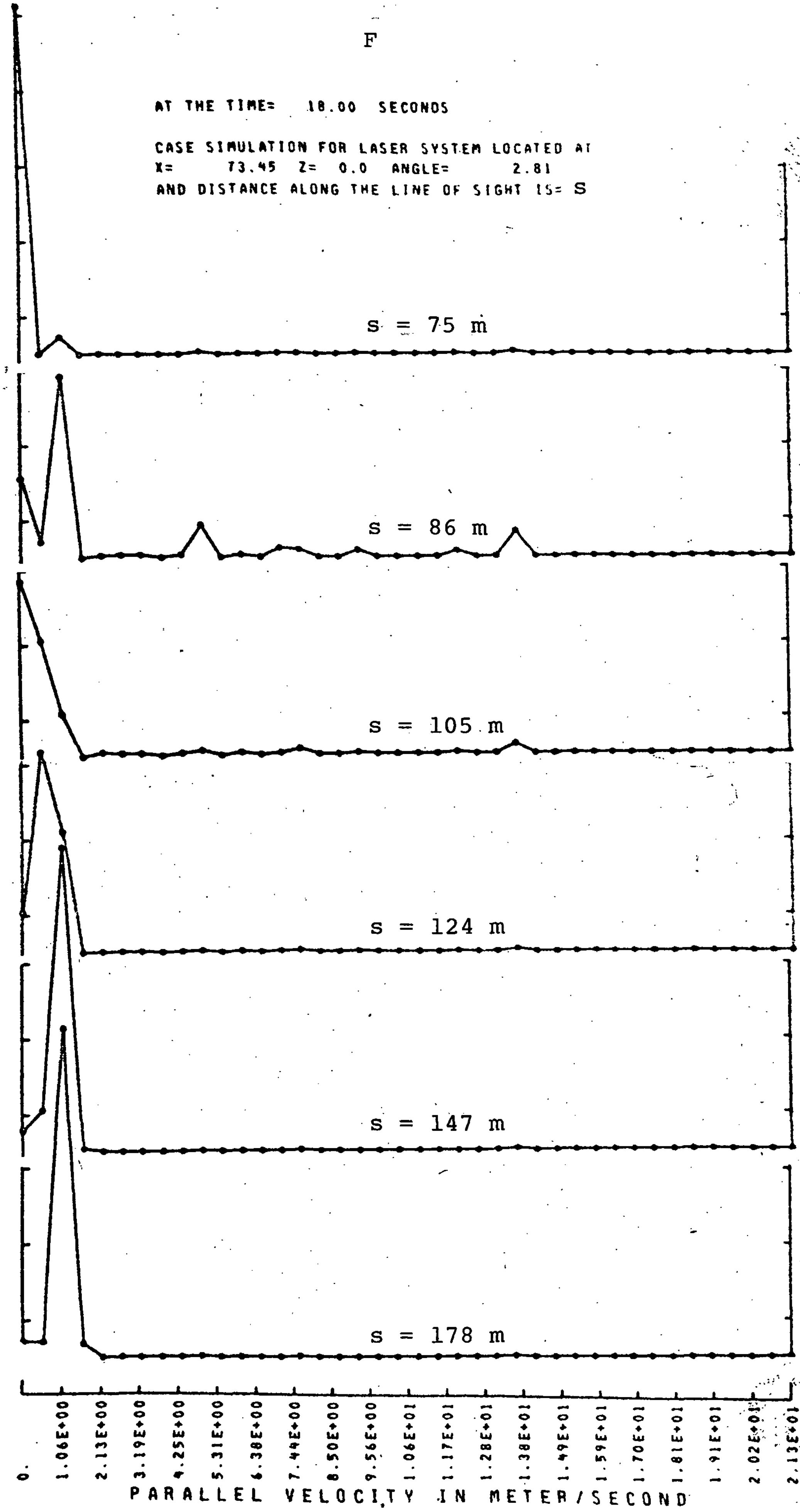

Figure 36. Simulated spectra for line of sight F (upwind site)

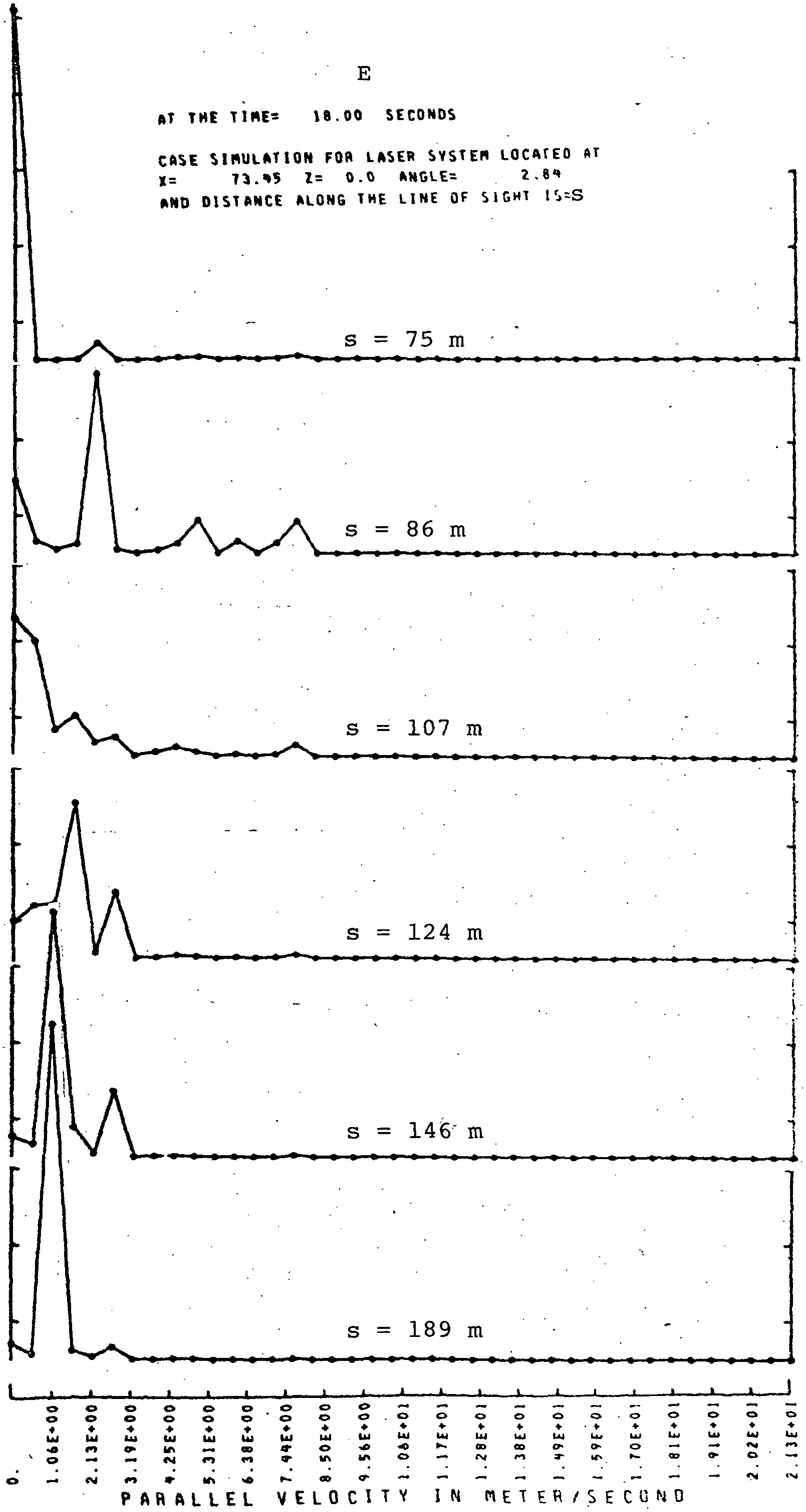

Figure 37. Simulated spectra for line of sight E (upwind site)

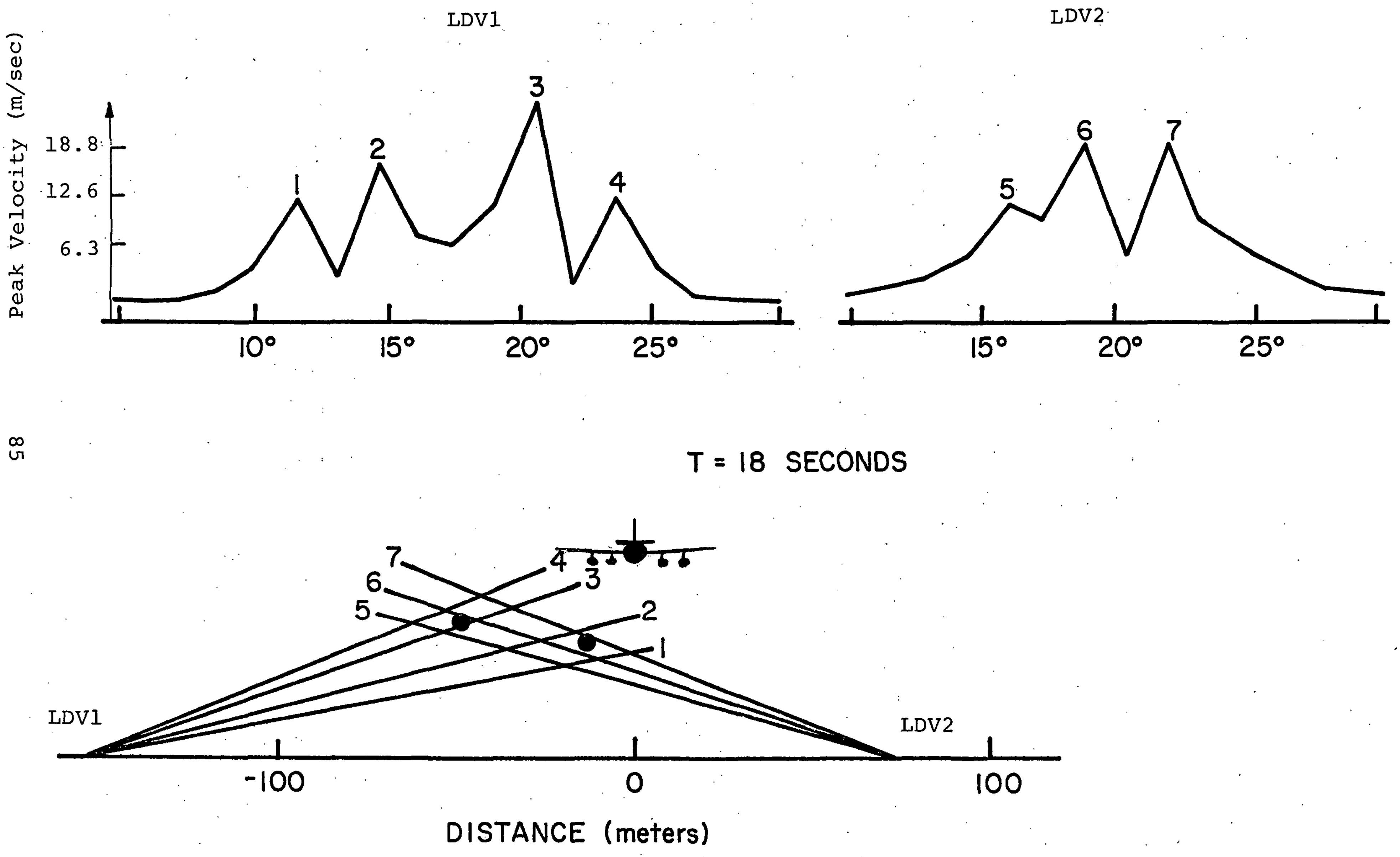

Figure 38. Peak velocities as a function of elevation angle.

to 42. Here it can be seen that both the skewness and kurtosis exhibit a similar range sensitivity as the variance, but are substantially more selective in angle. This presumably reflects their greater relative sensitivity to the higher velocities.

Cursory examination of these simulations indicate that the high moments (variance and, especially, skewness, kurtosis) provide a high selectivity for the edges of the vortex cores (but not the cores themselves). No conclusions concerning the effects of thresholds can be drawn from these results except to note that a high order moment such as kurtosis highly favors large spreads in velocity, and therefore, with the fairly coarse range resolution of the system, favors the high velocities. In this sense we would expect the kurtosis to bear some similarity to the lower order moments taken with a fairly high velocity threshold.

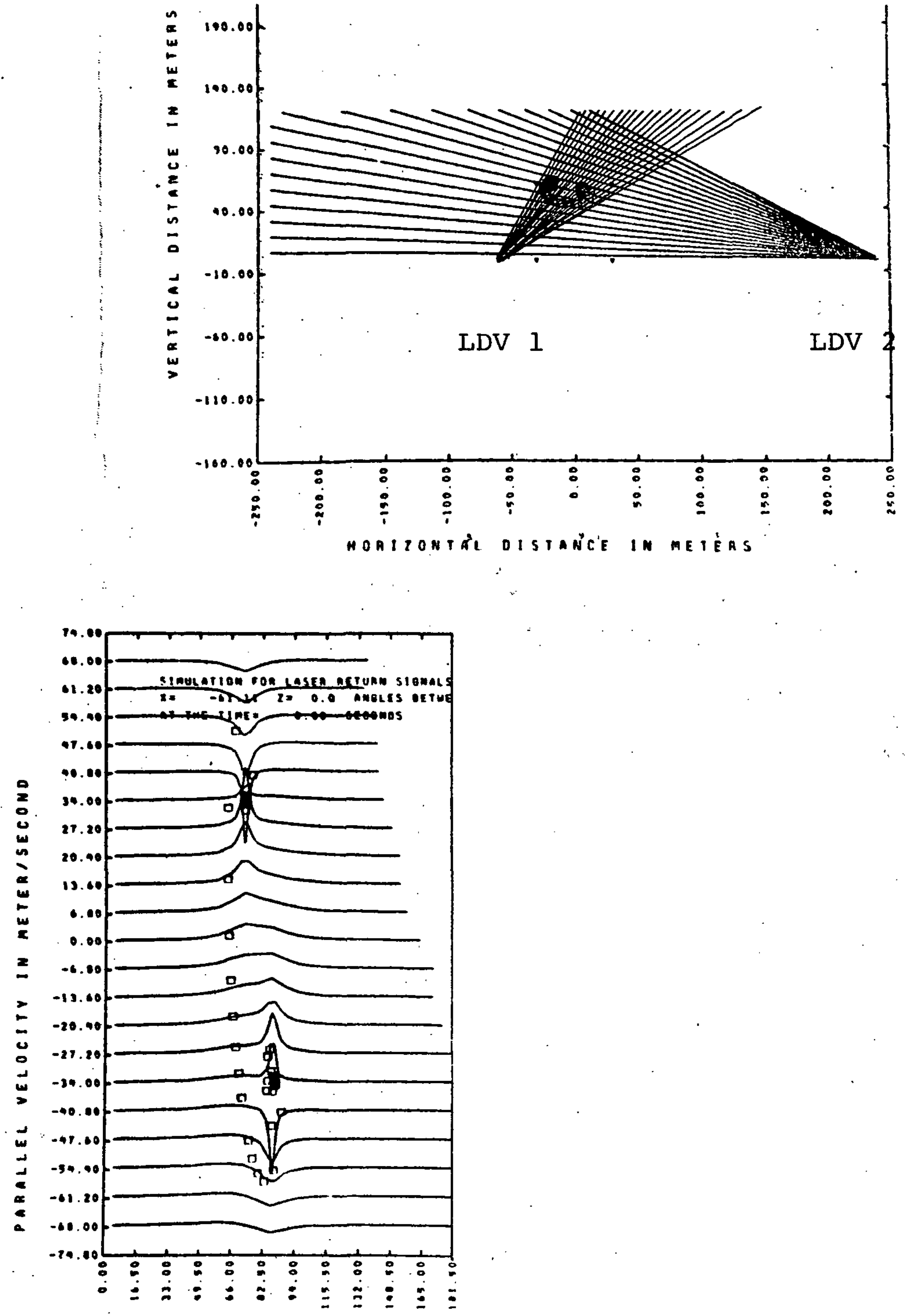

Range from LDV 1(mean range to wake: 80 meters)

Range from LDV 2(mean range to wake: 250 meters)

Figure 39. Local Parallel Velocity along various lines of sight for two LDV systems located at close and far ranges(B-720 simulations at 8 seconds)

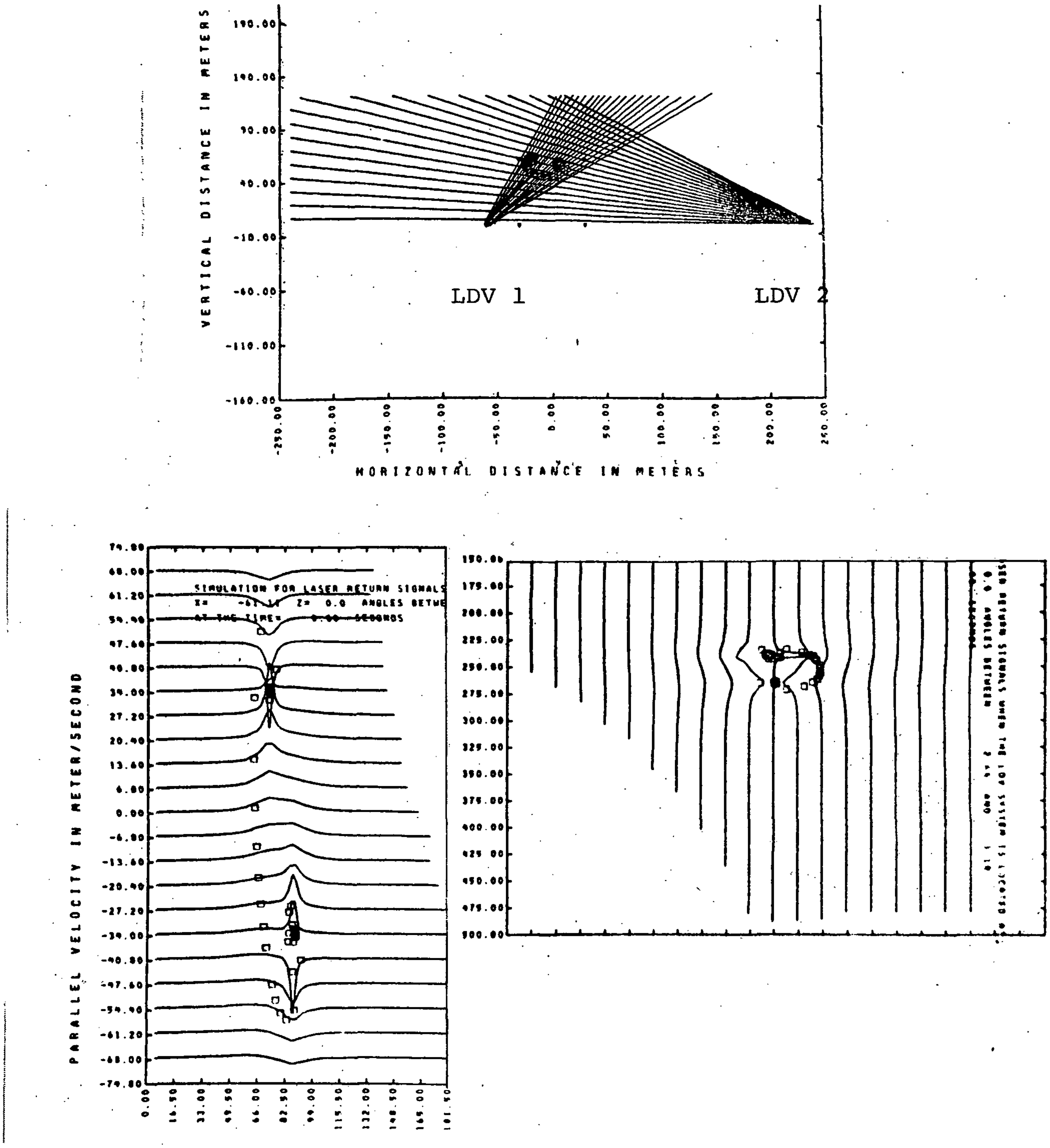

Range from LDV 1(mean range to wake: 80 meters)

Range from LDV 2(mean range to wake: 250 meters)

Figure 39. Local Parallel Velocity along various lines of sight for two LDV systems located at close and far ranges(B-720 simulations at 8 seconds)

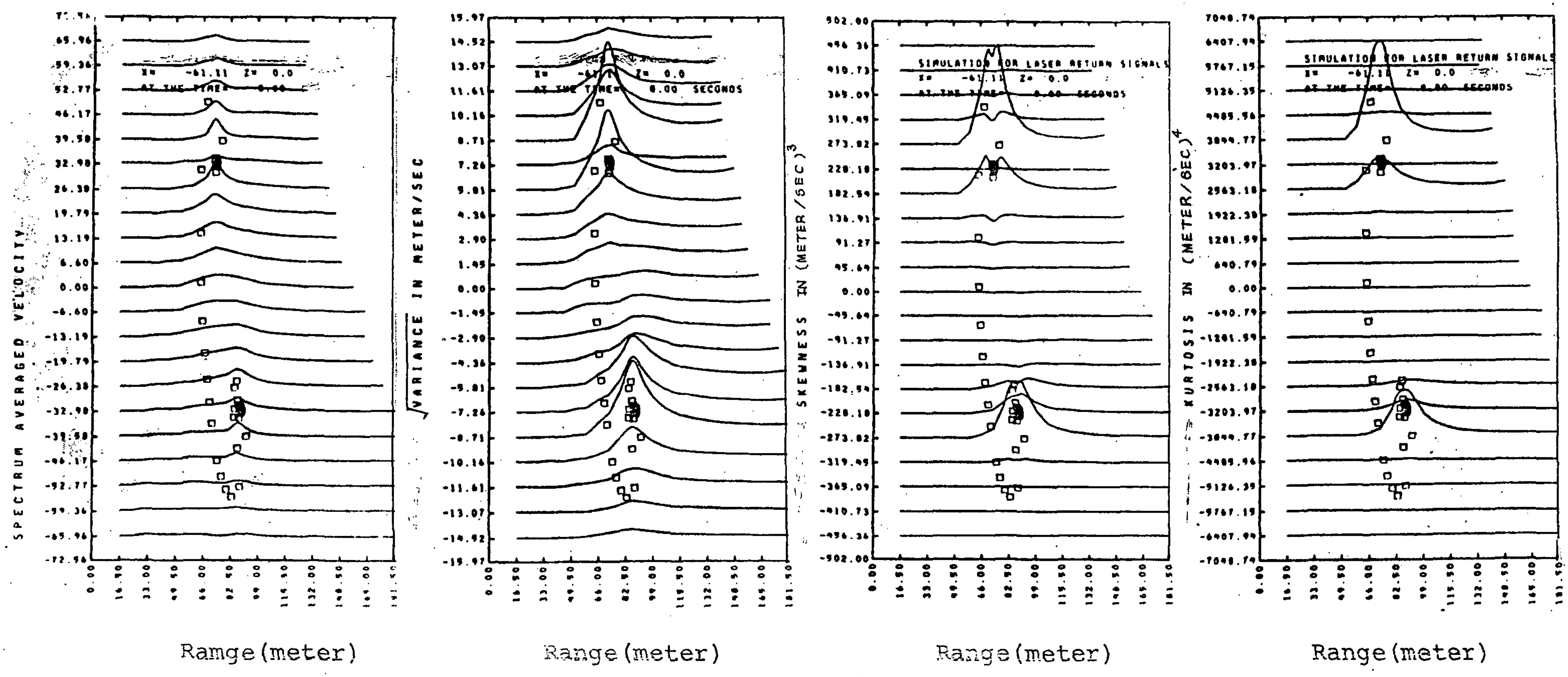

Figure 40. Various Spectral Moments simulated for the short range sensor LDV 1

(B-720 Simulation at 8 Seconds)

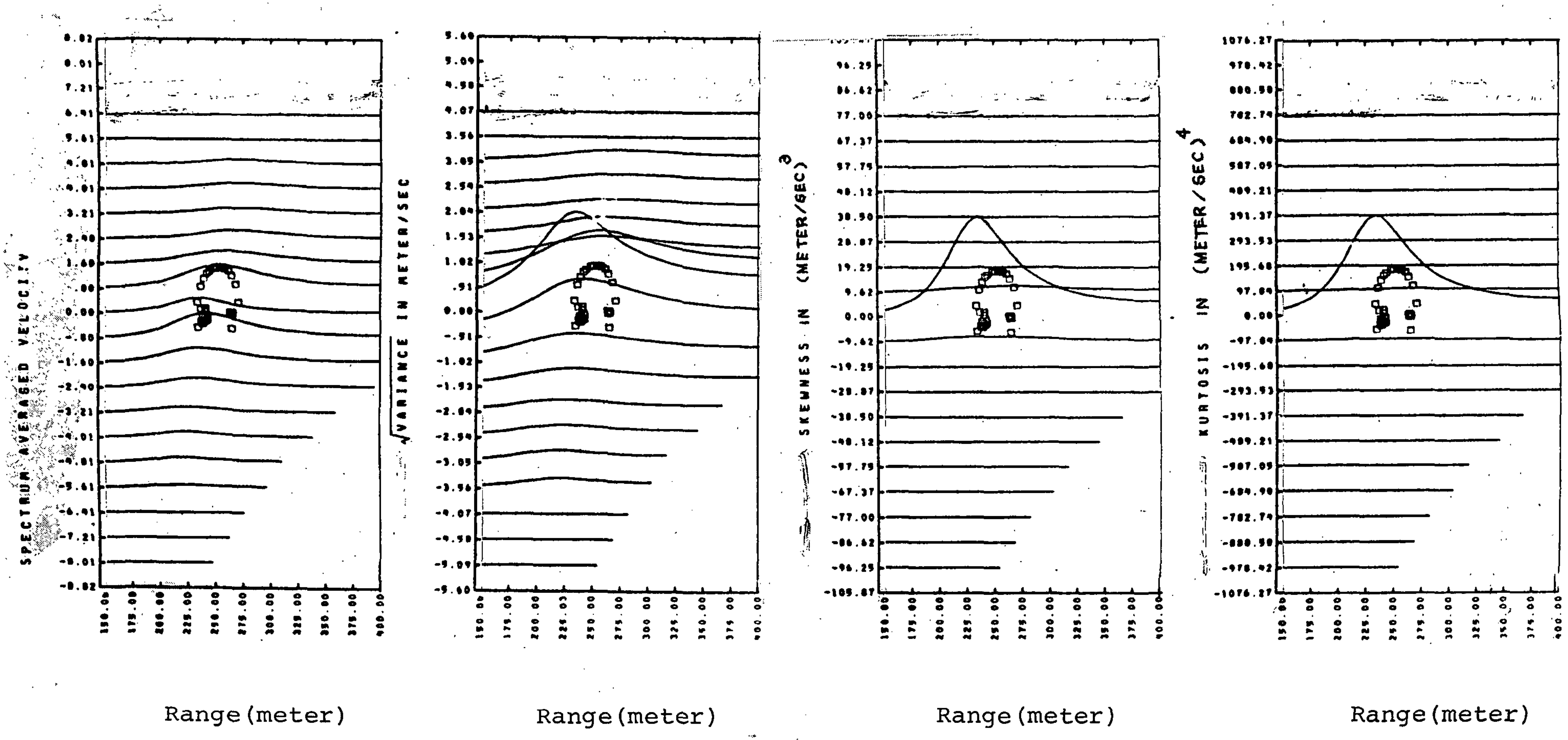

Figure 41. Various Spectral Moments simulated for the long range sensor LDV 2

(B720 Simulation at 8 seconds)

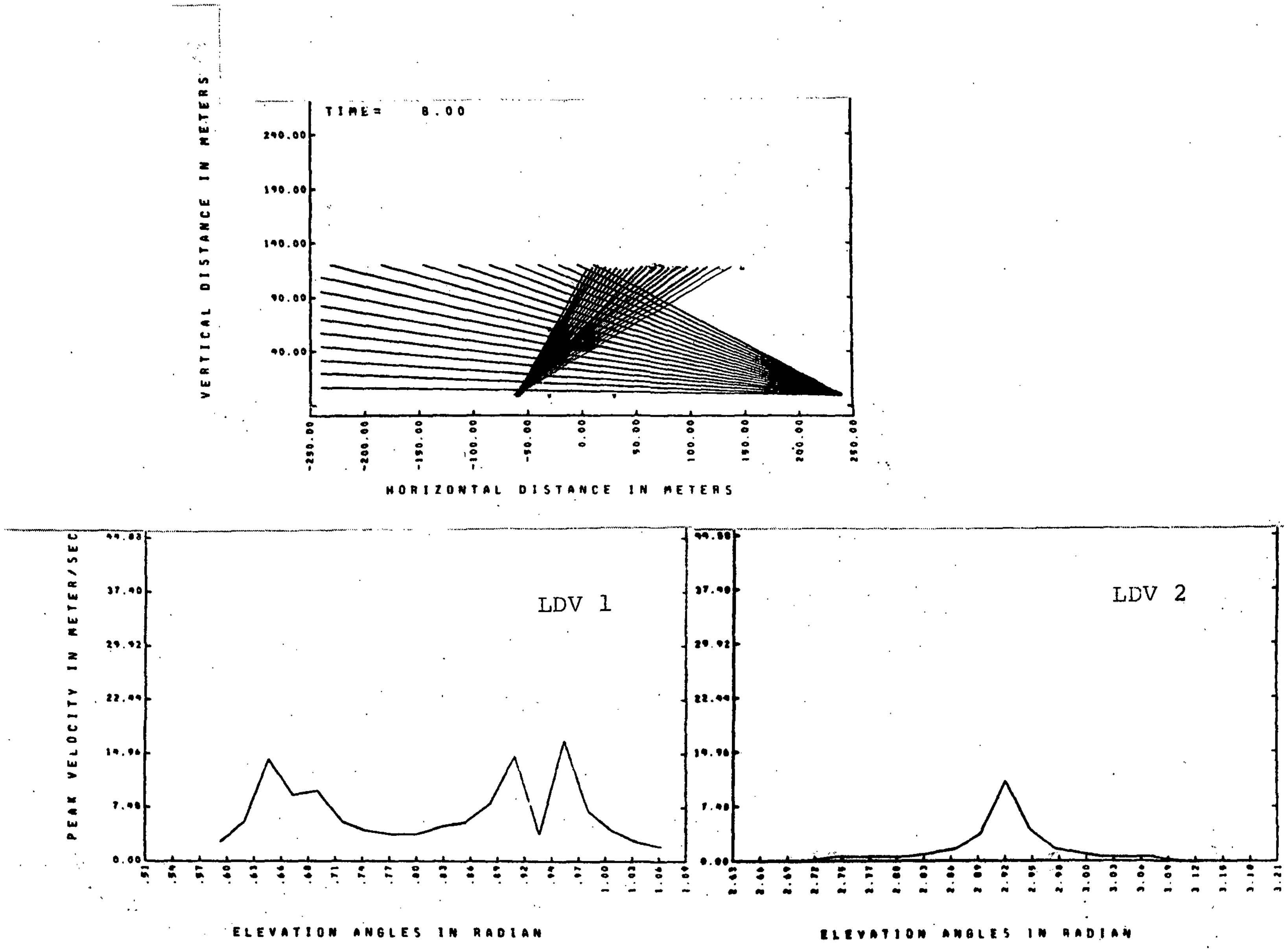

Figure 42. Peak Velocity versus angle(B-720 simulation at t=8 seconds)

VI.0 CONCLUSIONS

Two vortex detection modes may be considered: a local "hard target" mode in which a direct signal is obtained from the vortex centers and a "soft target" mode in which a portion of the flow field pattern is detected and the location of the vortices deduced by some sort of pattern recognition procedure. The former has the advantage of being simple and unambiguous, but may be subject to missed targets and/or false alarms. The latter requires a theoretical model for implementation and may be less able to provide precise position information. However, in general it tends to be less subject to misses or false alarms.

In order to be able to evaluate optimal detection modes we have attempted first to generate a simulation of the vortex-atmosphere hydrodynamics together with a simulation of the response of the laser doppler sensor system.

Several conclusions may be drawn from examination of the simulation data and comparison with the flight data:

1) The vortex wake appears as a spatially-distributed target, particularly for the low order moments. The vortex center itself provides a null signal to the LDV sensor and accurate location depends on locating the core edges or establishing the origin of the spatial pattern.

2) The range resolution varies strongly with range and the individual vortices are seen separately in the simulation at short range (ranges less than 120 to 150 meters) but at long range (greater than 200 meters) both vortices are merged.

3) At the longer ranges, high order moments give the best range and angle location. The kurtosis appears to yield the best localization of the technique considered.

4) The angular spacing used in the present model (1.5°) is inadequate to resolve the vortex at long range and should be reduced.

5) The measured data exhibit an extensive spatial distributions for most moments. The skewness and kurtosis are the most localized. Detailed interpretation of these patterns in terms of the vortex structure has not yet been made and requires careful comparison with the simulation.

6) The measured data exhibit spatial irregularities or noise, whose source has not been identified. Candidates include turbulence, aerosol density variations, and propagation degradations.

REFERENCES

Betz, A., "Behavior of Vortex Systems", NASA TM 713, 1933.

Blackdar, A.K. and H. Tennekes, "Asymptotic Similarity in Neutral Barotropic Planetary Boundary Layers", Journal of the Atmospheric Sciences, Vol. 25, pp. 1015, 1968.

Brashears, M.R. and J.N. Hallock, "Aircraft Wake Vortex Transport Model", AIAA Paper No. 73-679, AIAA 6th Fluid and Plasma Dynamics Conference, Palm Springs, California, July 16-18, 1973.

Batchelor, G.K., An Introduction to Fluid Dynamics, Cambridge University Press (1967).

Burnham, D., J. Hallock, R. Kodis, and T. Sullivan, "Vortex Sensing Tests at NAFEC", Technical Report DOT-TSC-FAA-72-2, AD 749908, January 1972.

Chorin, A.J., "Computational Aspects of the Turbulence Problem", Proceedings of the Second International Conference on Numerical Methods in Fluid Dynamics, Sept. 15-19, 1970, Berkeley, California, Lecture Notes in Physics, edited by M. Holt, 8, Springer-Verlag.

Chorin, A.J., "Numerical Study of Slightly Viscous Flow", Journal of Fluid Mechanics, Vol. 57, part 4, pp. 785-796, 1973.

Donaldson, C. duP., R.S. Snedeker and R.D. Sullivan, "Calculation of the Wakes of Three Transport Aircraft in Holding, Takeoff, and Landing Configurations, and Comparison with Experimental Measurements", AFOSR-TR-73-1594 (also FAA-RD-73-42), 1973.

Hinze, J.O., Turbulence, McGraw-Hill, New York (1959).

Owen, P.R., "The Decay of a Turbulent Trailing Vortex", Aeronautical Quarterly, Vol. 21, pp. 69-78, 1970.

Spreiter, J.R. and A.H. Sacks, "The Rolling Up of the Trailing Vortex Sheet and Its Effect on the Downwash behind Wings", Journal of the Aeronautical Sciences, Vol. 18, 1951.

Thomson, J.A.L. and J.C.S. Meng, "Studies of Free Buoyant and Shear Flows by the VIC Method", presented at the Fourth International Conference on Numerical Methods in Fluid Dynamics, Denver, Colorado, June 24-29, 1974.

Thomson, J. Alex, "Study of Conceptual and Operational Feasibility of Laser Doppler Detection Systems", Progress Report to Nov. 30, 1970, for Contract No. NAS8-24810, Research Institute for Engineering Sciences, Wayne State University, Detroit, Michigan.

Westwater, F.L., Aero. Res. Coun., Rep. and Mem. No. 1692, 1936.

APPENDIX I: Centrifugal Effects on the Aerosol Density in a Two-Dimensional Vortex

Consider a simple two dimensional vortex formed in an atmosphere uniformly laden with aerosols at time $t = 0$. We wish to calculate the aerosol density as a function of time for the case of zero axial flow. Aerosol particles will centrifuge outward radially at a velocity equal to the Stokes velocity based on the local centripetal acceleration

$$V_r = \frac{2}{9}\left(\frac{\rho_p - \rho_a}{\rho_a}\right)\frac{a_p^2}{\nu}\;\frac{V_t^2}{r} \qquad \text{(A-I.1)}$$

where ν is the kinematic viscosity and a_p the aerosol particle radius. V_t is the tangential velocity at the radius r.

The aerosol number density obeys the continuity equation

$$\frac{\partial n}{\partial t} + \frac{1}{r}\,\frac{\partial}{\partial r}\left(nr\,V_r\right) = 0 \qquad \text{(A-I.2)}$$

We prescribe a vortex profile of the form

$$V_t = (\Gamma/2\pi r)\; f\,([r/R]^2) \qquad \text{(A-I.3)}$$

If we define a characteristic time T according to

$$T = \frac{9}{4}\left(\frac{\rho_a}{\rho_p - \rho_a}\right)\frac{\nu}{a_p^2}\left(\frac{2\pi R^2}{\Gamma}\right)^2 \qquad \text{(A-I.4)}$$

the continuity equation may be reduced to the form

$$\frac{\partial\psi}{\partial\tau} + \frac{\partial}{\partial u}\left(\frac{f^2}{u}\right) + \frac{f^2}{u}\,\frac{\partial\psi}{\partial u} = 0 \qquad \text{(A-I.5)}$$

where

$$\psi = \ln\,(n/n_o) \ ,$$

and

$$u = (r/R)^2 \text{ and } \tau = t/T \ . \qquad \text{(A-I.6)}$$

This equation is easily solved by the method of characteristics. We define a set of trajectories $r(\tau,\, r_o)$ by the relation

$$\frac{du}{d\tau} = \frac{f^2(u)}{u} \quad \text{or} \quad \frac{dr}{d\tau} = \frac{R^3 f^2[(r/R)^2]}{2r^3} \qquad \text{(A-I.7)}$$

for various initial values of $r = r_o$.
Along each of these trajectories we have

$$\frac{d\psi}{d\tau} = \frac{\partial\psi}{\partial u}\frac{du}{d\tau} + \frac{\partial\psi}{\partial\tau} = \frac{\partial\psi}{\partial u}\,\frac{f^2(u)}{u} + \frac{\partial\psi}{\partial\tau} \qquad \text{(A-I.8)}$$

or, from Equation (A-I.5),

$$\frac{d\psi}{d\tau} = -\frac{\partial}{\partial u}\left(\frac{f^2}{u}\right) \qquad \text{(A-I.9)}$$

This equation may be integrated along the trajectory defined by Eq. (A-I.7) giving the result that $nf^2(u)/u$ = constant along the characteristics.

The vortex profile that results for a uniform value of the effective viscosity (molecular or turbulent) is given by

$$f(u) = 1 - e^{-u}$$

or

$$V_t = \frac{\Gamma}{2\pi r}\left(1 - \exp\left(-r^2/R^2\right)\right) \quad . \qquad \text{(A-I.10)}$$

For this profile, the characteristics $(r = r(r_o,\tau))$ are defined by

$$\frac{t}{T} = \int_{(r_o/R)^2}^{(r/R)^2} \frac{u\,du}{\left(1 - e^{-u}\right)^2} \quad . \qquad \text{(A-I.11)}$$

Along each of these trajectories we have the relation

$$n(R/r)^2\left[1 - \exp\left[-(r/R)^2\right]\right]^2 = \text{constant along } r = r(r_o,\tau) . \qquad \text{(A-I.12)}$$

In Figure A-I.1 we show aerosol density profiles at various dimensionless times.

The characteristic times (T) for 2 micron radius water droplets are tabulated in Table I for a vortices characteristic of large jet aircraft. Three models are shown: one corresponding to the Spreiter-Sachs model of the vortex structure and the others to hypothesized high velocity core vortices. Reference to this table shows that 2μ radius particles may be centrifuged out of small high speed vortex cores (when peak tangential velocities exceed 100 feet/second) in a fraction

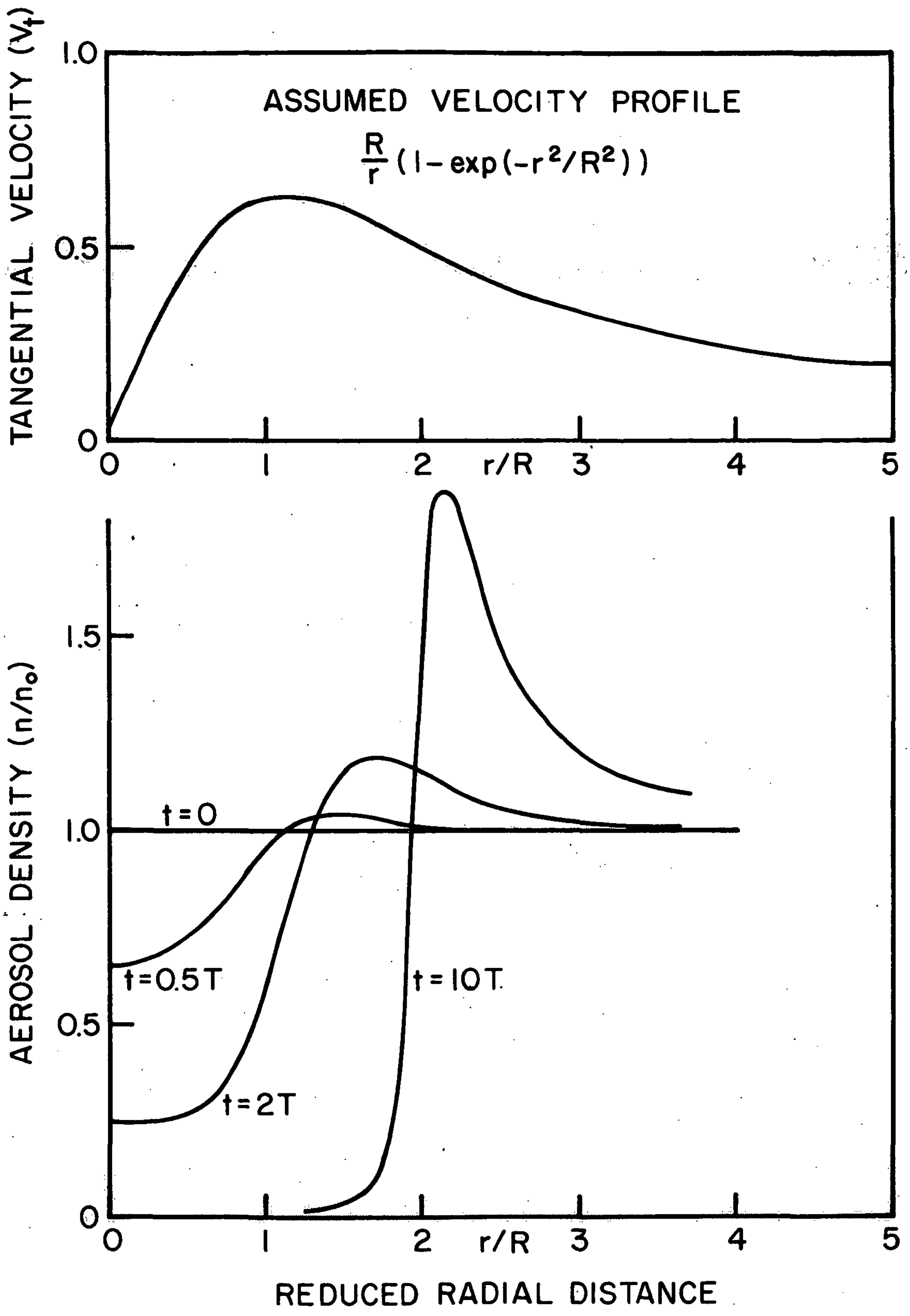

FIG. A-I.1. AEROSOL DENSITY AT VARIOUS TIMES

TABLE A-I.I

Centrifuging Times for 2µ Radius Water Droplets [Scales Inversely as (Particle Radius)^2]

		AIRCRAFT				
		B-737	B-727	B-707	B-747	DC-3
	Vortex Circulation (m^2/sec)	218 m^2/sec	297.	414.	628.	73.9
Spreiter-Sachs Model	Peak Tangential Velocity (.203 Γ/2R) (meters/second)	10.2 m/sec	11.9	12.2	13.8	3.45
	Core Diameter (2R) (meters)	4.35 m	5.05	6.90	9.29	4.35
	Centrifuging Time (seconds) (T)	187 sec	185	329	466	1635
"1/2" Spreiter-Sachs Model	Peak Tangential Velocity (.203 Γ/2R) (meters/second)	20.4	23.8	24.4	27.6	6.9
	Core Diameter (2R) (meters)	2.20	2.52	3.45	4.62	2.2
	Centrifuging Time (seconds) (T)	11.7	11.6	20.6	29.1	102
Owen's Model (at t=40 sec with Λ=1)	Peak Tangential Velocity (.203 Γ/2R) (meters/second)	30.3	36.1	42.2	51.8	17.8
	Core Diameter (2R) (meters)	1.46	1.67	1.99	2.46	.843
	Centrifuging Time (seconds) (T)	2.30	2.30	2.30	2.30	2.30

of a minute. However, for lower velocity cores, the time required for substantial aerosol density increases [a few times T (in Eq. A-I.4)] is several minutes.

APPENDIX II

Wake Parameters for Various Aircraft (Take off conditions - maximum load)
(based on the cylindrical vortex model)

Aircraft	737	727	707	747	C-47 (DC-3)
Weight (lbs)	104,000	161,000	336,000	710,000	29,300
Wing Span (ft) (S)	93	108	146	196	95
Velocity (ft/sec)	260	255	284	294	~ 150
Vortex Circulation (for L=W: ft^2/sec) $\Gamma = 4W/\pi S v \rho_a$	2,360	3,220	4,480	6,800	800
Vortex Separation (ft) $\left(b = \frac{\pi}{4} \text{ (span)}\right) = \frac{\pi}{4} S$	73.1	84.8	115	154	72
Initial Core Diameter (ft) (= 0.197 b)	14.3	16.6	22.7	30.4	14.4
Characteristic wake decay time (sec) $\left(\tau = 2\pi\rho V b^3/W = 2\pi b^2/\Gamma\right)$	14.1	13.7	18.2	21.6	42
Centerline downwash velocity (ft/sec) (= $2\Gamma/\pi b$)	20.6	24.2	24.8	28.2	7.3
Peak vortex tangential velocity (ft/sec) (= $\Gamma/2\pi a$)	52.5	61.1	63.2	72.0	18

APPENDIX III: Flow Chart of the LDV Simulation Program

The simulation program is composed mainly of three parts: the main program INVFD, which integrates the basic equations of motion with respect to time; the subroutine STREAM, which solves for the velocity field at each time; and the subroutine DISPLAY, which generates the LDV system response plots, the subroutine TPVRTX, which generates the linear displacements due to the tip vortices for all vortex elements distributed on the mesh. This is also the central theme of the hybrid VIC method which makes it possible to simulate the LDV system within reasonable limit of computer time. In general, the execution sequence flows from the INVFD to STREAM, KLMGRV, SEEDING, FOUR2, INTERP, VECTOR, TRAIL, DISPLAY, CALCP, TRAIL, 3DPROFL, and back to the main program INVFD. This process is repeated until the time t is greater than the interested elapse.

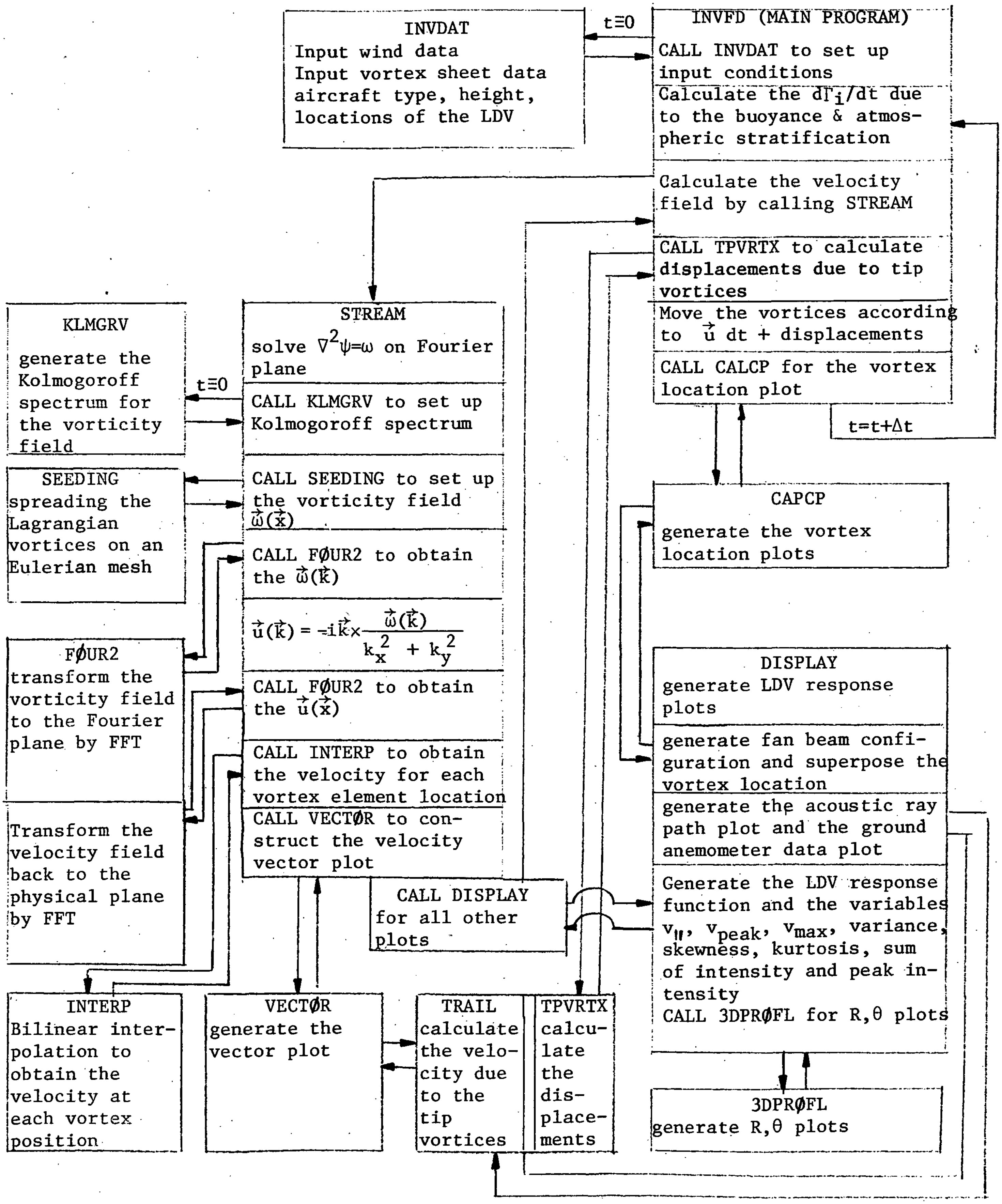
INVDAT
Input wind data
Input vortex sheet data
aircraft type, height,
locations of the LDV
t≡0
INVFD (MAIN PROGRAM)
CALL INVDAT to set up input conditions
Calculate the $d\Gamma_i/dt$ due to the buoyance & atmospheric stratification
Calculate the velocity field by calling STREAM
CALL TPVRTX to calculate displacements due to tip vortices
Move the vortices according to $\vec{u}$ dt + displacements
CALL CALCP for the vortex location plot
t=t+Δt
KLMGRV
generate the Kolmogoroff spectrum for the vorticity field
t≡0
STREAM
solve $\nabla^2\psi=\omega$ on Fourier plane
CALL KLMGRV to set up Kolmogoroff spectrum
CALL SEEDING to set up the vorticity field $\vec{\omega}(\vec{x})$
CALL FOUR2 to obtain the $\vec{\omega}(\vec{k})$
$\vec{u}(\vec{k}) = -i\vec{k}\times\frac{\vec{\omega}(\vec{k})}{k_x^2 + k_y^2}$
CALL FOUR2 to obtain the $\vec{u}(\vec{x})$
CALL INTERP to obtain the velocity for each vortex element location
CALL VECTOR to construct the velocity vector plot
SEEDING
spreading the Lagrangian vortices on an Eulerian mesh
FOUR2
transform the vorticity field to the Fourier plane by FFT
Transform the velocity field back to the physical plane by FFT
CAPCP
generate the vortex location plots
DISPLAY
generate LDV response plots
generate fan beam configuration and superpose the vortex location
generate the acoustic ray path plot and the ground anemometer data plot
Generate the LDV response function and the variables $v_{\parallel}$, v_{peak}, v_{max}, variance, skewness, kurtosis, sum of intensity and peak intensity
CALL 3DPROFL for R,θ plots
CALL DISPLAY for all other plots
INTERP
Bilinear interpolation to obtain the velocity at each vortex position
VECTOR
generate the vector plot
TRAIL
calculate the velocity due to the tip vortices
TPVRTX
calculate the displacements
3DPROFL
generate R,θ plots